UNIVERSITY OF PISA

The School of Graduate Studies in Basic Sciences "Galileo Galilei"

GRADUATE COURSE IN PHYSICS

PH.D. THESIS

Measurement of CP–Violating Asymmetries in the $D^0 \to \pi^+\pi^-$ and $D^0 \to K^+K^-$ Decays at CDF

Candidate:
Angelo Di Canto

Advisor:
Prof. Giovanni Punzi

XXIV Entrance, 2009–2011

A Viviana, Mamma,
Vito e Roberta

Abstract of the Thesis

Measurement of CP–Violating Asymmetries in the $D^0 \to \pi^+\pi^-$ and $D^0 \to K^+K^-$ Decays at CDF

by

Angelo Di Canto

Graduate Course in Physics

The School of Graduate Studies in Basic Sciences "Galileo Galilei"

University of Pisa

April 12, 2012

We report a search for non–Standard Model physics through the measurement of CP–violating asymmetries in the singly–Cabibbo–suppressed $D^0 \to \pi^+\pi^-$ and $D^0 \to K^+K^-$ decays reconstructed in about $5.9\,\text{fb}^{-1}$ of CDF data. We use the strong $D^{*+} \to D^0\pi^+$ decay ("D^* tag") to identify the flavor of the charmed meson at production time and exploit CP–conserving strong $c\bar{c}$ pair–production in $p\bar{p}$ collisions. Large samples of Cabibbo–favored $D^0 \to K^-\pi^+$ decays with and without D^* tag are used to highly suppress systematic uncertainties due to detector effects. The results are the world's most precise measurements to date and have been published by *Physical Review D* in January 2012 [1].

Contents

Introduction

One of the outstanding problems in particle physics is that the Standard Model implementation of CP violation, through the presence of the Cabibbo–Kobayashi–Maskawa phase, produces effects that are far from sufficient to explain the matter–antimatter asymmetry of the Universe. While investigations of the K and B systems have and will continue to play a central role in our quest to understand flavor physics and CP violation, in–depth examinations of the D mesons sector have yet to be performed with enough precision, leaving a gap in our knowledge. Since charm is the only heavy charged $+2/3$ quark presently accessible to experiments, which hadronizes into flavored mesons, it provides the sole window of opportunity to search for possible new CP–violating couplings, that might not exist in the down–quarks sector.

Singly–Cabibbo–suppressed transitions, such as $D^0 \to \pi^+\pi^-$ and $D^0 \to K^+K^-$, have long be indicated as ideal channels for looking for new effects of this type. Contribution to these decays from "penguin" amplitudes are negligible in the Standard Model, so the presence of New Physics could enhance the size of CP violation with respect to the Standard Model expectation, which predicts asymmetries of a few times 0.1%. However, conceivable New Physics effects are not too much larger than that, and the level of precision of existing measurements is still marginal for such explorations, that requires large samples and accurate calibration of possible sources of spurious asymmetries. At the CDF experiment at the TeVatron, large samples of charm hadrons are available thanks to the large production cross section in hadronic collisions and the presence of a specialized trigger on long–lived (weakly–decaying) states. Among these, $D^0 \to \pi^+\pi^-$ and $D^0 \to K^+K^-$ decays, consisting of only two charged tracks, have the additional advantage of being reconstructed with higher efficiency with respect to multibody decays or to other charm decays with neutral pions or K^0_S in their final states, thus allowing high precision searches for CP violation.

In the present work we measure the CP–violating asymmetry in decays of D^0 and $\overline{D}^0$ mesons into $\pi^+\pi^-$ and K^+K^- final states. Since the final states are charge–symmetric, to know whether they originate from a D^0 or a $\overline{D}^0$ decay, we need

the neutral charm candidate to be produced in the decay of an identified D^{*+} or D^{*-} meson. Flavor conservation in the strong interaction decay of the D^* meson allows identification of charm flavor through the sign of the charge of the π meson: $D^{*+} \to D^0\pi^+$ and $D^{*-} \to \overline{D}^0\pi^-$. We refer to neutral D mesons coming from an identified D^* decay as the *tagged* sample.

In the data collected by CDF between February 2002 and January 2010, corresponding to an integrated luminosity of about $5.9\,\text{fb}^{-1}$, we reconstruct approximately 215 thousand D^*–tagged $D^0 \to \pi^+\pi^-$ decays and 476 thousand D^*–tagged $D^0 \to K^+K^-$ decays.

To measure the CP asymmetry, we determine the number of detected decays of opposite flavor and use the fact that primary charm and anticharm mesons are produced in equal number by CP conserving strong interaction. We achieve a high precision cancellation of instrumental asymmetries and measure the CP asymmetries of $D^0 \to \pi^+\pi^-$ and $D^0 \to K^+K^-$ with a systematic uncertainty of about 10^{-3}, which is better than what has ever been previously achieved.

The thesis is organized as follows. In Chap. 1 we outline the phenomenology of CP violation in charm decays and the motivations for this measurement. In Chap. 2 we then briefly describe the experimental apparatus focusing the attention on the components of the CDF detector relevant for this analysis. We describe the strategy of the analysis and how we correct for detector–induced asymmetries in Chap. 3. The event selection and the kinematical requirements applied to isolate the different event samples are presented in Chap. 4, while the determination of observed asymmetries from data is described in Chap. 5. In Chap. 6 we discuss possible sources of systematic uncertainties and finally, in Chap. 7, we present the results and compare with measurements performed by other experiments showing that by combining them, it is possible to disentangle the contribution of direct and indirect CP violation.

Chapter 1

CP Violation in Charm Decays

This chapter introduces the motivations for the measurement described in this thesis. After a brief description of the theoretical framework, in which we discuss the connections between CP violation in the Standard Model and the charmed meson decays, we focus the attention on the $D^0 \to \pi^+\pi^-$ and $D^0 \to K^+K^-$ decays explaining how the search for CP violation in these decays can probe physics beyond the Standard Model. An overview of the measurement, as well as a summary of current experimental results are also presented.

1.1 Historical introduction

Symmetries play an important role in physics since they limit the possible terms which enter the Lagrangian and may be associated with conservation laws. Here we will be concerned with the role of CP violation, which is the violation of the combined conservation laws associated with charge conjugation (C) and parity (P) by the weak nuclear force. Charge conjugation is a mathematical operation that transforms a particle into an antiparticle, inverting the sign of all charges (such as electric charge) while leaving unaffected all other quantities (and in particular space–time related ones such as position, momentum and spin). It implies that every charged particle has an oppositely charged antimatter counterpart, while the antiparticle of an electrically neutral particle may be identical to the particle, as in the case of the neutral π meson, or it may be distinct, as with the antineutron. Parity, or space inversion, is the reflection in the origin of the space coordinates of a particle or particle system, *i. e.* the three space dimensions x, y, and z become, respectively, $-x$, $-y$, and $-z$. Stated more concretely, parity conservation means that left and right are indistinguishable by a physics process.

Before 1950s it was assumed that C and P were exact symmetries of elementary

processes, namely those involving electromagnetic, strong, and weak interactions. The same was held true for a third operation, time reversal (T), which trasforms the time coordinate t into $-t$. Invariance under time reversal implies that whenever a motion is allowed by the laws of physics, the reversed motion is also an allowed one. A series of discoveries from the mid–1950s caused physicists to alter significantly their assumptions about the invariance of C, P, and T. An apparent lack of the conservation of parity in the decay of charged K mesons into two or three π mesons prompted the theoretical physicists C. N. Yang and T.-D. Lee to examine the experimental foundation of parity itself. In 1956 they showed that there was no evidence supporting parity invariance in weak interactions [2]. Experiments conducted the next year verified decisively that parity was violated in both nuclear and pion's beta decays [3, 4]. Moreover, they revealed that charge conjugation symmetry was also broken during these decay processes. The discovery that the weak interaction conserves neither C nor P separately, however, led to a quantitative theory establishing combined CP as a symmetry of nature. This point was supported by the local T invariance derived from Mach's principle and from the CPT invariance that is natural in Lorentz–invariant quantum field theories [5, 6]: no CP violation is then allowed if T violation is not found. But further experiments, carried out in 1964, demonstrated that the electrically neutral K meson, which was thought to break down into three π mesons, decayed a fraction of the time into only two such particles, thereby violating CP symmetry.

The K^0 and $\overline{K}^0$ mesons are tipically produced in strong interactions, *e. g.* in processes like $\pi^- p \to K^0 \Lambda$ and $\pi^+ p \to \overline{K}^0 K^+ p$, and primarly decay weakly into two or three pions with very different lifetimes [7]:

$$\tau(K^0_{\mathrm{S}} \to 2\pi) \approx 0.9 \cdot 10^{-10} \text{ s};$$
$$\tau(K^0_{\mathrm{L}} \to 3\pi) \approx 0.5 \cdot 10^{-7} \text{ s}.$$

From these experimental observations one can expect that neutral K mesons are characterized by an additive quantum number S conserved in strong and electromagnetic interactions but violated by the weak interaction. Since S is not an absolutely conserved quantity, K^0 with $S = 1$ mixes with $\overline{K}^0$ with $S = -1$, and only an appropriate linear superposition of them is an eigenstates of the Hamiltonian. Since the final states with 3π and 2π are both CP eigenstates, with eigenvalue -1 e $+1$ respectively, it is natural to identify the $K^0_{\mathrm{S,L}}$ states as the CP eigenstates defined

by[1]

$$|K^0_{1,2}\rangle = \frac{|K^0\rangle \pm |\overline{K}^0\rangle}{\sqrt{2}}, \qquad \mathrm{CP} = \pm 1$$

This hypothesis has been widthdrawn in 1964, when the $K^0_{\mathrm{L}} \to \pi^+\pi^-$ decay was surprisly observed with a branching ratio at the 10^{-3} level [8]. This demonstrated that K_{L} state is governed by the CP–odd eigenstate, but also contains a small fraction of the CP–even eigenstate, which may decay through CP–conserving interactions into the $\pi^+\pi^-$ final state. This CP–violating effect is usually described by the observable [7]

$$\varepsilon_K = (2.228 \pm 0.011) \times 10^{-3} \times e^{i\pi/4}$$

defined through the following relations:

$$|K^0_{\mathrm{S}}\rangle = \frac{|K^0_1\rangle - \varepsilon_K |K^0_2\rangle}{\sqrt{1+|\varepsilon_K|^2}}, \qquad |K^0_{\mathrm{L}}\rangle = \frac{|K^0_2\rangle + \varepsilon_K |K^0_1\rangle}{\sqrt{1+|\varepsilon_K|^2}}.$$

At that time C and P violations were incorporated in the basic structure of the unified electroweak theory by assigning the left–handed and the right–handed fermions to doublet and singlet representations of the symmetry group $SU(2)_{\mathrm{L}} \times U(1)_{\mathrm{Y}}$. However, a striking feature of this theory, originally proposed by S. Glashow, S. Weinberg and A. Salam [9, 10, 11] as a theory of leptons and then extended by Glashow, J. Iliopoulos and L. Maiani [12] to quarks by postulating the existence of a fourth quark, the charm, was that it had CP and T invariance and so provided no explanation of the observed neutral K mesons phenomenology. This was an open problem until 1973, when M. Kobayashi and T. Maskawa [13] noticed that CP violation could be allowed in the electroweak model, by the presence of a single unremovable complex phase in the charged current interactions of quarks if there were at least six quarks. The existence of the charm and bottom quarks were established few years later, respectively in 1974 [14, 15] and in 1977 [16], while the sixth quark, the top, was discovered only in 1995 [17, 18]. The validity of the Kobayashi–Maskawa ansatz has been experimentally confirmed only recently when the $K^0 \to \pi^0\pi^0$ decay revealed the presence of direct CP violation in the neutral kaons system [19, 20] and when much more evident effects have been observed in the time evolution of the $B^0 - \overline{B}^0$ system [21, 22] or in two–body charmless B^0 decays [23, 24]. For their original contribution to the understanding of CP violation in

[1] It is a convention to choose $\mathrm{CP}|K^0\rangle = |\overline{K}^0\rangle$.

electroweak interactions, Kobayashi and Maskawa received in 2008 the Nobel prize in Physics.

The phenomenology of CP violation is particularly interesting since it could reveal the presence of "New Physics", *i. e.* physics beyond the Standard Model, as it actually did when it was firstly discovered. Interestingly, CP violation offers also a link to cosmology. One of the key features of our Universe is the cosmological baryon asymmetry of $\mathcal{O}(10^{-10})$[2]. As was pointed out by A. D. Sakharov [25], the necessary conditions for the generation of such an asymmetry include also the requirement that elementary interactions violate CP (and C). Model calculations of the baryon asymmetry indicate, however, that the CP violation present in the Standard Model seems to be too small to generate the observed asymmetry [26, 27, 28]. Almost any extension of the Standard Model provides new sources of CP violation, thus instilling the strong prejudice that there must be New Physics that is playing a role in hadrons decays. On the other hand, the required new sources of CP violation could be associated with very high energy scales and be still waiting to be discovered.

It is therefore essential to understand first the picture of CP violation arising in the framework of the Standard Model, where the Kobayashi–Maskawa mechanism plays a key role.

1.2 CP violation in the Standard Model

A model of elementary particles and their interactions is defined by the symmetries of the Lagrangian and the representations of fermions and scalars with respect to the trasformations of the symmetry group. The Standard Model is based on the gauge group[3]

$$G_{\mathrm{SM}} = SU(3)_{\mathrm{C}} \times SU(2)_{\mathrm{L}} \times U(1)_{\mathrm{Y}}. \tag{1.1}$$

where the $SU(3)_{\mathrm{C}}$ is the algebra of the strong forces and the electroweak part is described by $SU(2)_{\mathrm{L}} \times U(1)_{\mathrm{Y}}$ through the Glashow–Weinberg–Salam theory [9, 10, 11]. It contains three fermion generations, each consisting of five representations of

[2]This asymmetry is defined as the difference between the number density of baryons and that of antibaryons, normalized to the entropy of the Universe.

[3]In the following we do not discuss all the basic principles of the Standard Model but we concentrate only on those relevant for the understanding of CP violation. A more comprehensive and detailed description can be found in many textbooks, as for example Ref. [29].

$G_{\rm SM}$:

$$Q^I_{Li}(3,2)_{+1/6},\quad u^I_{Ri}(3,1)_{+2/3},\quad d^I_{Ri}(3,1)_{-1/3},\quad L^I_{Li}(1,2)_{-1/2},\quad \ell^I_{Ri}(1,1)_{-1}. \tag{1.2}$$

and a single scalar representation, the Higgs boson,

$$\phi(1,2)_{+1/2}. \tag{1.3}$$

Our notation means that, for example, left–handed quarks, Q^I_L, are triplets of $SU(3)_{\rm C}$, doublets of $SU(2)_{\rm L}$ and carry hypercharge $Y = +1/6$. The super–index I denotes interaction eigenstates. The sub–index $i = 1, 2, 3$ is the flavor (or generation) index.

The scalar $\phi = (\phi^+, \phi^0)^T$ assumes a vacuum expectation value,

$$\langle\phi\rangle = \begin{pmatrix} 0 \\ \frac{v}{\sqrt{2}} \end{pmatrix}, \tag{1.4}$$

so that the gauge group is spontaneously broken,

$$G_{\rm SM} \to SU(3)_{\rm C} \times U(1)_{\rm EM}. \tag{1.5}$$

The Standard Model Lagrangian, $\mathcal{L}_{\rm SM}$, is the most general renormalizable Lagrangian that is consistent with the gauge symmetry of Eq. (1.1), the particle content of Eqs. (1.2) and (1.3) and the pattern of spontaneous symmetry breaking given by Eq. (1.4). It can be divided into four parts:

$$\mathcal{L}_{\rm SM} = \mathcal{L}_{\rm gauge} + \mathcal{L}_{\rm kinetic} + \mathcal{L}_{\rm Higgs} + \mathcal{L}_{\rm Yukawa}. \tag{1.6}$$

The first part contains the fermions kinetic terms, of the form $i\psi\gamma_\mu D^\mu\psi$ where, to maintain gauge invariance, one defines the covariant derivative D^μ as:

$$D^\mu = \partial^\mu + ig_s G^\mu_a L_a + igW^\mu_b \Sigma_b + ig' B^\mu Y. \tag{1.7}$$

Here G^μ_a are the eight gluon fields, W^μ_b the three weak interaction bosons and B^μ the single hypercharge boson. The L_a's are $SU(3)_{\rm C}$ generators (the 3×3 Gell-Mann matrices $\lambda_a/2$ for triplets, 0 for singlets), the Σ_b's are $SU(2)_{\rm L}$ generators (the 2×2 Pauli matrices $\sigma_b/2$ for doublets, 0 for singlets), and the Y's are the $U(1)_{\rm Y}$ charges. As an example, for the left–handed quarks Q^I_L, we have

$$\mathcal{L}_{\rm kinetic}(Q^I_L) = i\overline{Q}^I_{Li}\gamma_\mu \left(\partial^\mu + \frac{i}{2}g_s G^\mu_a \lambda_a + \frac{i}{2}gW^\mu_b \tau_b + \frac{i}{6}g' B^\mu\right) Q^I_{Li}, \tag{1.8}$$

This part of the interaction Lagrangian is always CP conserving.

The second part of Eq. (1.6) describes the self–interactions of the gauge fields and is written as

$$-\mathcal{L}_{\text{gauge}} = \frac{1}{4}\left(G_a^{\mu\nu} G_{a\ \mu\nu} + W_b^{\mu\nu} W_{b\ \mu\nu} + B^{\mu\nu} B_{\mu\nu}\right),$$

where we introduced the Yang and Mills tensors $G_a^{\mu\nu} = \partial^\mu G_a^\nu - \partial^\nu G_a^\mu + g_s f_{abc} G_b^\mu G_c^\nu$, $W_b^{\mu\nu} = \partial^\mu W_b^\nu - \partial^\nu W_b^\mu$ and $B^{\mu\nu} = \partial^\mu B^\nu - \partial^\nu B^\mu$. This part would also seem to be CP invariant but actually there exists an additional gauge–invariant and renormalizable operator, namely

$$G_a^{\mu\nu} \tilde{G}_{a\ \mu\nu} = \frac{1}{2}\,\varepsilon_{\mu\nu\sigma\varrho} G_a^{\mu\nu} G_a^{\sigma\varrho},$$

which could be introduced in the QCD Lagrangian and which violates P, T and CP. Moreover, even if its coefficient in $\mathcal{L}_{\text{SM}}$ is set to zero at the tree–level, non–perturbative corrections will resurrect it, thus inducing a complex phase, θ_{QCD}, which is flavor diagonal. However, the bounds on the electric dipole moment of the neutron imply that $\theta_{\text{QCD}} \lesssim 10^{-9}$ [30]. The Standard Model offers no natural explanation to the smallness of θ_{QCD}. This puzzle is called "the strong CP problem". This is generally assumed to be solved by some type of New Physics, such as a Peccei–Quinn symmetry [31, 32], which sets θ_{QCD} to zero, *i. e.* in the following we assume $\mathcal{L}_{\text{gauge}}$ to conserve the CP symmetry.

The Higgs potential, which describes the scalar self interactions, is given by:

$$\mathcal{L}_{\text{Higgs}} = \mu^2 \phi^\dagger \phi - \lambda (\phi^\dagger \phi)^2.$$

For the Standard Model scalar sector, where there is a single doublet, this part of the Lagrangian is also CP conserving. For extended scalar sectors, such as that of a two Higgs doublet model, $\mathcal{L}_{\text{Higgs}}$ can be CP violating. Even in case that it is CP symmetric, it may lead to spontaneous CP violation.

The Yukawa interactions are given by

$$-\mathcal{L}_{\text{Yukawa}} = Y_{ij}^d \overline{Q}_{Li}^I \phi d_{Rj}^I + Y_{ij}^u \overline{Q}_{Li}^I \tilde{\phi} u_{Rj}^I + Y_{ij}^\ell \overline{L}_{Li}^I \tilde{\phi} \ell_{Rj}^I + \text{h.c.}, \tag{1.9}$$

where $\tilde{\phi} = i\sigma_2 \phi^\dagger$. This part of the Lagrangian is, in general, CP violating as we are going to explain now.

After the electroweak symmetry is broken by a non–zero vacuum expectation value v of the Higgs field (see Eq. (1.4)), the Yukawa terms in Eq. (1.9) yield (upon

the replacement $\Re\mathrm{e}(\phi^0) \to (v + H^0)/\sqrt{2}$) the mass matrices of quarks and charged leptons:

$$-\mathcal{L}_M = (M_d)_{ij}\bar{d}^I_{Li}d^I_{Rj} + (M_u)_{ij}\bar{u}^I_{Li}u^I_{Rj} + (M_\ell)_{ij}\bar{\ell}^I_{Li}\ell^I_{Rj} + \text{h.c.},$$

where $M_f = \frac{v}{\sqrt{2}}Y^f$, and we decomposed the $SU(2)_\mathrm{L}$ doublets into their components:

$$Q^I_{Li} = \begin{pmatrix} u^I_{Li} \\ d^I_{Li} \end{pmatrix} \quad L^I_{Li} = \begin{pmatrix} \nu^I_{Li} \\ e^I_{Li} \end{pmatrix}.$$

Since the Standard Model neutrinos have no Yukawa interactions, they are predicted to be massless.[4]

The mass basis corresponds, by definition, to diagonal mass matrices. We can always find unitary matrices V_{fL} and V_{fR} such that

$$V_{fL}M_fV^\dagger_{fR} = M^{\mathrm{diag}}_f,$$

with M^{diag}_f diagonal and real. The mass eigenstates are then identified as

$$\begin{aligned} d_{Li} &= (V_{dL})_{ij}d^I_{Lj}, \quad d_{Ri} = (V_{dR})_{ij}d^I_{Rj}, \\ u_{Li} &= (V_{uL})_{ij}u^I_{Lj}, \quad u_{Ri} = (V_{uR})_{ij}u^I_{Rj}, \\ \ell_{Li} &= (V_{\ell L})_{ij}\ell^I_{Lj}, \quad \ell_{Ri} = (V_{\ell R})_{ij}\ell^I_{Rj}, \quad \nu_{Li} = (V_{\nu L})_{ij}\nu^I_{Lj}. \end{aligned}$$

Since the Standard Model neutrinos are massless, $V_{\nu L}$ is arbitrary.

The charged current interactions (that is the interactions of the charged $SU(2)_\mathrm{L}$ gauge bosons $W^\pm_\mu = (W^1_\mu \mp iW^2_\mu)/\sqrt{2}$) for quarks, which in the interaction basis are described by Eq. (1.8), have a complicated form in the mass basis:

$$-\mathcal{L}_W = \frac{g}{\sqrt{2}}\bar{u}_{Li}\gamma^\mu(V_{uL}V^\dagger_{dL})_{ij}d_{Lj}W^+_\mu + \text{h.c.}.$$

where the unitary 3×3 matrix,

$$V_{\mathrm{CKM}} = V_{uL}V^\dagger_{dL} = \begin{pmatrix} V_{ud} & V_{us} & V_{ub} \\ V_{cd} & V_{cs} & V_{cb} \\ V_{td} & V_{ts} & V_{tb} \end{pmatrix},$$

[4] This is mere a consequence of the fact that in the Standard Model there are no $SU(2)_\mathrm{L}$–singlet ("sterile") right–handed neutrinos, $\nu^I_{Ri}(1,1)_0$, thus it is impossible to produce Dirac mass terms of the form $\bar{\nu}^I_{Li}\nu^I_{Rj}$. Moreover, for the Standard Model neutrinos, ν^I_{Li}, there are also no renormalizable Majorana mass terms. Therefore, the established observations of neutrino masses [7] necessarily call for an extension of the Standard Model through either an extention of its Higgs content, or its fermion content, or both, or enlarging the gauge group (which also requires extended particle content) [33].

is the Cabibbo–Kobayashi–Maskawa (CKM) quark mixing matrix [34, 13].

If $V_{\rm CKM}$ is real (and thus orthogonal), $\mathcal{L}_W = \mathrm{CP}\mathcal{L}_W(\mathrm{CP})^\dagger$ and CP symmetry is conserved in the weak interactions. Yet the occurrance of complex matrix elements does not automatically signal CP violation. This can be seen through the following algebraic argument. A unitary $n \times n$ matrix contains n^2 independent real parameters, $2n-1$ of those can be eliminated through the rephasing of the n up–type and n down–type fermion fields (changing all fermions by the same phase obviously does not affect $V_{\rm CKM}$); hence there are $(n-1)^2$ physical parameters left. A unitary matrix is also orthogonal, and as such it contains $n(n-1)/2$ parameters corresponding to the independent rotation angles between the n basis vectors; thus the remaining $(n-1)(n-2)/2$ parameters must be complex phases. For $n = 2$, *i. e.* two families there is just one mixing angle, the Cabibbo angle [34]. For $n = 3$ there are instead four physical parameters, namely three Euler angles and one phase. It is the latter that provides a gateway for CP violation.

As a result of the fact that $V_{\rm CKM}$ is not diagonal, the $W^\pm$ gauge bosons couple to quark (mass eigenstates) of different generations. Within the Standard Model, this is the only source of *flavor changing* interactions. In principle, there could be additional sources of flavor mixing (and of CP violation) in the lepton sector and in Z^0 interactions, but within the Standard Model with three families and massless neutrinos this does not happen.

1.2.1 Further requirements for CP violation in the Kobayashi–Maskawa model

The current knowledge of the CKM matrix elements moduli, as obtained from Ref. [35], is the following

$$|V_{\rm CKM}| = \begin{pmatrix} 0.97426^{+0.00022}_{-0.00014} & 0.22539^{+0.00062}_{-0.00095} & 0.003501^{+0.000196}_{-0.000087} \\ 0.22526^{+0.00062}_{-0.00095} & 0.97345^{+0.00022}_{-0.00018} & 0.04070^{+0.00116}_{-0.00059} \\ 0.00846^{+0.00043}_{-0.00015} & 0.03996^{+0.00114}_{-0.00062} & 0.999165^{+0.000024}_{-0.000048} \end{pmatrix}. \tag{1.10}$$

Using just the observed hierarchy $|V_{ub}| \ll |V_{cb}| \ll |V_{us}|, |V_{cd}| \ll 1$ one can, as firstly realized by Wolfenstein [36], expand $V_{\rm CKM}$ in powers of $\lambda = |V_{us}|$ (the sine of the

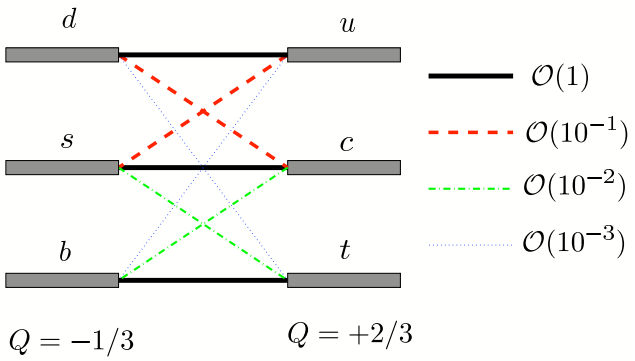

Figure 1.1: *Schematic representation of the CKM hierarchy between the different charged current transitions of quarks.*

Cabibbo angle). The expansion up to and including terms $\mathcal{O}(\lambda^5)$ is given by [37]:

$$V_{\rm CKM} = \begin{pmatrix} 1-\lambda^2/2-\lambda^4/8 & \lambda & A\lambda^3(\varrho-i\eta) \\ -\lambda+A^2\lambda^5[1-2(\varrho+i\eta)]/2 & 1-\lambda^2/2-\lambda^4(1+4A^2)/8 & A\lambda^2 \\ A\lambda^3[1-(1-\lambda^2/2)(\varrho+i\eta)] & -A\lambda^2+A\lambda^4[1-2(\varrho+i\eta)]/2 & 1-A^2\lambda^4/2 \end{pmatrix} + \mathcal{O}(\lambda^6), \tag{1.11}$$

where A, ϱ and η are the remaining real parameters, all of order unity ($\lambda \approx 0.23$, $A \approx 0.80$, $\varrho \approx 0.14$, $\eta \approx 0.34$ [35]).[5] In such representation, we clearly see that the CKM matrix is a very special unitary matrix: it is almost diagonal, it is almost symmetric and the matrix elements get smaller the more one moves away from the diagonal (see Fig. 1.1). Another observation is that $\eta/\varrho \sim \mathcal{O}(1)$ shows that CP is not even an approximate symmetry of the Standard Model: the smallness of CP violating effects is just due to the small mixing angles which appear together with the complex CKM phase in the expressions for specific observables, rather than a necessity. Conversely, it should be observed that the CP violating parameter η can be determined just from experiments on CP conserving processes, since $V_{\rm CKM}$ is uniquely determined by the moduli of its elements.

It is important to note that the position in which the complex terms appear in the CKM matrix is not physically significant, as in different parameterizations the complex phase shifts to different matrix elements. One can define, however, a CP violating quantity in $V_{\rm CKM}$ that is independent of the parameterization [39]. This

[5] It is worth to notice that in this parameterization $|V_{ub}/V_{cb}| \sim \lambda$, while the current data, shown in Eq. (1.10), indicates instead that $|V_{ub}/V_{cb}| \sim \lambda^2$. Thus, for current experimental sensitivities, different parameterizations of the CKM matrix are better suited [38].

quantity is the Jarlskog invariant, $J_{\rm CP}$, defined through the relation

$$\Im\mathrm{m}[V_{ij}V_{kl}V_{il}^*V_{kj}^*] = J_{\rm CP}\sum_{m,n\in\{d,s,b\}}\varepsilon_{ikm}\varepsilon_{jln} \qquad (i,j,k,l\in\{d,s,b\}). \tag{1.12}$$

CP is violated in the Standard Model only if $J_{\rm CP}\neq 0$, and in fact current measurements tell us [35]:

$$J_{\rm CP} = (2.884^{+0.253}_{-0.053})\cdot 10^{-5}.$$

It is interesting to note that any CP violating quantity in the Standard Model must be proportional to $J_{\rm CP}$, reflecting the fact that a single complex phase appears in the 3×3 CKM matrix. This feature makes the Standard Model implementation of CP violation (in principle) very predictive, all possible asymmetry measurements are correlated by their common origin from a single parameter of the theory.

Eq. (1.12) can also be expressed in terms of the Yukawa coupling, so the necessary and sufficient condition to have CP symmetry in the Standard Model is the vanishing of the quantity [39]

$$\Im\mathrm{m}\,\det[Y^dY^{d\dagger},Y^uY^{u\dagger}] = 2(m_t^2-m_c^2)(m_t^2-m_u^2)(m_c^2-m_u^2)\\ (m_b^2-m_s^2)(m_b^2-m_d^2)(m_s^2-m_d^2)J_{\rm CP}$$

Here the mass terms reflect the fact that the CKM phase could be eliminated through an appropriate unitary transformation of the quark fields if any two up–type or down–type quarks were degenerate in mass. Consequently, the origin of CP violation is closely related to the "flavor problem" in elementary particle physics, and it cannot be understood in a deeper way, unless we have fundamental insights into the hierarchy of quark masses and the number of fermion generations.

Eq. (1.12) also shows that at least four different quarks (real or virtual) must be involved in a process to exhibit CP violation. Large effects are then to be expected in transitions for which any competiting CP conserving amplitude is small, *e. g.* K decays, Cabibbo–suppressed D decays ($c\to u$) or, even better, B decays involving the small V_{ub} element; virtual processes involving V_{tb}, such as rare flavor changing neutral current K decays, are also very natural candidates.

1.2.1.1 Unitarity triangles

The qualitative difference between a two and a three family scenario can be also seen in a less abstract way. The unitarity of the CKM matrix, $V_{\rm CKM}V_{\rm CKM}^\dagger = 1$,

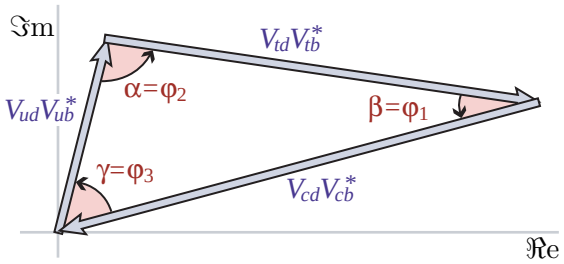

Figure 1.2: *Graphical representation of the unitary triangle of Eq.* (1.17) *in the complex plane.*

leads to a set of 9 equations,

$$\sum_{k\in\{u,c,t\}} V_{ki}V_{kj}^* = \delta_{ij} \qquad (i,j \in \{d,s,b\}),$$

6 of which require the sum of three complex quantities to vanish:

$$\underbrace{V_{ud}V_{us}^*}_{\mathcal{O}(\lambda)} + \underbrace{V_{cd}V_{cs}^*}_{\mathcal{O}(\lambda)} + \underbrace{V_{td}V_{ts}^*}_{\mathcal{O}(\lambda^5)} = 0; \tag{1.13}$$

$$\underbrace{V_{ud}^*V_{cd}}_{\mathcal{O}(\lambda)} + \underbrace{V_{us}^*V_{cs}}_{\mathcal{O}(\lambda)} + \underbrace{V_{ub}^*V_{cb}}_{\mathcal{O}(\lambda^5)} = 0; \tag{1.14}$$

$$\underbrace{V_{us}V_{ub}^*}_{\mathcal{O}(\lambda^4)} + \underbrace{V_{cs}V_{cb}^*}_{\mathcal{O}(\lambda^2)} + \underbrace{V_{ts}V_{tb}^*}_{\mathcal{O}(\lambda^2)} = 0; \tag{1.15}$$

$$\underbrace{V_{cd}^*V_{td}}_{\mathcal{O}(\lambda^4)} + \underbrace{V_{cs}^*V_{ts}}_{\mathcal{O}(\lambda^2)} + \underbrace{V_{cb}^*V_{tb}}_{\mathcal{O}(\lambda^2)} = 0; \tag{1.16}$$

$$\underbrace{V_{ud}V_{ub}^*}_{\mathcal{O}(\lambda^3)} + \underbrace{V_{cd}V_{cb}^*}_{\mathcal{O}(\lambda^3)} + \underbrace{V_{td}V_{tb}^*}_{\mathcal{O}(\lambda^3)} = 0; \tag{1.17}$$

$$\underbrace{V_{ud}^*V_{td}}_{\mathcal{O}(\lambda^3)} + \underbrace{V_{us}^*V_{ts}}_{\mathcal{O}(\lambda^3)} + \underbrace{V_{ub}^*V_{tb}}_{\mathcal{O}(\lambda^3)} = 0. \tag{1.18}$$

Each of these relations can be geometrically represented in the complex plane as triangles, as graphically shown in Fig. 1.2 for Eq. (1.17). These are "the unitarity triangles", though the term "unitarity triangle" is usually reserved for Eq. (1.17) only.

The shapes of the six triangles are very different from each other, as indicated in Eqs. (1.13)–(1.18) by expressing each side in terms of the powers of λ, but it can be easily shown that all have the same area, equal to $|J_{\rm CP}|/2$, *i. e.* the fact that the triangles do not degenerate into a line represents CP violation. It become obvious now that there cannot be CP violation in the Standard Model with only two generations of quarks.

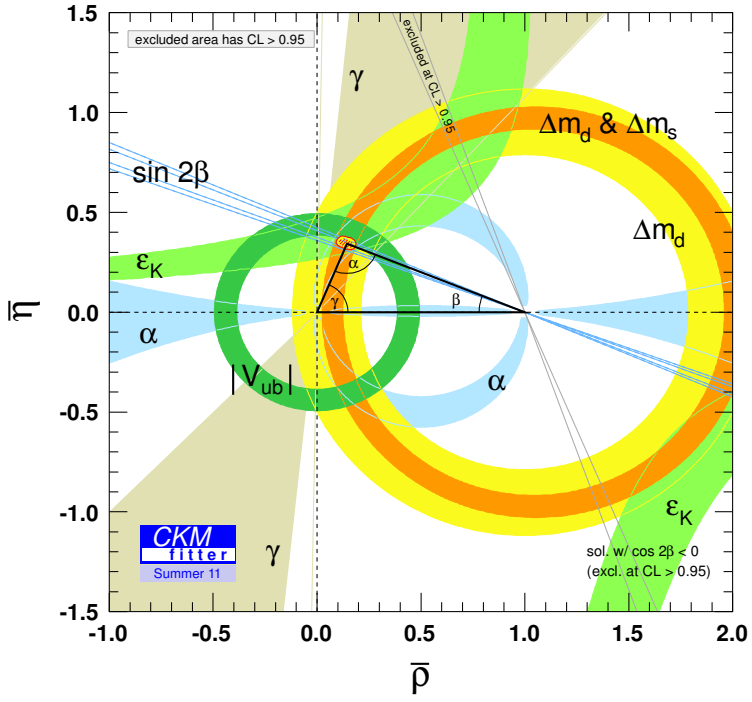

Figure 1.3: *Constraints in the* $(\bar{\varrho}, \bar{\eta})$ *plane. The red hashed region of the global combination corresponds to 68% CL.*

Fig. 1.3 shows all the experimental constraints to the unitary triangle of Eq. (1.17), as well as the results of the global fit with the 68% CL contour for the position of the apex[6] (red hashed area) as obtained by the CKMfitter Group [35].

1.3 Phenomenology of CP violation in meson decays

In the previous section, we understood how CP violation arises in the Standard Model. Now we are going to describe the implications of this theory for the phenomenology of CP violation in meson decays. Our main focus will be on neutral D meson decaying to CP eigenstates with two charged pions or kaons, but, since the phenomenology of CP violation is superficially different in K, D, B, and B_s decays we first introduce some notations and formalism that applies to all pseudoscalar mesons. However, as a matter of practical convenience, we will refer specifically to

[6]The apex of the unitarity triangle is obtained when Eq. (1.17) is normalized by $V_{cd}V_{cb}^*$.

D meson mixing and decays, even if most of our discussion applies equally well to K, B and B_s mesons. Our treatment will follow very closely the one presented in Ref. [40].

We define decay amplitudes of a D meson (which could be charged or neutral) and its CP conjugate $\overline{D}$ to a multi–particle final state f and its CP conjugate $\overline{f}$ as

$$A_f = \langle f|\mathcal{H}|D\rangle, \quad \overline{A}_f = \langle f|\mathcal{H}|\overline{D}\rangle, \quad A_{\bar{f}} = \langle \overline{f}|\mathcal{H}|D\rangle, \quad \overline{A}_{\bar{f}} = \langle \overline{f}|\mathcal{H}|\overline{D}\rangle$$

where $\mathcal{H}$ is the decay Hamiltonian.

There are two types of phases that may appear in A_f and $\bar{A}_{\bar{f}}$. Complex parameters in any Lagrangian term that contributes to the amplitude will appear in complex conjugate form in the CP–conjugate amplitude. Thus their phases appear in A_f and $\bar{A}_{\bar{f}}$ with opposite signs. In the Standard Model these phases occur only in the CKM matrix which is part of the electroweak sector of the theory, hence these are often called "weak phases". The weak phase of any single term is convention dependent. However the difference between the weak phases in two different terms in A_f is convention independent because the phase rotations of the initial and final states are the same for every term. A second type of phase can appear in scattering or decay amplitudes even when the Lagrangian is real. Such phases do not violate CP and they appear in A_f and $\bar{A}_{\bar{f}}$ with the same sign. Their origin is the possible contribution from intermediate on–shell states in the decay process, that is an absorptive part of an amplitude that has contributions from coupled channels. Usually the dominant rescattering is due to strong interactions and hence the designation "strong phases" for the phase shifts so induced. Again only the relative strong phases of different terms in a scattering amplitude have physical content, an overall phase rotation of the entire amplitude has no physical consequences.

CP violation in the decay appears as a result of interference among various terms in the decay amplitude, and will not occur unless at least two terms have different weak phases and different strong phases. As an example, let us consider a decay process which can proceed through several amplitudes:

$$A_f = \sum_j |A_j|\ e^{i(\delta_j+\phi_j)}, \qquad \overline{A}_{\bar{f}} = \sum_j |A_j|\ e^{i(\delta_j-\phi_j)},$$

where δ_j and ϕ_j are strong (CP conserving) and weak (CP violating) phases, respectively. To observe CP violation one needs $|A_f| \neq |\overline{A}_{\bar{f}}|$, *i. e.* there must be a

contribution from at least two processes with different weak and strong phases in order to have a non vanishing interferience term

$$|A_f|^2 - |\overline{A}_{\bar{f}}|^2 = -2\sum_{i,j} |A_i||A_j| \sin(\delta_i - \delta_j)\sin(\phi_i - \phi_j).$$

The phenomenology of CP violation in neutral flavored meson decays is enriched by the possibility that, besides the decay, it is also possible to have $D^0 \leftrightarrow \overline{D}^0$ transitions, also known as flavor mixing or oscillations. Particle–antiparticle mixing has been observed in all four flavored neutral meson systems, *i. e.* in neutral kaon, both neutral B meson systems and neutral D meson system. The particle–antiparticle mixing phenomenon causes an initial (at time $t = 0$), pure D^0 meson state to evolve in time to a linear combination of D^0 and $\overline{D}^0$ states. If the times t in which we are interested are much larger than the typical strong interaction scale, then the time evolution can be described by the approximate Schrödinger equation:

$$i\frac{d}{dt}\begin{pmatrix} D^0(t) \\ \overline{D}^0(t) \end{pmatrix} = \left[\boldsymbol{M} - \frac{i}{2}\boldsymbol{\Gamma}\right]\begin{pmatrix} D^0(t) \\ \overline{D}^0(t) \end{pmatrix},$$

where $\mathbf{M}$ and $\boldsymbol{\Gamma}$ are 2×2 Hermitian matrices,

$$\boldsymbol{M} = \begin{pmatrix} M_{11} & M_{12} \\ M_{12}^* & M_{22} \end{pmatrix} \quad \text{and} \quad \boldsymbol{\Gamma} = \begin{pmatrix} \Gamma_{11} & \Gamma_{12} \\ \Gamma_{12}^* & \Gamma_{22} \end{pmatrix},$$

associated with transitions via off–shell (dispersive) and on–shell (absorptive) intermediate states, respectively. Diagonal elements of $\mathcal{H}_{\text{eff}} = \boldsymbol{M} - i\boldsymbol{\Gamma}/2$ are associated with the flavor–conserving transitions $D^0 \to D^0$ and $\overline{D}^0 \to \overline{D}^0$ while off–diagonal elements are associated with flavor–changing transitions $D^0 \leftrightarrow \overline{D}^0$. The matrix elements of $\boldsymbol{M}$ and $\boldsymbol{\Gamma}$ must satisfy $M_{11} = M_{22}$ and $\Gamma_{11} = \Gamma_{22}$ in order to be consistent with CPT invariance.

The eigenstates of the effective Hamiltonian $\mathcal{H}_{\text{eff}}$ are

$$|D_{L,H}\rangle = p\ |D^0\rangle \pm q\ |\overline{D}^0\rangle$$

while the corresponding eigenvalues are

$$\lambda_{L,H} = \left(M_{11} - \frac{i}{2}\Gamma_{11}\right) \pm \frac{q}{p}\left(M_{12} - \frac{i}{2}\Gamma_{12}\right) \equiv m_{L,H} - \frac{i}{2}\Gamma_{L,H}.$$

The coefficients p and q are complex coefficients, satisfying $|p|^2 + |q|^2 = 1$, and

$$\frac{q}{p} = \sqrt{\frac{M_{12}^* - \frac{i}{2}\Gamma_{12}^*}{M_{12} - \frac{i}{2}\Gamma_{12}}} = \left|\frac{q}{p}\right| e^{i\phi}.$$

The real parts of the eigenvalues $\lambda_{1,2}$ represent masses, $m_{L,H}$, and their imaginary parts represent the widths $\Gamma_{L,H}$ of the two eigenstates $|D_{L,H}\rangle$, respectively. The sub–scripts H (heavy) and L (light) are here used because by convention we choose $\Delta m = m_H - m_L > 0$, while the sign of $\Delta\Gamma = \Gamma_L - \Gamma_H$ is not known *a priori* and needs to be experimentally determined.[7]

The time–dependent decay amplitude of an initially pure D^0 state decaying to final state f is then given by

$$\langle f|\mathcal{H}|D^0(t)\rangle = A_f\ g_+(t) + \bar{A}_f\ \frac{q}{p}\ g_-(t),$$

where

$$|g_\pm(t)|^2 = \frac{1}{2}\ e^{-t/\tau}\left[\cos\left(\frac{xt}{\tau}\right) \pm \cosh\left(\frac{xt}{\tau}\right)\right]$$

represents the time–dependent probability to conserve the initial flavor (+) or oscillate into the opposite flavor (−) and x, y are dimensionless mixing parameters defined as

$$x = \frac{\Delta m}{\Gamma}, \qquad y = \frac{\Delta\Gamma}{2\Gamma},$$

and $\Gamma = (\Gamma_L + \Gamma_H)/2 = 1/\tau$ is the mean decay width.

The time–dependent decay rate, proportional to $|\langle f|\mathcal{H}|D^0(t)\rangle|^2$, is then

$$\frac{d\Gamma}{dt}(D^0(t) \to f) \propto |A_f|^2\Bigg[(1 - |\lambda_f|^2)\cos\left(\frac{xt}{\tau}\right) + (1 + |\lambda_f|^2)\cosh\left(\frac{yt}{\tau}\right) - 2\Im\mathrm{m}(\lambda_f)\sin\left(\frac{xt}{\tau}\right) + 2\Re\mathrm{e}(\lambda_f)\sinh\left(\frac{xt}{\tau}\right)\Bigg].$$

with

$$\lambda_f = \frac{q}{p}\ \frac{\overline{A}_f}{A_f}.$$

In analogy with this treatment one can show that for an initial pure $\overline{D}^0$ eigenstate the decay rate is

$$\frac{d\Gamma}{dt}(\overline{D}^0(t) \to f) \propto |\bar{A}_f|^2\Bigg[(1 - |\lambda_f^{-1}|^2)\cos\left(\frac{xt}{\tau}\right) + (1 + |\lambda_f^{-1}|^2)\cosh\left(\frac{yt}{\tau}\right) - 2\Im\mathrm{m}(\lambda_f^{-1})\sin\left(\frac{xt}{\tau}\right) + 2\Re\mathrm{e}(\lambda_f^{-1})\sinh\left(\frac{yt}{\tau}\right)\Bigg].$$

[7] Another possible choice, which is in standard usage for K^0 mesons, defines the mass eigenstates according to their lifetimes: K_S for the short–lived and K_L for the long–lived state, with $\Delta\Gamma_K = \Gamma_\mathrm{S} - \Gamma_\mathrm{L}$ positive by definition. The K_L is then experimentally found to be the heavier state, *i. e.* also $\Delta m_K > 0$.

Decay rates to the CP–conjugate final state $\bar{f}$ are obtained analogously, with the substitutions $A_f \to A_{\bar{f}}$ and $\overline{A}_f \to \overline{A}_{\bar{f}}$ in the above equations. Terms proportional to $|A_f|^2$ or $|\overline{A}_f|^2$ are associated with decays that occur without any net $D^0 \leftrightarrow \overline{D}^0$ oscillation, while terms proportional to $|\lambda_f|^2$ or $|\lambda_f^{-1}|^2$ are associated with decays following a net oscillation; the $\sin(xt/\tau)$ and $\sinh(yt/\tau)$ terms are instead associated with the interference between these two cases.

While CP violation in charged meson decays depends only on A_f and $\overline{A}_{\bar{f}}$, in the case of neutral mesons, because of the possibility of flavor oscillations, CP violating effects have additional dependences on the values of $|q/p|$ and λ_f. We then distinguish three types of CP violating effects in meson decays:

(i) CP violation in the decay is defined by

$$|\overline{A}_{\bar{f}}/A_f| \neq 1.$$

In charged meson decays, where mixing effects are absent, this is the only possible source of CP asymmetries:

$$\mathcal{A}_{\rm CP}(D \to f) \equiv \frac{\Gamma(D \to f) - \Gamma(\overline{D} \to \bar{f})}{\Gamma(D \to f) + \Gamma(\overline{D} \to \bar{f})} = \frac{1 - |\overline{A}_{\bar{f}}/A_f|^2}{1 + |\overline{A}_{\bar{f}}/A_f|^2} \tag{1.19}$$

(ii) CP violation in mixing is defined by

$$|q/p| \neq 1.$$

In this case, in place of Eq. (1.19), it is usefull to define the time–dependent asymmetry

$$\mathcal{A}_{\rm CP}(D^0 \to f; t) = \frac{d\Gamma(D^0(t) \to f)/dt - d\Gamma(\overline{D}^0(t) \to \bar{f})/dt}{d\Gamma(D^0(t) \to f)/dt + d\Gamma(\overline{D}^0(t) \to \bar{f})/dt}, \tag{1.20}$$

(iii) CP violation in interference between a decay without mixing, $D^0 \to f$, and a decay with mixing, $D^0 \to \overline{D}^0 \to f$ (such an effect occurs only in decays to final states that are common to both D^0 and $\overline{D}^0$, including all CP eigenstates), is defined by

$$\Im\mathrm{m}\lambda_f \neq 0$$

Usually type (i) is also know as direct CP violation, while type (ii) and (iii) are referred as indirect CP violation.

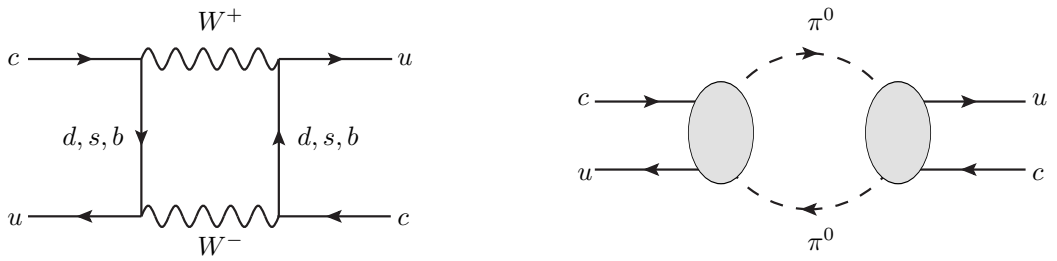

Figure 1.4: *Examples of Feynman diagrams which describe "short" (left) and "long distance" (right) contributions to the* $D^0 - \overline{D}^0$ *mixing amplitude. In the Standard Model the latter diagrams dominate over the "short distance" ones which are negligible compared to the first because of the small CKM coupling to the b quark and of GIM suppression of the remaing two light–quark loops.*

1.4 CP violation in neutral charmed mesons decays

The phenomenology of CP violation in neutral meson decays has been primarly studied in the K and B systems. While these investigations have and will continue to play a central rôle in our quest to understand flavor physics and CP violation, in–depth examinations of the D mesons sector have yet to be performed with enough precision, leaving a gap in our knowledge. In particular, the searches performed in the past 15 years in over 30 decay modes of D^0, D^+, and D_s^+ mesons by Belle, *BABAR*, Cleo, CDF, FOCUS, E796 and E687 experiments [41] are all consistent with CP conservation but have only recently started reaching interesting level of sensitivity below the 1% in some decay modes.

The interest in charm dynamics has increased recently with the evidence of charm oscillations reported by three different experiments [42, 43, 44], which, when combined together with all other available experimental information, established the existence of mixing at the 10σ level [41]. In the Standard Model mixing in neutral D meson system can proceed through a double weak boson exchange (short distance contributions) represented by box diagrams, or through intermediate states that are accessible to both D^0 and $\overline{D}^0$ (long distance effects), as represented in Fig. 1.4. Potentially large long distance contributions are non–perturbative and therefore difficult to estimate, so the predictions for the mixing parameters x and y within the Standard Model span several orders of magnitude between 10^{-8} and 10^{-2} [45]. The measured values of x and y, as averaged by the *Heavy Flavor Averaging Group*

(HFAG) when CP violation is allowed [41], are

$$x = (0.63^{+0.19}_{-0.20})\% \quad \text{and} \quad y = (0.75 \pm 0.12)\%. \tag{1.21}$$

The large uncertainties of the Standard Model mixing predictions make it difficult to identify New Physics contributions (a clear hint would be, if x is found to be much larger than y), however since current measurements are on the upper end of most theory predictions [45], they could be interpreted as a possible hint for New Physics.

Charm oscillations could be enhanced by a broad class of non–Standard Model physics processes [46]: *e. g.* models with extra fermions like a forth generation down–type quark, with flavor changing neutral currents at tree level mediated by additional gauge bosons or in general with new symmetry of the theory like in Supersymmetry (SUSY). Any generic New Physics contribution to the mixing would naturally carry additional CP–violating phases, which could enhance the observed CP–violating asymmetries relative to Standard Model predictions. Moreover, since charmed hadrons are the only hadrons, presently accessible to experiment, composed of a heavy charged $+2/3$ quark[8], they provides the sole window of opportunity to examine scenarios where up–type quarks play a special role, such as SUSY models where the down quark and the squark mass matrices are aligned [47, 48] and, more generally, models in which CKM mixing is generated in the up–quark sector.

Moreover, within the Standard Model, CP violation in charm decays is predicted to be negligibly small since the physics of these decays involves, to an excellent approximation, only the first two quark generations and is therefore CP conserving [49]. Charm decays can therefore be well probed for the existence and analyses of a New Physics "signal" without too much Standard Model "background".

1.4.1 Cabibbo–suppressed $D^0 \to \pi^+\pi^-$ and $D^0 \to K^+K^-$ decays

Examples of clean channels where to study both direct and indirect CP violation in the charm system are the neutral singly–Cabibbo–suppressed decays into CP–eigenstates, such as $D^0 \to \pi^+\pi^-$ and $D^0 \to K^+K^-$ (collectively referred to as $D^0 \to h^+h^-$ in the following).

[8] The top quark decays before it forms a hadron and therefore cannot oscillate; the absence of flavor mixing reduces significantly the possibility to study CP violating effects involving the other down–type quarks.

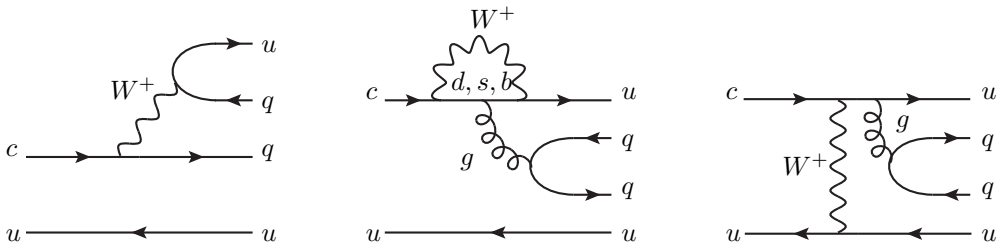

Figure 1.5: *Feynman diagrams of the possible topologies (from left to right: tree, one–loop penguin, W–exchange) of the $D^0 \to h^+h^-$ decays. The symbol q stands for either a d or a s quark.*

Owing to the slow mixing rate of charm mesons, the time–dependent asymmetry of Eq. (1.20) can be approximated to first order as the sum of two terms:

$$\mathcal{A}_{\rm CP}(D^0 \to f; t) = \mathcal{A}^{\rm dir}_{\rm CP}(D^0 \to f) + \frac{t}{\tau}\,\mathcal{A}^{\rm ind}_{\rm CP}(D^0 \to f) \quad (x, y \ll \tau/t) \tag{1.22}$$

where $\mathcal{A}^{\rm dir}_{\rm CP}$ and $\mathcal{A}^{\rm ind}_{\rm CP}$ represents direct and indirect CP asymmetries, respectively. In the case f is a CP eigenstate, as for $D^0 \to h^+h^-$ decays, then

$$\mathcal{A}^{\rm dir}_{\rm CP}(D^0 \to f) = \frac{1 - \left|\overline{A}_f/A_f\right|^2}{1 + \left|\overline{A}_f/A_f\right|^2} \quad \text{and} \tag{1.23}$$

$$\mathcal{A}^{\rm ind}_{\rm CP}(D^0 \to f) = \frac{1}{2}\left[y\ \Re{\rm e}(\lambda_f - \lambda_f^{-1}) - x\ \Im{\rm m}(\lambda_f - \lambda_f^{-1})\right] \tag{1.24}$$

Within the Standard Model direct CP violation can occur in singly–Cabibbo–suppressed charm decays ($c \to uq\bar{q}$ with $q = d, s$) because the final state particles contain at least one pair of quark and antiquark of the same flavor, which makes a contribution from penguin–type or box amplitudes induced by virtual b–quarks possible in addition to the tree amplitudes [49].[9] However, as shown in the Feynman diagrams of Fig. 1.5, the contribution of these second order amplitudes are strongly suppressed by the small combination of CKM matrix elements $V_{cb}V^*_{ub}$. Moreover, the tree amplitudes are practically CP conserving, since, for both $D^0 \to \pi^+\pi^-$ and $D^0 \to K^+K^-$ decays, they involve only one CKM factor, $V_{cd}V^*_{ud}$ and $V_{cs}V^*_{us}$ respectively, which is real in Wolfenstein parametrization up to $\mathcal{O}(\lambda^4)$ and $\mathcal{O}(\lambda^6)$. Hence to first order one would expect to observe an asymmetry consistent only with

[9] Conversely, in the Standard Model, it is not possible to have direct CP violarion in Cabbibo–favored ($c \to su\bar{d}$) or doubly–Cabbibo–suppressed ($c \to du\bar{s}$) charm decays.

the mixing phase ϕ, with no decay phase contribution:

$$\begin{aligned}\mathcal{A}_{\rm CP}(D^0 \to h^+h^-) &\approx \mathcal{A}_{\rm CP}^{\rm ind}(D^0 \to h^+h^-) \\ &\approx \frac{\eta_{\rm CP}}{2}\left[y\left(\left|\frac{q}{p}\right| - \left|\frac{p}{q}\right|\right)\cos\phi + x\left(\left|\frac{q}{p}\right| + \left|\frac{p}{q}\right|\right)\sin\phi\right],\end{aligned}$$

where $\eta_{\rm CP} = +1$ is the CP eigenvalue of the h^+h^- final state. The Standard Model dynamics predicts indirect CP asymmetries around $\mathcal{O}(10^{-3})$, being suppressed by the value of x and y (see Eq. (1.21)), while direct CP violation produces asymmetries one order of magnitude smaller. In addition, in the limit of U–spin symmetry, the direct component is equal in magnitude and opposite in sign for $D^0 \to K^+K^-$ and $D^0 \to \pi^+\pi^-$ [50].

As already mentioned in the previous section, New Physics contributions to the charm mixing would, in general, also exhibit larger CP violation. This mixing–induced effects, in many scenarios beyond the Standard Model, would in addition provide sources of direct CP violation in $D^0 \to h^+h^-$ decays both at tree level (extra quark in Standard Model vector–like representation, SUSY without R–parity models, two Higgs doublet models) or at one–loop (QCD penguin and dipole operators, flavor changing neutral currents in supersymmetric flavor models) as described in Ref. [50]. While the first group of models can produce an effect that is much less than 1%, the processes having one–loop can even reach the percent level, producing effects that are clearly not expected in the Standard Model.

In the absence of large new weak phases in the decay amplitudes, *i. e.* negligible direct CP violation from New Physics, the CP asymmetries in singly–Cabibbo–suppressed decays into final CP eigenstates would be dominated by mixing–induced effects and thus universal, *i. e.* independent of the final state. So if different asymmetries are observed between $D^0 \to \pi^+\pi^-$ and $D^0 \to K^+K^-$ decays, then direct CP violation must be present.

In summary, $D^0 \to h^+h^-$ decays are powerful probes of New Physics contributions in the mixing transition amplitudes. They also probe the magnitude of penguin contributions, which are negligible in the Standard Model, but could be greatly enhanced by the exchange of additional non–Standard Model particles. Both phenomena would, in general, increase the size of the observed CP violation with respect to the Standard Model expectation, which is both CKM and loop–suppressed and, therefore, entirely negligible at present level of experimental sensitivity. Any

significant CP violating asymmetry at the 1% level expected in the CKM hierarchy would then be a strong evidence of new dynamics [51, 52, 53].

1.4.1.1 Time–integrated measurement of CP asymmetries

The sources of a possible asymmetry in neutral D meson decays can be distinguished by their dependence on the decay–time, so a time–dependent analysis seems necessary. However, as outlined in the following, sensitivity to indirect CP violation can be achieved also with time–integrated measurements if the detector acceptance allows to collect samples of D^0 mesons with decay–times longer than τ.

The time–integrated asymmetry is the time integral of Eq. (1.22) over the observed distribution of proper decay time, $D(t)$:

$$\begin{aligned}\mathcal{A}_{\rm CP}(D^0 \to h^+h^-) &= \mathcal{A}^{\rm dir}_{\rm CP}(D^0 \to h^+h^-) + \mathcal{A}^{\rm ind}_{\rm CP}(D^0 \to h^+h^-) \int_0^\infty \frac{t}{\tau}\, D(t)dt \\ &= \mathcal{A}^{\rm dir}_{\rm CP}(D^0 \to h^+h^-) + \frac{\langle t\rangle}{\tau}\, \mathcal{A}^{\rm ind}_{\rm CP}(D^0 \to h^+h^-). \quad (1.25)\end{aligned}$$

Since the value of $\langle t\rangle$ depends on $D(t)$, different values of time–integrated asymmetry may be observed in different experimental environments because of different detector acceptances as a function of decay time, thus providing different sensitivities to $\mathcal{A}^{\rm dir}_{\rm CP}$ or $\mathcal{A}^{\rm ind}_{\rm CP}$. In experiments where the reconstruction efficiency does not depend on proper decay time ($D(t) = 1$), as it is the case at the B–factories, the factor $\langle t\rangle/\tau$ equals unity resulting in the same sensitivity to direct and indirect CP violation. On the contrary, as we will detail in Sect. 2.2.3, the data used in this analysis were collected with an online event selection (trigger) that imposes requirements on the displacement of the D^0 meson decay point from the production point, thus rejecting candidates with short decay times which results in $\langle t\rangle/\tau > 1$. This makes the present measurement more sensitive to mixing–induced CP violation. In addition, combination of our results with those from Belle and *BABAR* provides some discrimination between the two contributions to the asymmetry.

The current experimental status is summarized in Tab. 1.1. No CP violation has been found within the precision of about 0.5% attained by Belle [55] and *BABAR* [54]. The previous CDF result [56] dates from 2005 and was obtained using data from only $123\,\mathrm{pb}^{-1}$ of early Run II integrated luminosity. The results presented in this thesis are based on a data sample, corresponding to about $5.9\,\mathrm{fb}^{-1}$ of integrated

Experiment	$\mathcal{A}_{\rm CP}(\pi^+\pi^-)$ (%)	$\mathcal{A}_{\rm CP}(K^+K^-)$ (%)
BABAR 2008	-0.24 ± 0.52 (*stat.*) ± 0.22 (*syst.*)	$+0.00 \pm 0.34$ (*stat.*) ± 0.13 (*syst.*)
Belle 2008	$+0.43 \pm 0.52$ (*stat.*) ± 0.12 (*syst.*)	-0.43 ± 0.30 (*stat.*) ± 0.11 (*syst.*)
CDF 2005	$+1.0 \pm 1.3$ (*stat.*) ± 0.6 (*syst.*)	$+2.0 \pm 1.2$ (*stat.*) ± 0.6 (*syst.*)

Table 1.1: Summary of recent experimental measurements of CP violating asymmetries in two–body singly–Cabibbo–suppressed decays of D^0 mesons [54, 55, 56].

luminosity. This is currently the world's largest samples of exclusive charm meson decays in charged final states, with signal purities competitive to those achievable at the so–called heavy–flavor factories.

Chapter 2

Experimental Apparatus

This chapter briefly describes the TeVatron collider and the CDF II detector, focusing on the subsystems most important for heavy flavour physics such as the tracking and the trigger systems.

2.1 The Fermilab's TeVatron collider

The TeVatron is a circular synchrotron of 1 km in radius, located at the Fermi National Accelerator Laboratory (FNAL or Fermilab), about 50 km West from Chicago (IL), USA, that collides bunches of protons against bunches of antiprotons accelerated in opposite direction, both at energies of 980 GeV. The energy available in the center–of–mass after the collision is thus $\sqrt{s} = 1.96\,\text{TeV}$, the world's highest until the beginning of LHC operations.

Together with the center–of–mass energy another key quantity that characterizes the performance of a collider is the instantaneous luminosity, $\mathscr{L}$, that is the coefficient of proportionality between the rate of a given process and its cross–section σ:

$$\frac{dN}{dt}\ [\text{events/s}] = \mathscr{L}\left[\text{cm}^{-2}\text{s}^{-1}\right] \cdot \sigma\left[\text{cm}^{2}\right].$$

The time–integral of the luminosity (integrated luminosity) is therefore a measure of the expected number of events, N, produced in a finite time T:

$$N(T) = \int_0^T \mathscr{L}\ \sigma\ dt.$$

Assuming an ideal head–on $p\bar{p}$ collision with no crossing angle between the beams, the instantaneous luminosity at the TeVatron is defined as

$$\mathscr{L} = 10^{-5}\frac{N_p N_{\bar{p}} B f \beta\gamma}{2\pi\beta^\star\sqrt{(\varepsilon_p+\varepsilon_{\bar{p}})_x(\varepsilon_p+\varepsilon_{\bar{p}})_y}}\ F\left(\sigma_z/\beta^\star\right) \qquad \left[10^{30}\text{cm}^{-2}\text{s}^{-1}\right]$$

where N_p ($N_{\bar{p}}$) is the average number of protons (antiprotons) in each bunch ($N_p \approx 8.1 \cdot 10^{11}$ and $N_{\bar{p}} \approx 2.9 \cdot 10^{11}$), B (36) is the number of bunches per beam circulating into the ring, f (47.713 kHz) is the revolution frequency, $\beta\gamma$ is the relativistic factor of the Lorentz boost (1045.8 at 980 GeV), F is an empiric form factor which depends on the ratio between the longitudinal width of the bunch ($\sigma_z \approx 60$ cm) and the "betatron function" calculated at the interaction point ($\beta^\star \approx 31$ cm), and finally ε_p ($\varepsilon_{\bar{p}}$) is the 95% normalized emittance of the proton (antiproton) beam ($\varepsilon_p \approx 18\pi$ mm mrad and $\varepsilon_{\bar{p}} \approx 13\pi$ mm mrad after injection).[1]

The luminosity is determined only through quantities that depend on the acceleration performance: at the TeVatron the most limiting factor of the luminosity is the availability of antiprotons since it is difficult to produce, to compact into bunches and to transfer them efficiently through all the acceleration stages.

The TeVatron is the final sector of a more complex accelerators system, entirely represented in Fig. 2.1, which provides beam to different typologies of experiments ($p\bar{p}$ collisions, fixed–target, etc.). We will now describe the procedure for obtaining a continuous period of collider operation, called a *store*, using the same collection of protons and antiprotons. Further details can be found in Refs. [57, 58].

2.1.1 The proton beam

The protons production starts with turning hydrogen gas into H^- ions. The gas, in the molecular state H_2, is placed in a container lined with molybdenum electrodes: a matchbox–sized, oval–shaped cathode and a surrounding anode, separated by 1 mm and held in place by glass ceramic insulators. A magnetron generates a plasma that forms H^- ions near the metal surface. These are then extracted out of the container by a 750 keV electrostatic field, applied by a commercial Cockcroft–Walton generator, and injected into a 150 m long linear accelerator (*Linac*) which

[1] The form factor F is a parameterization of the longitudinal profile of the beams in the collision region, which assumes the characteristic shape of an "hourglass" posed horizontally and centered in the interaction point. The betatron function is a parameter convenient for solving the equation of motion of a particle through an arbitrary beam transport system; β is a local function of the magnetic properties of the ring and it is indipendent of the accelerating particle. The emittance ε measures the phase space occupied by the particles of the beam; three independent two–dimensional emittances are defined, for each of them $\sqrt{\beta\varepsilon}$ is proportional to the statistical width of the beam in the corresponding phase plane.

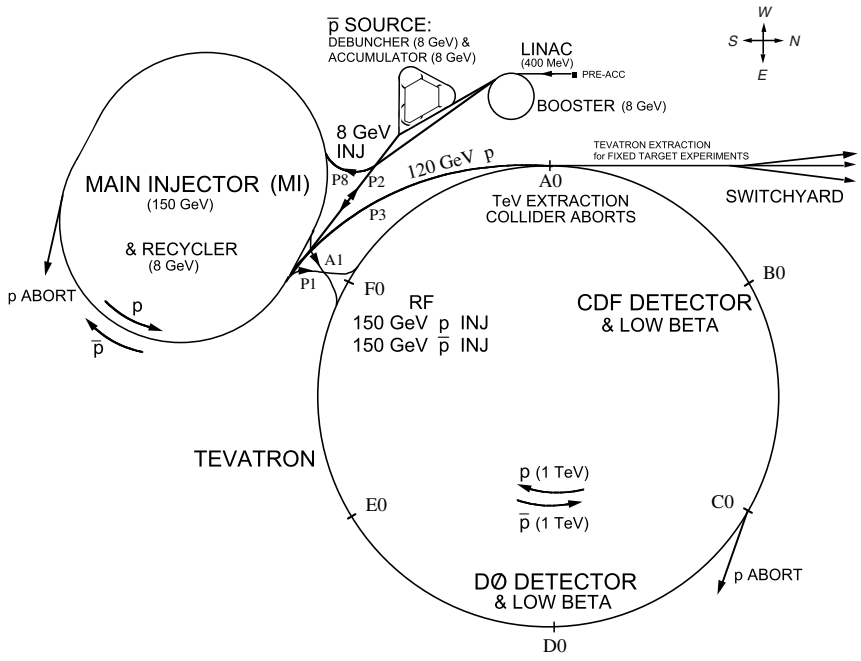

Figure 2.1: *Sketch of the Fermilab's accelerators system.*

increases their energy up to 400 MeV. A carbon foil is used to strip the electrons from the H^- before the resulting protons are injected into the *Booster*. The Booster is a rapid cycling synchrotron (radius of 75 m) which accelerates the protons up to 8 GeV and compacts them into bunches of about $5 \cdot 10^{12}$ particles each. The bunches are then transfered into the *Main Injector*, a synchrotron which brings their energy up to 150 GeV, and finally into the TeVatron where superconducting magnets keep them on an approximately circular orbit waiting for the antiproton beam to be injected.

2.1.2 The antiproton beam

While the energy of the protons bunches circulating in the Main Injector reaches 120 GeV, they are slammed to a rotating 7 cm thick nickel target. Spatially wide–spread antiprotons are produced and focused into a beam via an appropiate magnetic lens which separates them from other charged interaction products. The emerging antiprotons have a bunch structure similar to that of the incident protons and are stored in a *Debuncher*. This is a storage ring where the momentum spread of the antiprotons is reduced while maintaining a constant energy of 8 GeV,

via stochastic cooling stations. Many cycles of Debuncher cause the destruction of the bunch structure which results in a continuous beam of antiprotons. At the end of the process the monochromatic antiprotons are transferred into the *Accumulator* which is a triangle-shaped storage ring where they are further cooled and stored until the cycles of the Debuncher are completed. When a current sufficient to create 36 bunches with the required density is available, the antiprotons are injected into the Main Injector, here accelerated up to 150 GeV and finally transferred into the TeVatron where 36 bunches of protons are already circulating in opposite direction.

2.1.3 The collision

When 36 bunches of both protons and antiprotons are circulating in the TeVatron, the energy of the machine is increased in about 10 s from 150 to 980 GeV and the collisions begin at the two interaction points: DØ and BØ (where the DØ and the CDF II detectors are respectively located). Special quadrupole magnets (*low–β squeezers*) located at both extremities of the detectors along the beam pipe "squeeze" the beam in the longitudinal direction to maximize the luminosity inside the detectors. Then the beam transverse profile is shaped to its optimized configuration by mean of iron plates which act as collimators and sweep away the transverse beam halo. The interaction region thus achieves a roughly Gaussian distribution in both transverse ($\sigma_T \approx 30\,\mu$m) and longitudinal ($\sigma_z \approx 28$ cm) planes with its center in the nominal interaction point. When the beam profile is narrow enough and the conditions are safely stable the detectors are powered and the data taking starts.

In the last years of operations, as we will outline in the next section, when collisions start the peak luminosity is almost regularly above $3.2 \times 10^{32}\,\mathrm{cm}^{-2}\mathrm{s}^{-1}$. While collisions are taking place the luminosity decreases exponentially[2] because of the beam–gas and beam–halo interactions. In the meantime, antiproton production and storage continues. When the antiproton stack is sufficiently large ($\simeq 4 \times 10^{12}$ antiprotons) and the circulating beams are degraded the detector high–voltages are switched off and the store is dumped. The beam is extracted via a switch–yard and sent to an absorption zone. Beam abortion can occur also accidentally when the temperature of a superconducting magnet shift above the critical value and a magnet quenches destroying the orbit of the beams. The time between the end of a

[2]The decrease is about a factor of 3 (5) for a store of $\sim$ 10 (20) hrs.

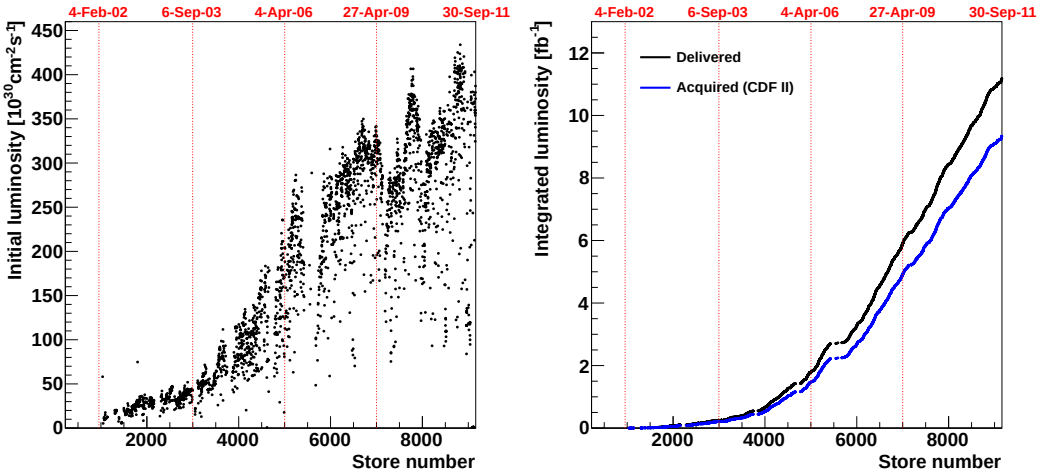

(a) (b)

Figure 2.2: *Initial (a) and integrated (b) luminosity as a function of store number/time.*

store and the beginning of collisions of the next one is typically $\sim 1\,\text{hr}$; during this time calibrations of the sub–detectors and test runs with cosmics are performed.

2.1.4 Run II performances and achievements

The TeVatron $p\bar{p}$ collider has been the centerpiece of the world's high energy physics program for almost a quarter of century, beginning operation in December of 1985 until it was overtaken by the LHC first in the colliding beam energy, in November 2009, and then in terms of colliding beam luminosity, in April 2011. In this section we briefly describe the achievements of such a long history, focusing in particular the attention on the latter period of TeVatron operations initiated in March 2001 and continued through September 2011, which is commonly referred to as *Run II*.

Fig. 2.2 (a) shows the collider performance history in terms of instantaneous luminosity. As already stated, at the end of the Run II, typical TeVatron luminosities were well constantly above $3.2 \times 10^{32}\,\text{cm}^{-2}\text{s}^{-1}$, with record peak above $4.4 \times 10^{32}\,\text{cm}^{-2}\text{s}^{-1}$, thus ultimately exceeding its initial luminosity goal by a factor of 400. The plot also shows the steadly increase occurred during the years after numerous improvements, some were implemented during operation and others were introduced during regular shutdown periods. They took place in all accelerators

and addressed all parameters affecting luminosity, proton and antiproton intensities, emittances, optics functions, bunch length, losses, reliability and availability, etc.

The TeVatron integrated luminosity has greatly progressed over the years, too (see Fig. 2.2 (b)) and, at the end of Run II operations, a total of $11\,\mathrm{fb}^{-1}$ of $p\bar{p}$ collisions has been delivered to both experiments, thus enabling CDF and DØ to carefully study the Standard Model and observe many of its important features for the first time.

2.2 The CDF II detector

CDF II, in operation between 2001 and 2011, is an azimutally and forward–backward symmetric apparatus designed to study $p\bar{p}$ collisions at the TeVatron. It is a multi–purpose cylindrical–shaped detector, about 15 m in length and 15 m in diameter, composed of several specialized subsystems, each one designed to perform a different task, as shown in Fig. 2.3. High resolution three–dimensional charged particle tracking is achieved through an integrated system consisting of three silicon inner subdetectors and a large outer drift chamber, all contained in a superconducting solenoid, 1.5 m in radius and 4.8 m in length, which generates a 1.4 T magnetic field parallel to the beam axis. Outside the magnet a non–compensated calorimeter system provides electrons and photons identification and finely segmented sampling of energy flow coming from final state particles as well as identification of neutrinos via transverse energy imbalance. A system of muon chambers plus scintillators, is instead used to track and identify muons which pass through the calorimeters interacting as minimum–ionizing–particles.

In the following sections we describe the general features of the most important subsystems for the study of heavy flavour production and decays, while a comprehensive description of the entire apparatus is given in Ref. [59]. In order to do so we first need to establish few conventions.

2.2.1 Coordinates and notation

CDF II employs a right–handed Cartesian coordinates system with the origin in the BØ interaction point, assumed coincident with the center of the drift chamber.

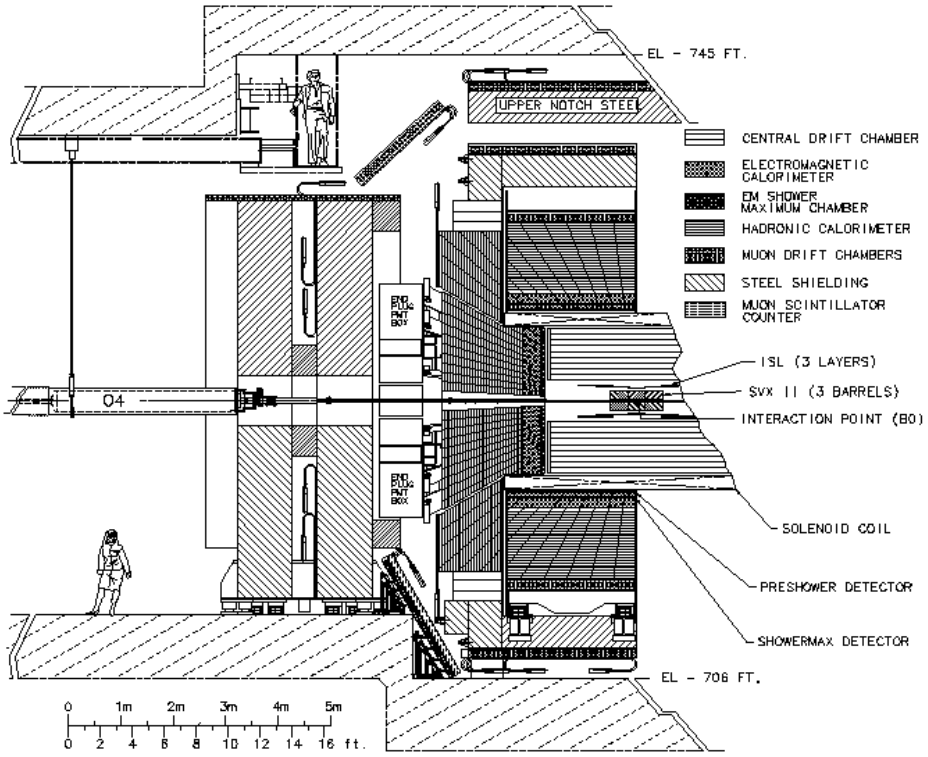

Figure 2.3: *Elevation view of one half of the CDF II detector.*

The positive z axis lies along the nominal beam–line pointing toward the proton direction. The (x, y) plane is therefore perpendicular to either beams, with positive y axis pointing vertically upward and positive x axis in the horizontal plane of the TeVatron, pointing radially outward with respect to the center of the ring.

Since the colliding beams of the TeVatron are unpolarized, the resulting physical observations are invariant under rotations around the beam line axis. Thus, a cylindrical (r, ϕ, z) coordinates system is particularly convenient to describe the detector geometry. Throughout this thesis, *longitudinal* (or *axial*) means parallel to the proton beam direction (*i. e.* to the z axis) and *transverse* means perpendicular to the proton direction (*i. e.* in the (x, y) or (r, ϕ) plane).

Since the protons and antiprotons are composite particles, the actual interaction occurs between their individuals partons (valence or sea quarks and gluons). Each parton carries a varying fraction of the (anti)proton momentum, not known on a event–by–event basis. As a consequence of the possible imbalance in the longitudinal components of the momenta of interacting partons, possible large velocities along

z for the center–of–mass of the parton–level interaction may occur. In the hadron collisions environment, it is customary to use a variable invariant under z boosts as an unit of relativistic phase–space, instead of the polar angle θ. This variable is the *rapidity*, defined as

$$Y = \frac{1}{2} \ln\left(\frac{E + p\cos\theta}{E - p\cos\theta}\right),$$

where $(E, \boldsymbol{p})$ is the energy–momentum four–vector of the particle. Under a $\hat{\boldsymbol{z}}$ boost to an inertial frame with velocity β, the rapidity of a particle transforms linearly, according to $Y \to Y' = Y + \tanh^{-1}\beta$, therefore Y is invariant since $dY \equiv dY'$. However, a measurement of rapidity still requires a detector with accurate identification capabilities because of the mass term entering E. Thus, for practical reasons, it is often preferred to substitute Y with its approximate expression η in the ultra–relativistic limit (usually valid for products of high–energy collisions):

$$Y \overset{p \gg m}{\longrightarrow} \eta + \mathcal{O}(m^2/p^2),$$

where the *pseudo–rapidity*,

$$\eta = -\ln\tan\left(\frac{\theta}{2}\right),$$

is only function of the momenta. As the event–by–event longitudinal position of the actual interaction is distributed around the nominal interaction point with 28 cm r.m.s width, it is useful to distinguish the *detector pseudo–rapidity*, η_{det}, measured with respect to the $(0, 0, 0)$ nominal interaction point, from the *particle pseudo–rapidity*, η, measured with respect to the z position of the real vertex where the particle originated.

2.2.2 Tracking system

Tracking refers to the measurement of charged particles trajectories within the detector volume. This allows the determination of the charge and the momenta of the particles which are essential for the analysis presented in this thesis where mesons decaying to two charged particles are studied. In particular, the excellent CDF II tracking performance is key element of the analysis since, as it will be shown in the following chapters, permits a mass resolution of $\sim 8\,\text{GeV}/c^2$ for a D meson, allowing a good separation between all final states of interest.

Within an uniform axial magnetic field, the trajectory of a charged particle produced with non–zero initial velocity in the bending plane of the magnet is described

by an helix, which can be uniquely parameterized by the following set of equations:

$$\begin{cases} x = R\sin(2Cs + \phi_0) - (R + d_0)\sin\phi_0 \\ y = -R\cos(2Cs + \phi_0) + (R + d_0)\cos\phi_0 \\ z = z_0 + s\lambda \end{cases},$$

where, given the projected length along the track, s, one can find the corresponding (x, y, z) coordinates of the trajectory by means of five parameters (see Fig. 2.4):

C – signed half–curvature of the helix, defined as $C = q/2R$, where R is the radius of the helix and q is the charge of the track. This is directly related to the transverse momentum: $p_T = cB/(2|C|)$, where c is the speed of light and B is the magnetic field of the solenoid;

ϕ_0 – ϕ angle of the particle at the point of closest approach to the z axis;

d_0 – signed impact parameter, *i. e.* the radial distance of closest approach to the z axis, defined as $d_0 = q(\sqrt{x_c^2 + y_c^2} - R)$, where (x_c, y_c) are the coordinates of the center;

λ – the helix pitch, *i. e.* $\cot\theta$, where θ is the polar angle of the helix at the point of its closest approach to the z axis. This is directly related to the longitudinal component of the momentum: $p_z = p_T \cot\theta$;

z_0 – the z coordinate of the point of closest approach.

Charged particles leave small charge depositions as they pass through the alternative layers of the tracking system. Using a set of spatial measurements of these depositions ("hits"), pattern recognition algorithms can reconstruct the particle original trajectory measuring the five parameters of the helix that best match to the observed path in the tracking detector. At CDF II this is an integrated system consisting of three silicon inner sub–detectors and a large outer drift chamber, all contained in a 1.4 T magnetic field of a solenoid parallel to the beams and pointing in the negative z direction. The silicon detectors provide excellent impact parameter, azimuthal angle and z_0 resolution while the drift chamber provides excellent resolution of the curvature and ϕ_0. Together they provide a very accurate measurements of the helical paths of charged particles.

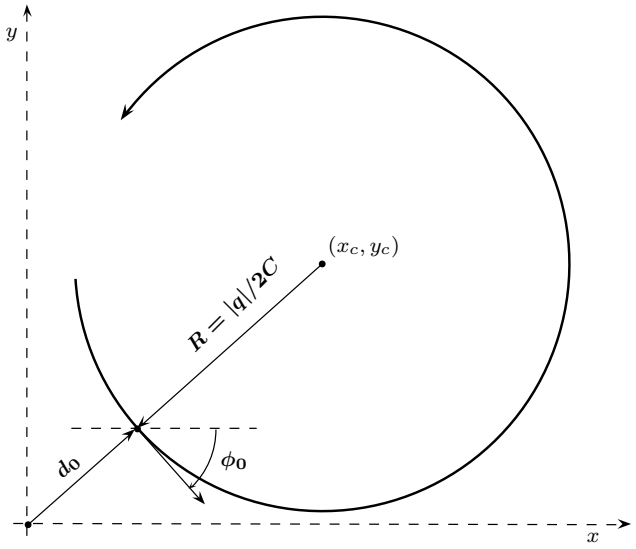

Figure 2.4: *Schematic view of a positively charged track in the plane transverse to an axial magnetic field* $\boldsymbol{B} = (0, 0, -B)$.

2.2.2.1 The inner silicon tracker

The CDF II silicon tracking system, as shown in Fig. 2.5 in both (r, ϕ) and (r, z) projections, is composed of three approximately cilindrical coaxial subsystems: the *Layer00* (L00), the *Silicon VerteX detector* (SVX II) and the *Intermediate Silicon Layer* (ISL).

L00 [60] is the innermost subsystem and consists of a one layer of single–sided, AC–coupled, microstrip silicon sensors installed at radii of 1.35 and 1.62 cm on a mechanical structure in direct contact with the beam pipe. It provides full azimuthal and $|z| \lesssim 47$ cm longitudinal coverage. Longitudinally adjacent sensors $(0.84 - 1.46\,\text{cm} \times 7.84\,\text{cm})$ are ganged in modules of 15.7 cm active–length arranged into twelve partially–overlapping ϕ sectors, and six longitudinal barrels. These radiation–tolerant sensors are biased to $\mathcal{O}(500\,\text{V})$, which allows full depletion after $\mathcal{O}(5\,\text{MRad})$ integrated radiation doses. The strips are parallel to the beam axis allowing sampling of tracks in the (r, ϕ) plane. The inter–strip implant pitch of 25 μm with floating alternate strips results in 50 μm read–out pitch. The analog signals of the 13 824 channels are fed via fine–pitch cables, up ~ 50 cm long, to the front–end electronics outside the tracking volume.

The SVX II [61] is a fine resolution silicon micro–strip vertex detector which pro-

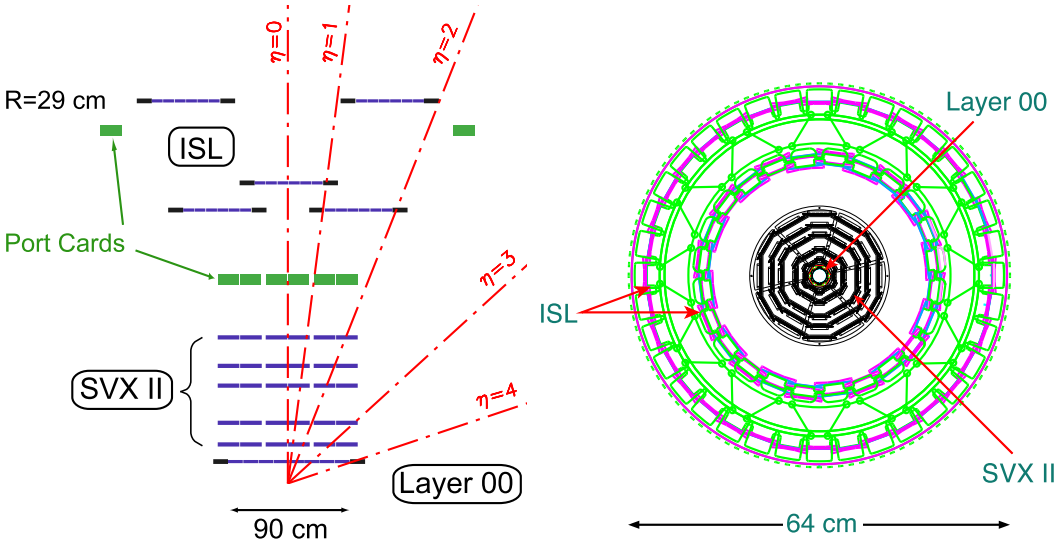

(a) (b)

Figure 2.5: *View of the CDF II silicon system, including the SVX II cooling bulkheads and ISL support structure, in the* (r, z) *(a) and* (r, ϕ) *(b) planes. The z scale is highly compressed.*

vides five three–dimensional samplings of tracks at 2.45, 4.1, 6.5, 8.2 and 10.1 cm (or, depending on the ϕ sector, at 2.5, 4.6, 7.1, 8.7 and 10.6 cm) of radial distance from the beam with full pseudo–rapidity coverage in the $|\eta_{\rm det}| \lesssim 2$ region. This corresponds to a length of $|z| \lesssim 96$ cm along the beam–line, sufficient to cover the $\sigma_z \approx 28$ cm longitudinal spread of the luminous region. The SVX II has a cylindrical geometry coaxial with the beam, and its mechanical layout is segmented in three 32 cm axial sections ("barrels") times twelve 30° azimuthal sectors ("wedges") times five equally–spaced radial layers. A small overlap between the edges of adjacent azimuthal sectors helps wedge–to–wedge alignment (see Fig. 2.5 (b)). Sensors in a single layer are arranged into independent longitudinal read–out units, called "ladders". Each ladder comprises two, double–sided sensors and a multi–layer electronic board, all glued on a carbon–fiber support. Front–end electronics, biasing circuits, and fan–out are located on the board that serves the pair of sensors whose strips are wire–bonded together resulting in a 15 cm active length. At a given radial layer and azimuth, each barrel contains pairs of ladders stacked length–wise head–to–head to keep the read–out electronic at the two outside extremities of the barrel. The active surface consists of double–sided, AC–coupled, $7.5\,{\rm cm} \times 1.5 - 5.8\,{\rm cm}$ sil-

icon sensors with microstrips implanted on a 300 μm thick, high resistivity bulk. Bias is applied through integrated poly–silicon resistors. On one side, all sensors have axial strips spaced by approximately 60–65 μm, for a precise reconstruction of the ϕ coordinate. On the reverse side, the following combination of read–out pitch (strip orientations with respect to the beam) is used: 141 μm (90°), 125.5 μm (90°), 60 μm(−1.2°), 141 μm (90°), 65 μm (1.2°), from the innermost to the outermost layer for reconstructing the z coordinate. A total of 405 504 electronics channels are used for SVX II.

The ISL [62] detector is placed at intermediate radial distance between the SVX II and the drift chamber and has polar coverage up to $|\eta_{\rm det}| < 2$ and a total length of 174 cm along z. At $|\eta_{\rm det}| \lesssim 1$ a single layer of silicon sensors is mounted on a cylindrical barrel at radius of 22.6 cm (or 23.1 cm). At $1 \lesssim |\eta_{\rm det}| \lesssim 2$ two layers of silicon sensors are arranged into two pairs of concentric barrels (inner and outer). In the inner (outer) barrel, staggered ladders alternate at radii of 19.7 and 20.2 cm (28.6 and 29 cm). One pair of barrels is installed in the forward region, the other one in the backward region. Each barrel is azimuthally divided into a 30° structure matching the SVX II segmentation. The basic read–out unit consists of an electronic board and three sensors ganged together resulting in a total active length of 25 cm. ISL employs 888 5.7 cm × 7.5(6.7) cm double–sided, 300 μm thick sensors. Each sensor has axial strips spaced by 112 μm on one side, and 1.2° angled strips spaced 112–146 μm on the reverse, for a total of 303 104 channels.

All 722 432 channels from the $\sim$ 7.0 m^2 silicon active–surface employ 5 644 radiation–tolerant, custom integrated read–out chips of the same type. This chip allows independent cycles of digitization of data and analog processing of subsequent data. The discriminated differential pulse from each channel is preamplified, digitized and propagated to the downstream data–acquisition. The ISL and the SVX II, whose mass is approximately 128 kg, share the carbon–fiber supporting structure.

The total amount of material in the silicon system, averaged over ϕ and z, varies roughly as $0.1X_0/\sin\theta$ in the $|\eta_{\rm det}| \lesssim 1$ region, and roughly doubles in $1 \lesssim |\eta_{\rm det}| \lesssim 2$ because of the presence of cables, cooling bulk–heads, and portions of the support frame.[3] The average amount of energy loss for a charged particle is roughly 9 MeV.

[3]The symbol X_0 indicates the radiation length.

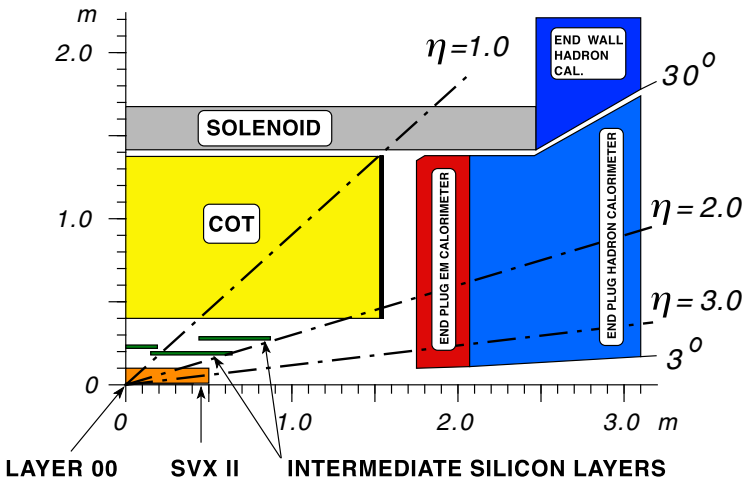

Figure 2.6: *Elevation view of one quadrant of the inner portion of the CDF II detector showing the tracking volume surrounded by the solenoid and the forward calorimeters.*

The total heat load of the silicon system is approximately 4 kW. To prevent thermal expansion, relative detector motion, increased leakage–current, and chip failure due to thermal heating, the silicon detectors and the associated front–end electronics are held at roughly constant temperature ranging from -6°C to -10°C for L00 and SVX II, and around 10°C for ISL, by an under–pressurized water and ethylene–glycol coolant flowing in aluminum pipes integrated in the supporting structures.[4]

The resolution on the hit position for all silicon sensors is about 11 μm in the (r, ϕ) plane, thus allowing to reach about 20 μm resolution on the impact parameter of high–p_T tracks which degrades to about 35 μm at 2 GeV/c. This precision provides a powerful help to identify long–lived hadrons containing heavy–flavored quarks already at trigger level.

2.2.2.2 The central outer tracker

A large multi–wire, open–cell drift chamber called the *Central Outer Tracker* (COT) [63] extends, in the central pseudo–rapidity region $|\eta_{\text{det}}| \lesssim 1$, the silicon tracking system (see Fig. 2.6).

The COT has an hollow–cylindrical geometry, its active volume spans from 43.4

[4]The pressure of the cooling fluid is maintained under the atmospheric pressure to prevent leaks in case of damaged cooling pipes.

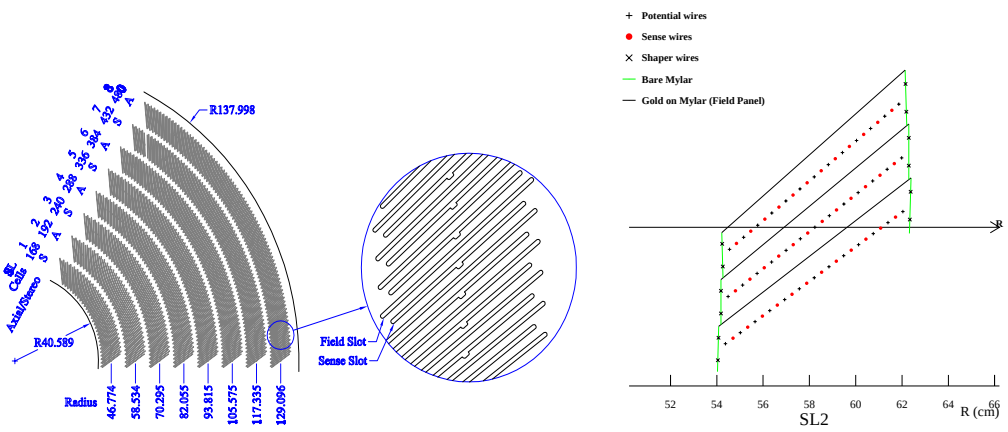

(a) (b)

Figure 2.7: *A 1/6 section of the COT end-plate (a); for each super-layer the total number of cells, the wire orientation (axial or stereo), and the average radius in cm are given; the enlargement shows in details the slot where the wire planes (sense and field) are installed. Sketch of an axial cross-section of three cells in the super-layer 2 (b); the arrow points into the radial direction.*

to 132.3 cm in radius and $|z| \lesssim 155$ cm in the axial direction. Arranged radially into eight "super–layers", it contains 96 planes of wires that run the length of the chamber between two end–plates (see Fig. 2.7 (a)). Each super–layer is divided into ϕ cells; within a cell, the trajectory of a charged particle is sampled at 12 radii (spaced 0.583 cm apart) where sense wires (anodes) are strung. Four super–layers employ sense–wires parallel to the beam axis, for the measurement of the hit coordinates in the (r, ϕ) plane. These are radially interleaved with four stereo super–layers whose wires are alternately canted at angles of 2° and -2° with respect to the beam–line. Combined read–out of stereo and axial super–layers allows the measurement of the (r, z) hit coordinates. Each super–layer is azimuthally segmented into open drift cells. Fig. 2.7 (b) shows the drift cell layout, which consists of a wire plane closed azimuthally by cathode sheets spaced approximately 2 cm apart. The wire plane contains sense wires alternating with field–shaping wires, which control the gain on the sense wires optimizing the electric field intensity. The cathode is a 6.35 μm thick Mylar sheet with vapor–deposited gold shared with the neighboring cell.[5] Innermost and outermost radial extremities of a cell (*i. e.* the boundaries

[5]Gold, used also for the wires, was chosen because of its good conductivity, high work function,

between super–layers) are closed both mechanically and electrostatically by Mylar strips with an additional field–shaping wire attached, the shaper wire.

Both the field sheet and the wire plane have a center ($z \approx 0$) support rod that limits motion due to electrostatic forces. Each wire plane contains 12 sense, 13 field–shaping and 4 shaper wires, all made of 40 μm diameter gold–plated tungsten. Wire planes are not aligned with the chamber radius: a $\zeta = 35°$ azimuthal tilt partially compensates for the Lorentz angle of the drifting electrons in the magnetic field.[6] The tilted–cell geometry helps in the drift velocity calibration, since every high–p_T (radial) track samples the full range of drift distances within each super-layer. Further benefit of the tilt is that the left-right ambiguity is resolved for particles coming from the z axis since the ghost track in each super–layer appears azimuthally rotated by $\arctan[2\tan(\zeta)] \approx 54°$, simplifying the pattern recognition problem. On the other hand this tilt angle causes an unavoidable difference in the reconstruction efficiencies between positively and negatively charged tracks which cross the sense wires with different incidence angle. Such difference is particularly enhanced for low–p_T tracks and introduces unwanted spurious asymmetries which need to be taken into account in all searches for CP violation.

A 50 : 50 gas admixture of argon and ethane bubbled through isopropyl alcohol (1.7%) flows in the active volume of the chamber with its pressure being continuously monitored by four probes. High voltage is applied to the sense and field–shaping wires to generate a 1.9 kV/cm drift electric field. This value, combined with the drift gas, results in a maximum drift–time of about 177 ns along a maximum drift–distance of 0.88 cm, allowing for read–out and processing of the COT data between two consecutive bunch–crossings. The average 180 kV/cm field present at the surface of the sense wire produces typical gains of $2 \cdot 10^4$. The sense wires are read–out by the front–end chip, which provides input protection, amplification, shaping, baseline restoration, discrimination and charge measurement. The input–charge information is encoded (logarithmically) in the signal width for dE/dx sampling and is fed to a

resistance to etching by positive ions, and low chemical reactivity.

[6] In the presence of crossed electric ($\boldsymbol{E}$) and magnetic ($\boldsymbol{B}$) fields, electrons drifting in a gas move at an angle ζ with respect to the electric field direction, given by $\zeta \approx \arctan\left(\frac{v(E,B=0)B}{kE}\right)$, where $v(E, B = 0)$ is the drift velocity without a magnetic field, and k is a $\mathcal{O}(1)$ empirical parameter that depends on the gas and on the electric field. A common solution for this problem consists in using tilted cells (*i. e.* tilted drift electric field) that compensate the Lorentz angle linearizing the time–to–distance relation.

time–to–digital converter that records leading and trailing–edge times of signal in 1 ns bins.

The COT single–hit resolution is 140 μm, including a 75 μm contribution from the $\sim$ 0.5 ns uncertainty on the measurement of the $p\bar{p}$ interaction time. Internal alignments of the COT cells are maintained within 10 μm using cosmic rays. Curvatures effects from gravitational and electrostatic sagging are under control within 0.5% by equalizing the difference of E/p between electrons and positrons as a function of $\cot\theta$.

2.2.2.3 Tracking algorithms and peformances

As already mentioned, the reconstruction of a charged particle trajectory consists in determining the helix parameters of Pag. 30 trough a fit of the reconstructed hits in the tracking sub–detectors with two basic steps: clustering multiple close measurements coming from the same track and pattern–recognition algorithm to joint the hits along the whole track arc. CDF employs several algorithms for tracks reconstruction depending on which component of the detector a particle travels through. The principal one, used to track the particles in the central region ($|\eta_{\rm det}| \lesssim 1$), is the *Outside–In* (OI). In this algorithm tracks are first reconstructed in the COT and then extrapolated inward to the silicon. This approach guarantees fast and efficient tracking with high purity. The greater radial distance of the COT with respect to the silicon tracker results in a lower track density and consequent fewer accidental combination of hits in the track reconstruction. Due to the limited COT coverage and the strict hits requirement (at least 4 out of 8 super–layers must contain a valid hit), tracking in the forward region requires different algorithms that are not described here because not used in this analysis. A concise overview of all the algorithms used at CDF is given in Refs. [64, 65, 66], in the following we briefly summarize how the OI works and which perfomances are achieved.

In the first step of pattern recognition, cells in the axial super–layers are searched for sets of 4 or more hits that can be fit to a straight line. Once these "segments" of hits are found, there are two approaches that can be followed to reconstruct a track. One approach is to link together the segments which are consistent with lying tangent to a common circular path[7]. The other approach is to constrain its circular

[7]The helical track, when projected onto the (r, ϕ) plane, is a circle.

fit to the beam–line. Once a circular path is found in the (r, ϕ) plane, segments and hits in the stereo super-layers are added depending on their proximity to the circular fit. This results in a three–dimensional track fit. Typically, if one algorithm fails to reconstruct a track, the other algorithm will not. Once a track is reconstructed in the COT, it is extrapolated inward to the silicon system. Based on the estimated errors on the track parameters, a three–dimensional "road" is formed around the extrapolated track. Starting from the outermost layer, and working inwards, silicon hits found inside the road are added to the track. As hits get added, the road gets narrowed, according to the knowledge of the updated track parameters and their covariance matrix. Reducing the width of the road reduces the chance of adding a wrong hit to the track, and also reduces the computation time. In the first pass of this algorithm, only axial hits are considered; while in a second pass, hits with stereo information are also added to the track. At the end, the track combination with the highest number of hits and lowest χ^2/ndf for the five parameters helix fit is kept.

COT efficiency for tracks with p_T larger (smaller) than $1\,\mathrm{GeV}/c$ is typically 98–99% (95%) depending on the isolation. The typical resolutions on track parameters are: $\sigma_{p_T}/p_T^2 \approx 0.15\%\,(\mathrm{GeV}/c)^{-1}$, $\sigma_{\phi_0} \approx 0.035°$, $\sigma_{d_0} \approx 250\,\mu\mathrm{m}$, $\sigma_\theta \approx 0.17°$ and $\sigma_{z_0} \approx 0.3\,\mathrm{cm}$ for tracks with no silicon information nor beam constrained. The silicon information improves the impact parameter resolution which, depending on the number (and radial distance) of the silicon hits, may reach $\sigma_{d_0} \approx 20\,\mu\mathrm{m}$ (not including the transverse beam size). This value, combined with the $\sim 30\,\mu\mathrm{m}$ transverse beam size, is sufficiently small with respect to the typical transverse decay–lengths of heavy flavors (a few hundred microns) to allow separation of their decay–vertices from production vertices. The silicon tracker improves also the stereo resolutions to $\sigma_\theta \approx 0.06°$ and $\sigma_{z_0} \approx 70\,\mu\mathrm{m}$, while the transverse momentum and the azimuthal resolutions remain approximately the same of COT–only tracks. Transverse momentum resolution can be further improved to about $\sigma_{p_T}/p_T^2 \approx 0.05\%\,(\mathrm{GeV}/c)^{-1}$ when tracks are beam contrained.

2.2.3 Trigger and data acquisition systems

The CDF II trigger system is a key element that makes this measurement possible. Identification of hadronic decays of heavy–flavored mesons is challenging in the

TeVatron collider environment due to the large inelastic $p\bar{p}$ cross section and high particle multiplicities at 1.96 TeV. In order to collect these events the trigger system must reject more than 99.99% of the collisions while retaining good efficiency for signal. In this section, we describe the CDF II trigger structure and the algorithms used in collecting the samples of hadronic D decays used in this analysis.

2.2.3.1 Overview

At the typical TeVatron instantaneous luminosity approximately $2.6 \cdot 10^6$ inelastic collisions per second occur, corresponding to one interaction per bunch–crossing on average. Since the read–out of the entire detector needs about 2 ms on average, after the acquisition of one event, another approximately 5 000 interactions would remain unrecorded. When an event recording is prevented because the system is busy with a different event or a different task, this is called deadtime.

Expressing the same concept in terms of information units, the average size of information associated to each event is 140 kB. Even in case of deadtime–less read–out of the detector, in order to record all events, an approximate throughput and storage rate of 350 GB/s would be needed, largely beyond the possibility of currently available technology[8].

The read–out system has to reduce the 2.3 MHz interaction–rate to the 100 Hz storage rate attainable at CDF II. The challenge for the whole system is to be smart enough to cut–off events that do not have the minimal requirements to be reconstructed or seem to contain well–known processes, that do not need further study, focusing the acquisition system on the interesting processes. Fig. 2.8 shows a scheme to explain how the information flows trough the different parts.

To suppress unwanted events, the CDF II *Data AcQuisition system* (DAQ) is segmented in three levels, each level receiving the accepted event from the previous one, and, provided with detector information with increasing complexity and with more time for processing, determines if one of a set of existing criteria is verified by the event.

Prior to any trigger level, the bunched structure of the beam is exploited to reject cosmic–ray events by gating the front–end electronics of all sub–detectors

[8]The maximum current storage rate is approximately 250 kb/s

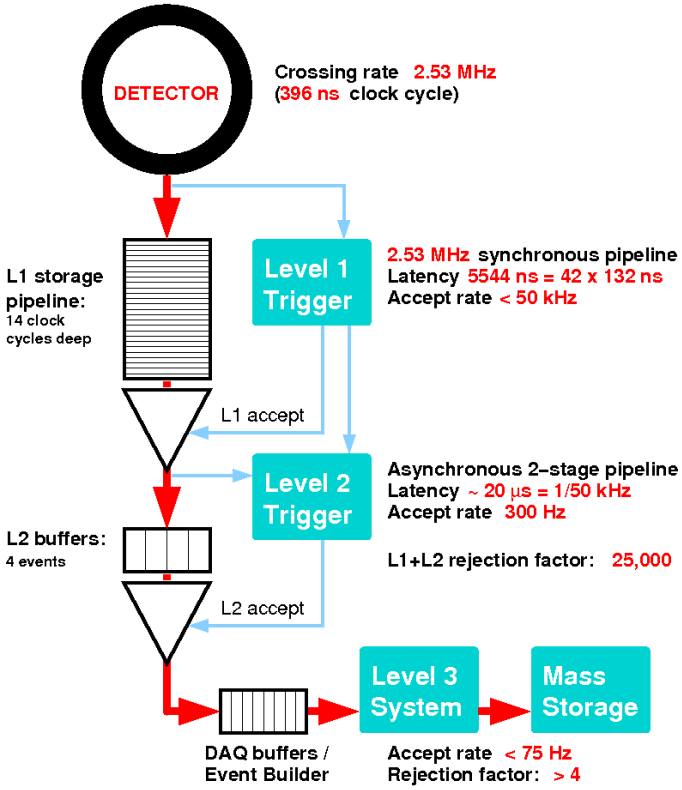

Figure 2.8: *Functional block diagram of the CDF II trigger and data acquisition systems.*

in correspondence of the bunch–crossing. The front–end electronics of each sub–detector, packaged in *Vesa Module Eurocard* (VME) modules hosted in about 120 crates, has a 42–cells deep pipeline synchronized with the TeVatron clock–cycle set to 132 ns. The TeVatron clock picks up a timing marker from the synchrotron RF and forwards this bunch–crossing signal to the trigger and to the front–end electronics. Since the inter–bunch time is 396 ns, three times the TeVatron clock–cycle, the pipeline can collect data corresponding to a maximum of 14 bunch–crossings. The pipeline depth gives the amount of time that *Level 1* (L1) trigger has to decide to accept or reject an event otherwise the buffer content is overwritten: $14 \times 396\,\text{ns} = 5.5\,\mu\text{s}$. An event accepted by the L1 is passed to the *Level 2* (L2) buffer, where the number of buffers in the pipeline is 4, that gives $4 \times 5.5\,\mu\text{s} = 22\,\mu\text{s}$. This means that if an event is accepted by the L1 and the L2 does not have a free buffer, deadtime will incur. L2 output rate is low enough to avoid in general deadtime problem in the connection between L2 and *Level 3* (L3).

At L1, a synchronous system of custom–designed hardware processes a simplified subset of data in three parallel streams to reconstruct coarse information from the calorimeters (total energy and presence of single towers over threshold), the COT (two–dimensional tracks in the transverse plane), and the muon system (*muon stubs*, *i. e.* segments of hits in the muon chambers). A decision stage combines the information from these low–resolution physics objects, called "primitives", into more sophisticated objects, *e. g.* track primitives are matched with muon stubs, or tower primitives, to form muon, electron, or jet[9] objects, which then undergo some basic selections.

At L2, an asynchronous system of custom–designed hardware processes the time–ordered events accepted by the L1. Additional information from the shower–maximum strip chambers in the central calorimeter [67] and from the axial layers of the SVX II detector is combined with L1 primitives to produce L2 primitives. A crude energy–clustering is done in the calorimeters by merging the energies in adjacent towers to the energy of a seed tower above threshold. L1 track primitives matched with consistent shower–maximum clusters provide refined electron candidates whose azimuthal position is known with 2° accuracy. Information from the (r, ϕ) sides of the SVX II is combined with L1 tracks primitives to form two–dimensional tracks with resolution similar to the off–line one. Finally, an array of programmable processors makes the trigger decision, while the L2 objects relative to the following event accepted at L1 are already being reconstructed.

The digitized output relative to the L2–accepted event reaches L3 via optical fibers and it is fragmented in all sub–detectors. It is collected by a custom hardware switch that arranges it in the proper order and transfers it to commercial computers, organized in a modular and parallelized structure of 16 subsystems. The ordered fragments are assembled in the *event record*, a block of data that univocally corresponds to a bunch–crossing and is ready for the analysis of the L3 software. The event reconstruction benefits from full detector information and improved resolution with respect to the preceding trigger levels, including three–dimensional track reconstruction, tight matching between tracks and calorimeter or muon information, and calibration information. If an event satisfies the L3 requirements, the

[9] A jet is a flow of observable secondary particles produced in a spatially collimated form, as a consequence of the hadronization of partons produced in the hard collision.

corresponding event record is transferred to mass storage at a maximum rate of 20 MB/s. A fraction of the output is monitored in real time to search for detector malfunctions, to derive calibrations constants and to graphically display events. The L3 decision is made after the full reconstruction of the event is completed and the integrity of its data is checked, a process that takes a few milliseconds.

2.2.3.2 Trigger on displaced tracks

In this section we describe that part of the CDF II trigger system which provides the ability to recognize tracks displaced from the $p\bar{p}$ interaction point. Displaced tracks are those that have impact parameter inconsistent with having originated from the $p\bar{p}$ interaction point, such as those arising from the decay of weakly–decaying heavy hadrons with sufficient transverse momentum.

Using information from the COT, at L1, the *eXtremely Fast Tracker* (XFT) [68, 69] reconstructs trajectories of charged particles in the (r, ϕ) plane for each proton–antiproton bunch crossing. The XFT is a custom processor that uses pattern matching to first identify short segments of tracks and then to link them into full–length tracks. After classifying the hits of the four axial super–layers in "prompt" (0–66 ns) or "delayed" hits (67–220 ns), depending upon the observed drift–time within the cell, track segments are reconstructed in each axial super–layer. A pattern–matching algorithm searches for coincidences between the observed combinations of hits in each super–layer (a minimum of 11 out of 12 hits is required) and a set of predetermined patterns. If a coincidence between segments crossing four super–layers is found, two–dimensional XFT–tracks are reconstructed by linking the segments. The segments are compared with a set of about 2 400 predetermined patterns corresponding to all tracks with $p_T \gtrsim 1.5\,\mathrm{GeV}/c$ originating from the beam–line. The comparison proceeds in parallel in each of the 288 azimuthal 1.25° sectors in which XFT logically divides the chamber. If no track is found using all four super–layers, then the best track found in the innermost three super–layers is output. The track–finding efficiency and the fake–rate with respect to the off–line tracks depend on the instantaneous luminosity and were measured to be about 96% and 3%, respectively, at $\mathscr{L} \simeq 10^{31}\,\mathrm{cm}^{-2}\mathrm{s}^{-1}$. The observed momentum resolution is $\sigma_{p_T}/p_T^2 \approx 1.7\%\,(\mathrm{GeV}/c)^{-1}$, and the azimuthal resolution is $\sigma_{\phi_6} \approx 0.3°$, where ϕ_6 is the azimuthal angle of the track measured at the sixth COT super–layer, located

at 106 cm radius from the beam–line.

Events are selected for further processing when two XFT–tracks satisfying trigger criteria on basic variables are found. The variables are the product of any combination of two particles' charges (opposite or same sign), the opening angle of the two tracks in the transverse plane ($\Delta\phi_6$), the two particles' transverse momenta and their scalar sum.

At L2 the information from the SVX II detector is incorporated into the trigger track reconstruction by the *Silicon Vertex Trigger* (SVT) [70, 71]. Charge clusters in the silicon, which SVT finds by converting a list of channel numbers and pulse heights into charge–weighed hit centroids, are used by a pattern recognition algorithm, which is formed of two subsequent stages. First, a low–resolution stage is implemented by grouping together adjacent detector channels into "super–bins". Their width in the azimuthal direction is programmable, with 250–700 μm typical values. A set containing about 95% of all super–bin combinations compatible with the trajectory of a charged particle with $p_T \gtrsim 2\,\mathrm{GeV}/c$ originated from the beam–line ("patterns") is calculated in advance from simulation and stored in a special design memories called *Associative Memories* (AMs). For each azimuthal sector, the 32 768 most probable patterns are stored. Online, an algorithm detects low–resolution candidate tracks, called "roads", by matching super–bins containing hits with the stored patterns. A road is a combination four excited super–bins in different SVX II layers plus the XFT track parameters, which are logically treated as additional hits (see Fig. 2.9 (a)).

In the AMs system, maximum parallelism is exploited to speed–up the processing, using a working principle similar to the one of the bingo game: while the silicon hits are being read out, each "player" marks the matching super–bins on his "score–card"; each "bingo" corresponds to a road and is retained for further processing. A maximum of 64 roads per event, each one having a maximum of 8 hits per super–bin, is output. At this stage, pattern recognition is done during detector read–out with no additional processing time. The resolution is coarse enough to reduce the fraction of accidental combinations, but fine enough to separate most tracks. Once a track is confined to a road, most of the pattern recognition is done, leaving the remaining ambiguities, as multiple hits in the same super–bin, to the stage of track fitting.

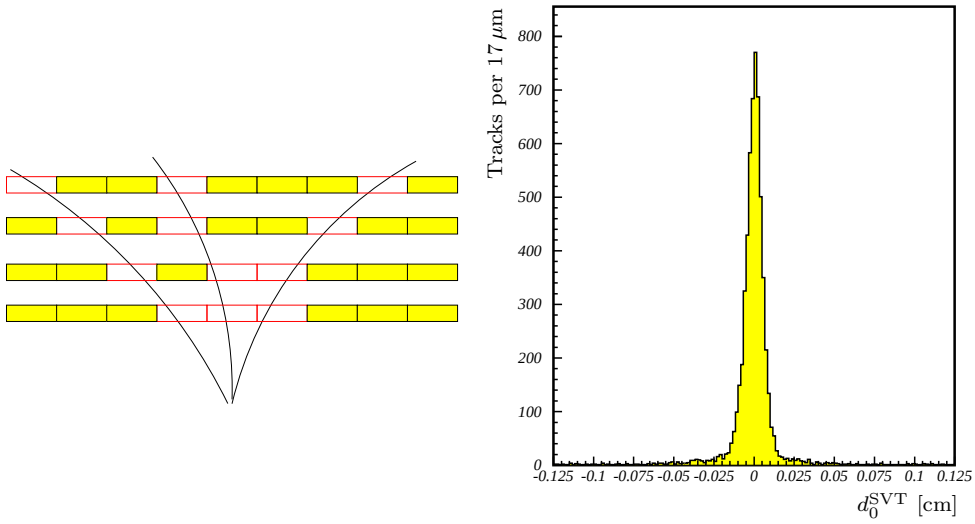

(a) (b)

Figure 2.9: *Schematic illustration of combinations of super–bins (in the transverse plane) corresponding to the passage of charged particles in four radial silicon layers (a). Impact parameter distribution as measured by the SVT (b).*

In principle, no exact linear relation exists between the transverse parameters of a track in a solenoidal field, and the coordinates at which the track intersects a radial set of flat detector planes. But for $p_T \gtrsim 2\,\mathrm{GeV}/c$, $|d_0| \lesssim 1\,\mathrm{mm}$ and $|\Delta\phi_0| \lesssim 150°$, a linear fit biases the reconstructed d_0 by at most a few percent. The track–fitting process exploits this feature by expanding the non–linear constraints and the parameters of the real track to first order with respect to the reference track associated to each road. A linear expansion in the hit positions of both the track parameters and the χ^2 is used. The fit process is thus reduced to computing a few scalar products, which is done within 250 ns per track. The needed constants, which depend on detector geometry and alignments, are evaluated in advance and stored in an internal memory. The output of the SVT are the reconstructed parameters of the two–dimensional track in the transverse plane: ϕ_0, p_T and d_0. The list of parameters for all found tracks is sent to L2 for trigger decision.

The SVT measures the impact parameter with a r.m.s. width $\sigma_{d_0^{\mathrm{SVT}}} \approx 35\,\mu\mathrm{m}$, with an average latency of $24\,\mu$s, $9\,\mu$s of which being spent waiting for the start of the read–out of silicon data. This resolution is comparable with the off–line one, for

tracks not using L00 hits, and yields a distribution of impact parameter of prompt tracks with respect to the z axis with $\sigma_{d_0^{\rm SVT}} \approx 47\,\mu$m when combined with the transverse beam–spot size, as shown in Fig. 2.9 (b). The SVT efficiency is higher than 85%.[10]

The impact parameter is a quantity measured with respect to the beam. If the actual beam position in the transverse plane is shifted by an amount $d_{\rm beam}$ with respect to the origin of the SVT reference frame, all prompt tracks appear to SVT as having $\mathcal{O}(d_{\rm beam})$ impact parameters. This is relevant since the beam is usually displaced from its nominal $(0, 0, z)$ position. Between TeVatron stores, $\mathcal{O}(500\,\mu$m) displacements in the transverse plane and $\mathcal{O}(100\,\mu$rad) slopes with respect to the detector axis may occur. In addition, the beam can drift by $\mathcal{O}(10\,\mu$m) in the transverse plane even during a single store. However, a simple geometric relation prescribes that the impact parameter of a track, calculated with respect to a point displaced from its production vertex, is a sinusoidal function of its azimuthal coordinate:

$$d_0 = y_0 \cos\phi_0 - x_0 \sin\phi_0, \tag{2.1}$$

where (x_0, y_0) are the coordinates of the production vertex. Using Eq. (2.1), SVT measures the actual coordinates of the beam position with respect to the detector system and subtracts them from the measured impact parameters, in order to provide physical impact parameters. Using about 10^5 tracks every 30 seconds, six transverse beam positions (one for each SVX II semi–barrel) are determined on–line. The six samplings (one for each SVX II barrel) along the z direction provide a measurement of the slope of the beam with respect to the nominal z axis.

For the proper measurement of impact parameters, the beam slope is more harmful than the transverse drift, because it breaks the cylindrical symmetry of the system. The SVT does not have access to the z_0 coordinate of tracks. For each track, only the longitudinal coordinate of the SVX II half–barrel that detected the track is known. But half–barrels are too long (16 cm) to allow for a reliable correction of the beam slope. When significant slopes are observed, the TeVatron beam division is alerted and they apply a corrective action on the magnets.

Beam mis–alignments affect also the SVT efficiency. Owing to its modular structure and to the limited size of the pattern bank, the SVT can not identify

[10] This efficiency is defined as the ratio between the number of tracks reconstructed by SVT and all XFT–matched off–line silicon tracks that are of physics analysis quality.

charged particles that cross adjacent SVX II wedges. In normal conditions, these are only a small fraction of $p_T > 2\,\mathrm{GeV}/c$ particles, typically due to the bending trajectory and of the finite beam–spot size. However, in presence of beam offset from the nominal position, this fraction significantly increases, thus inducing SVT inefficiency.

The L2 trigger selections used in this analysis typically requires two SVT–tracks with impact parameter greater than $100\,\mu$m and smaller than 1 mm. In addition, the L2 trigger requires the transverse decay length, L_{xy}, to exceed $200\,\mu$m, where L_{xy} is calculated as the projection of the vector from the primary vertex to the two track vertex in the transverse plane along the vectorial sum of the transverse momenta of the tracks. The trigger based on SVT collects large quantities of long–lived D hadrons, rejecting most part of the prompt background. However, through its impact–parameter–based selection, the SVT trigger also biases the observed proper decay time distribution. This has important consequences on the results of this analysis as it will be shown in the following chapters.

The L3 trigger, as already mentioned, uses a full reconstruction of the event with all detector information, but uses a simpler tracking algorithm and preliminary calibrations relative to the ones used off–line and retests the criteria imposed by L2. In addition, the difference in z of the two tracks at the point of minimum distance from the primary vertex, Δz_0, is required not to exceed 5 cm, removing events where the pair of tracks originate from different collisions within the same crossing of p and $\bar{p}$ bunches.

Over the course of a TeVatron store, the available trigger bandwidth varies because trigger rates fall as instantaneous luminosity falls. Higher trigger rates at high luminosity arise from both a larger rate for real physics processes as well as a larger fake trigger rate due to multiple $p\bar{p}$ interactions. To fully exploit the available trigger bandwidth, we employ three main variants of the displaced–tracks trigger. The three selections are summarized in Tab. 2.1 and are referred to as the low–p_T, medium–p_T and high–p_T selections, according to their requirements on minimum transverse momentum. At high luminosity, the higher purity, but less efficient, high–p_T selection is employed. As the luminosity decreases over the course of a store, trigger bandwidth becomes available and the other selections are utilized to fill the available trigger bandwidth and maximize the charm yield.

Version	Level 1	Level 2	Level 3
High–p_T	$p_T > 2.5\,\mathrm{GeV}/c$	$p_T > 2.5\,\mathrm{GeV}/c$	$p_T > 2.5\,\mathrm{GeV}/c$
	Opposite charge	Opposite charge	Opposite charge
	$\Delta\phi_6 < 90°$	$2° < \Delta\phi_0 < 90°$	$2° < \Delta\phi_0 < 90°$
	$\sum p_T > 6.5\,\mathrm{GeV}/c$	$\sum p_T > 6.5\,\mathrm{GeV}/c$	$\sum p_T > 6.5\,\mathrm{GeV}/c$
		$0.1 < d_0 < 1\,\mathrm{mm}$	$0.1 < d_0 < 1\,\mathrm{mm}$
		$L_{xy} > 200\,\mu\mathrm{m}$	$L_{xy} > 200\,\mu\mathrm{m}$
			$\lvert\Delta z_0\rvert < 5\,\mathrm{cm}$
			$\lvert\eta\rvert < 1.2$
Medium–p_T	$p_T > 2\,\mathrm{GeV}/c$	$p_T > 2\,\mathrm{GeV}/c$	$p_T > 2\,\mathrm{GeV}/c$
	Opposite charge	Opposite charge	Opposite charge
	$\Delta\phi_6 < 90°$	$2° < \Delta\phi_0 < 90°$	$2° < \Delta\phi_0 < 90°$
	$\sum p_T > 5.5\,\mathrm{GeV}/c$	$\sum p_T > 5.5\,\mathrm{GeV}/c$	$\sum p_T > 5.5\,\mathrm{GeV}/c$
		$0.1 < d_0 < 1\,\mathrm{mm}$	$0.1 < d_0 < 1\,\mathrm{mm}$
		$L_{xy} > 200\,\mu\mathrm{m}$	$L_{xy} > 200\,\mu\mathrm{m}$
			$\lvert\Delta z_0\rvert < 5\,\mathrm{cm}$
			$\lvert\eta\rvert < 1.2$
Low–p_T	$p_T > 2\,\mathrm{GeV}/c$	$p_T > 2\,\mathrm{GeV}/c$	$p_T > 2\,\mathrm{GeV}/c$
	$\Delta\phi_6 < 90°$	$2° < \Delta\phi_0 < 90°$	$2° < \Delta\phi_0 < 90°$
	$\sum p_T > 4\,\mathrm{GeV}/c$	$\sum p_T > 4\,\mathrm{GeV}/c$	$\sum p_T > 4\,\mathrm{GeV}/c$
		$0.1 < d_0 < 1\,\mathrm{mm}$	$0.1 < d_0 < 1\,\mathrm{mm}$
		$L_{xy} > 200\,\mu\mathrm{m}$	$L_{xy} > 200\,\mu\mathrm{m}$
			$\lvert\Delta z_0\rvert < 5\,\mathrm{cm}$
			$\lvert\eta\rvert < 1.2$

Table 2.1: Selections for the three versions of the displaced–tracks trigger used in this analysis. The criteria refer to track–pairs. The p_T, d_0 and η requirements are applied to both tracks. The $\sum p_T$ refers to the scalar sum of the p_T of the two tracks.

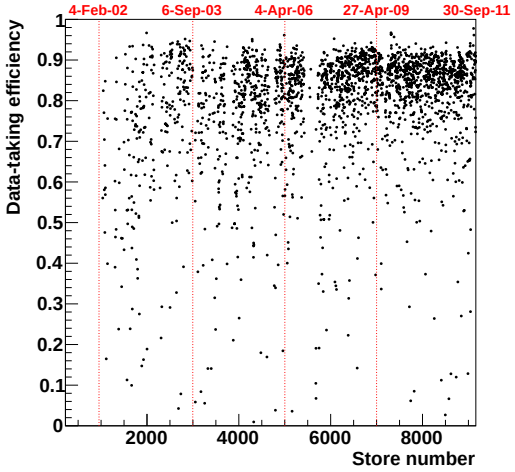

Figure 2.10: *Data–taking efficiency as a function of store number/time.*

The rates are controlled by the application of prescaling, which rejects a predefined fraction of events accepted by each trigger selection dependent on the instantaneous luminosity.

2.2.4 Operations and data quality

The data–taking efficiency is plotted in Fig. 2.10 as a function of time. The average over the whole Run II is about 85%. The inefficiency is approximately equally shared in a 5% arising at the beginning of the store, when the detector is not powered while waiting for stable beam conditions, a 5% due to trigger deadtime, and a 5% due to unexpected detector or DAQ problems.

Each time that at least one of the trigger paths fires, an "event" is labeled with a progressive number. Events are grouped into runs, *i. e.* periods of continuous data–taking in constant configurations of trigger table, set of active sub–detectors and so forth.[11] Several parameters of the operations (*e. g.* beam–line position and slope, set of calibrations, etc.) are stored in the database on a run–averaged format.

All data manipulations occurring some time after the data are written to permanent memories are referred to as off–line processes, as opposed to the on–line

[11] The data acquisition might need to be interrupted and recovered for several motivations, including the need for enabling or disabling a sub–detector, the need for a change in the trigger table, a problem in the DAQ chain and so forth.

operations that take place in real time, during the data–taking. The most important off–line operation is the processing with a centralized *production* analysis that generates collections of high–level physics objects suitable for analysis, such as tracks, vertexes, muons, electrons, jets, etc. from low–level information such as hits in the tracking sub–detectors, muon stubs, fired calorimeter towers, etc. During the production, more precise information about the detector conditions (*e. g.* calibrations, beam–line positions, alignment constants, masks of malfunctioning detector–channels, etc.) and more sophisticated algorithms are used than those ones available at the L3 of the trigger. The production may be repeated when improved detector information or reconstruction algorithms become available.

To ensure homogeneous data–taking conditions, each run undergoes a quality inspection. On–line shift operators, off–line production operators, and sub–detector experts certify in what fraction of data the running conditions for all relevant sub–detectors are compliant to physics–quality standards. When detectable problems of the detector occur, the data–taking is quickly stopped, so very short runs are likely to contain corrupted data. Runs with fewer than 10^8 live TeVatron clock–cycles, or fewer than 10^4 (10^3) L1 (L2) accepts, or containing data corresponding to an integrated luminosity $\int \mathscr{L}\, dt < 1\,\text{nb}$ are excluded from physics analysis. On–line shift operators further exclude the runs in which temporary or test trigger tables were used.[12] Runs whose data underwent problems or software crashes during the production are excluded off–line.

Accurate integrated luminosity measurements are ensured in physics–quality data by requiring the Cherenkov luminosity monitor [72] to be operative during the data–taking and by verifying that a set of luminosity and beam–monitor probe quantities are within the expected ranges. Shift operators ensure that L1 and L2 triggers operate correctly and that the rate of SVX II data corruption errors is smaller than 1%.[13] SVT experts verify that the on–line fit and subtraction of the beam position is done correctly and that the SVT occupancy is within the expected limits. In addition, higher level quantities, such as event yields of $J/\psi \to \mu^+\mu^-$

[12] It is sometimes necessary to test new configurations of the trigger selections in a real data–taking condition to monitor trigger rates, performance and so on.

[13] The read–out of the silicon detector and the proper integration of the information in the on–line infrastructure is a complex operation which, occasionally, leads to a certain fraction of data to be improperly processed.

and $D^0 \to K^-\pi^+$ decays are monitored on–line and are required to be within the expected ranges. For analyses using COT information, the minimum integrated luminosity required is 10 nb and the fraction of noisy COT channels is required to be smaller than 1%.

Chapter 3

Analysis Overview

This chapter describes the fully data–driven method, proposed and developed in this thesis, to measure the time–integrated CP asymmetries in $D^0 \to h^+h^-$ decays at CDF with the control of systematics uncertainties at the permille level. It also present the validation of this method on Monte Carlo simulated samples.

3.1 Introduction to the problem

As mentioned in Sect. 1.4, searches for CP violation in the charm sector have only recently started reaching interesting level of sensitivity below the 1% in some decay modes. The measurement described in this thesis has the goal to increase such sensitivity to the 0.1% level studing the singly–Cabibbo–suppressed D^0 decays to CP final states.

In order to do so not only larger samples but also very good control over the systematic uncertainties will be needed. These uncertainties are dominated by the uncertainties in asymmetries in the detection and reconstruction of particles of opposite charge. Estimation of these factors used to rely upon Monte Carlo simulated studies, with hard–to–justify assumptions about charge dependent interaction effects, resulting in systematic uncertainties in $\mathcal{A}_{\rm CP}$'s in the $1-5\%$ range. In the past years, new insights in using real data rather than simulations have led the B–factories to reduce these uncertainties down to the 0.5% level.

The work presented in this thesis develops a completely data–driven methodology to measure $\mathcal{A}_{\rm CP}(D^0 \to h^+h^-)$ which naturally suppress the systematics induced by detector effects. In the following we outline the details of this method specifically designed for the CDF experimental environment.

3.2 Detector induced charge asymmetries in D^*–tagged $D^0 \to h^+h^-$ decays at CDF

In an ideal experimental apparatus, the CP–violating asymmetries of our interest could be measured by simply determining the asymmetry between the number of detected particles of opposite charm content

$$A(D^0) = \frac{N^{\rm obs}_{D^0} - N^{\rm obs}_{\overline{D}^0}}{N^{\rm obs}_{D^0} + N^{\rm obs}_{\overline{D}^0}}, \tag{3.1}$$

where $N^{\rm obs}_{\overline{(D)}^0}$ is the observed number of $\overline{(D)}^0$ mesons decaying into the selected final state ($\pi^+\pi^-$ or K^+K^-). The main experimental difficulty of this measurement comes from the small differences in the detection efficiency of a real apparatus for tracks of opposite charge which lead, if not properly taken into account, to spuriously–measured charge asymmetries. Relevant instrumental effects include differences in interaction cross sections with matter between positive and negative low–momentum hadrons and the geometry of the tracking system. As already mentioned in Sect. 2.2.2.2, the CDF II drift chamber (COT) layout is intrinsically charge asymmetric because of a 35° tilt angle between the cell orientation and the radial direction, designed to partially correct for deviation in charge drift direction caused by crossed electric and magnetic fields (see Fig. 2.7). In the COT, different detection efficiencies are expected for positive and negative low–momentum tracks (especially for soft pions, in our case), which induce an instrumental asymmetry in the number of reconstructed D^*–tagged D^0 and $\overline{D}^0$ mesons. Additional asymmetries may originate in slightly different performance between positive and negative tracks in pattern–reconstruction and track–fitting algorithms. The combined effect of these is a net asymmetry, which is p_T–dependent, in the range of a few percent, as shown in Fig. 3.1 (a), which must be corrected to better than one permille to match the expected statistical precision of the present measurement.

We extract the physical value of $\mathcal{A}_{\rm CP}(D^0 \to h^+h^-)$ using a fully data–driven method, based on an appropriate correction determined with the help of independent control samples of D^*–tagged and untagged Cabibbo–favored $D^0 \to K^-\pi^+$ decays.

Because of the similar decay topology the Cabibbo–favored $D^{*+} \to D^0(\to K^-\pi^+)\pi^+_s$ mode exhibits instrumental asymmetries analogous to the singly–Cabibbo–

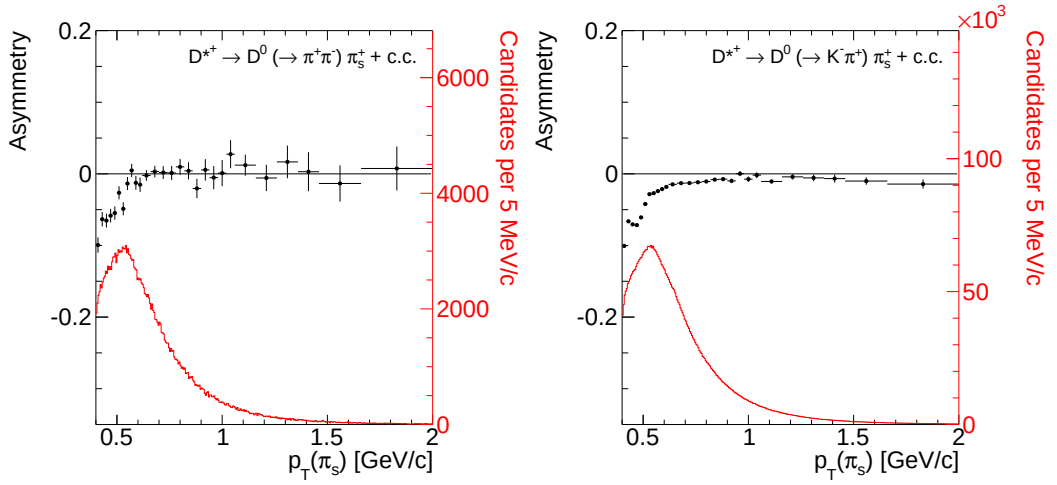

(a) (b)

Figure 3.1: *Observed asymmetry between the number of reconstructed D^{*+} and D^{*-} mesons as a function of the soft pion's transverse momentum for a pure sample of $D^{*+} \to D^0(\to \pi^+\pi^-)\pi_s^+$ (a) and $D^{*+} \to D^0(\to K^-\pi^+)\pi_s^+$ (b) decays. The soft pion transverse momentum spectrum is also shown superimposed.*

suppressed one, with the exception of an additional detector–induced contribution to the observed asymmetry due to the difference between the reconstruction efficiencies of a $K^-\pi^+$ versus $K^+\pi^-$ pair of final state particles, as shown, for example, in Fig. 3.1 (b). In order to extract the correction for the detector induced asymmetry in the soft pion reconstruction from the sample of D^*–tagged Cabibbo–favored decays, this additional effect needs to be taken into account. In our analysis we do that comparing the asymmetry of D^*–tagged $D^0 \to K^-\pi^+$ decays with the observed asymmetry in the untagged $D^0 \to K^-\pi^+$ decays where, instead, no effect from the soft pion is present.

The exact procedure of how the full correction is performed, thus allowing to measure the CP–violating asymmetries in $D^0 \to h^+h^-$ decays at CDF, is described in the following section.

3.3 Cancellation of detector asymmetries

We consider the following three event samples: D^*–tagged $D^0 \to h^+h^-$ decays (or simply hh^*), D^*–tagged $D^0 \to K^-\pi^+$ decays ($K\pi^*$) and untagged $D^0 \to K^-\pi^+$

decays ($K\pi$). We show in this section that an appropriate combination of asymmetries, measured in these three samples yields the true physical value of $\mathcal{A}_{\rm CP}$ with a high degree of suppression of detector asymmetries, and as a consequence, a very small systematic uncertainty coming from residual, uncompensated effects. In our discussion we always refer to the *true* values of kinematical variables of particles when not otherwise indicated. The *measured* quantities, affected by experimental uncertainties, play no role here since we are only interested in counting particles and all detection efficiencies are assumed to be dependent on true quantities only.

Assuming factorization of efficiencies for reconstructing the neutral charmed meson and the soft pion, the number of observed D^*–tagged $\overset{(-)}{D}{}^0 \to h^+h^-$ is[1]

$$N^{\rm obs}_{\overset{(-)}{D}{}^0} = \frac{N_{D^*}}{2}\ \mathcal{B}(D^* \to D^0\pi)\ \mathcal{B}(\overset{(-)}{D}{}^0 \to h^+h^-) \int d\boldsymbol{p}_* d\boldsymbol{p}_s d\boldsymbol{p}_{h^+} d\boldsymbol{p}_{h^-}\ \varrho_{*\pm}(\boldsymbol{p}_*)\ \varrho_{hh^*}(\boldsymbol{p}_{h^+}, \boldsymbol{p}_{h^-}, \boldsymbol{p}_s \mid \boldsymbol{p}_*)\ \varepsilon_{hh}(\boldsymbol{p}_{h^+}, \boldsymbol{p}_{h^-})\ \varepsilon_{s\pm}(\boldsymbol{p}_s),$$

where N_{D^*} is the total number of D^{*+} and D^{*-} mesons produced and we assumed $N_{D^{*+}} = N_{D^{*-}}$ as expected by CP–conserving strong $c\bar{c}$ pair–production in $p\bar{p}$ collisions; $\mathcal{B}(D^* \to D^0\pi)$ and $\mathcal{B}(\overset{(-)}{D}{}^0 \to h^+h^-)$ are the branching fractions of $D^{*\pm} \to \overset{(-)}{D}{}^0\pi^\pm$, assumed to be charge symmetric being governed by strong interactions, and $\overset{(-)}{D}{}^0 \to h^+h^-$ respectively; $\boldsymbol{p}_*$, $\boldsymbol{p}_s$ and $\boldsymbol{p}_{h^\pm}$ are the three–momenta of the D^*, π_s and $h^\pm$ respectively; $\varrho_{*\pm}$ is the densities in phase space of $D^{*\pm}$ mesons; ϱ_{hh^*} is the density in phase space of the soft pion and the h^+h^- pair from D^0 decay; ε_{hh} is the detection efficiency of the h^+h^- pair from the D^0 decay and $\varepsilon_{s\pm}$ is the detection efficiencies of the positive/negative soft pion. Densities are normalized to unity, *i. e.* $\int d\boldsymbol{p}_* \varrho_{*\pm}(\boldsymbol{p}_*) = 1$ and $\int d\boldsymbol{p}_s d\boldsymbol{p}_{h^+} d\boldsymbol{p}_{h^-} \varrho_{hh^*}(\boldsymbol{p}_{h^+}, \boldsymbol{p}_{h^-}, \boldsymbol{p}_s \mid \boldsymbol{p}_*) = 1$, where the last relation holds for each $\boldsymbol{p}_*$.

The difference between charm and anticharm event yields is therefore

$$N^{\rm obs}_{D^0} - N^{\rm obs}_{\overline{D}{}^0} = N_{D^*}\ \mathcal{B}(D^* \to D^0\pi)\ \overline{\mathcal{B}}(D^0 \to hh) \int d\boldsymbol{p}_* d\boldsymbol{p}_s d\boldsymbol{p}_{h^+} d\boldsymbol{p}_{h^-} \varrho_*(\boldsymbol{p}_*)\ \varrho_{hh^*}(\boldsymbol{p}_{h^+}, \boldsymbol{p}_{h^-}, \boldsymbol{p}_s \mid \boldsymbol{p}_*)\ \varepsilon_{hh}(\boldsymbol{p}_{h^+}, \boldsymbol{p}_{h^-})\ \varepsilon_s(\boldsymbol{p}_s) \left[\mathcal{A}_{\rm CP} + \delta\varrho_*(\boldsymbol{p}_*) + \delta\varepsilon_s(\boldsymbol{p}_s) + \mathcal{A}_{\rm CP}\delta\varrho_*(\boldsymbol{p}_*)\delta\varepsilon_s(\boldsymbol{p}_s)\right], \quad (3.2)$$

where we introduced the time–integrated $\mathcal{A}_{\rm CP}$ defined in Eq. (1.25) and we have

[1] The symbol $\overset{(-)}{D}{}^0$ mens that in the following expressions the positive sign of $\pm$ is associate with the D^0, while the negative sign is associated with $\overline{D}{}^0$.

defined the following additional quantities:

$$\overline{\mathcal{B}}(D^0 \to hh) = \frac{\mathcal{B}(D^0 \to h^+h^-) + \mathcal{B}(\overline{D}^0 \to h^+h^-)}{2},$$

$$\varrho_* = \frac{\varrho_{*+} + \varrho_{*-}}{2}, \qquad \delta\varrho_* = \frac{\varrho_{*+} - \varrho_{*-}}{\varrho_{*+} + \varrho_{*-}},$$
$$\varepsilon_s = \frac{\varepsilon_{s+} + \varepsilon_{s-}}{2}, \qquad \delta\varepsilon_s = \frac{\varepsilon_{s+} - \varepsilon_{s-}}{\varepsilon_{s+} + \varepsilon_{s-}}.$$

In general $\varrho_{*+}(\boldsymbol{p}_*) \neq \varrho_{*-}(\boldsymbol{p}_*)$ because correlations with the $p\bar{p}$ initial state may induce pseudo–rapidity–dependent asymmetries between the number of produced charm and anticharm mesons. However, such asymmetries are constrained by CP conservation to be antisymmetric in η. It follows that the second and fourth term in square brackets of Eq. (3.2) vanish when integrated over a $\boldsymbol{p}_*$ domain symmetric in η, therefore we finally obtain

$$N^{\rm obs}_{D^0} - N^{\rm obs}_{\overline{D}^0} = N_{D^*}\mathcal{B}(D^* \to D^0\pi)\overline{\mathcal{B}}(D^0 \to hh) \int d\boldsymbol{p}_* d\boldsymbol{p}_s d\boldsymbol{p}_{h^+} d\boldsymbol{p}_{h^-} \left[\mathcal{A}_{\rm CP} + \delta\varepsilon_s(\boldsymbol{p}_s)\right].$$

In a similar way we obtain

$$N^{\rm obs}_{D^0} + N^{\rm obs}_{\overline{D}^0} = N_{D^*}\ \mathcal{B}(D^* \to D^0\pi)\ \overline{\mathcal{B}}(D^0 \to hh) \int d\boldsymbol{p}_* d\boldsymbol{p}_s d\boldsymbol{p}_{h^+} d\boldsymbol{p}_{h^-}$$
$$\varrho_*(\boldsymbol{p}_*)\ \varrho_{hh^*}(\boldsymbol{p}_{h^+}, \boldsymbol{p}_{h^-}, \boldsymbol{p}_s \mid \boldsymbol{p}_*)\ \varepsilon_{hh}(\boldsymbol{p}_{h^+}, \boldsymbol{p}_{h^-})\ \varepsilon_s(\boldsymbol{p}_s)$$
$$\left[1 + \mathcal{A}_{\rm CP}\delta\varepsilon_s(\boldsymbol{p}_s) + \mathcal{A}_{\rm CP}\delta\varrho_*(\boldsymbol{p}_*) + \delta\varrho_*(\boldsymbol{p}_*)\delta\varepsilon_s(\boldsymbol{p}_s)\right].$$

The second term in square brackets is small with respect to $\mathcal{A}_{\rm CP}$ and can be neglected while the third and fourth terms vanish once integrated over a p_* domain symmetric in η. Hence the observed asymmetry of the D^*–tagged $D^0 \to h^+h^-$ sample is

$$A(hh^*) = \left(\frac{N^{\rm obs}_{D^0} - N^{\rm obs}_{\overline{D}^0}}{N^{\rm obs}_{D^0} + N^{\rm obs}_{\overline{D}^0}}\right)^{hh^*} = \mathcal{A}_{\rm CP}(h^+h^-) + \delta(\pi_s) \tag{3.3}$$

where

$$\delta(\pi_s)^{hh^*} = \int d\boldsymbol{p}_s\ n_s^{hh^*}(\boldsymbol{p}_s)\ \delta\varepsilon_s(\boldsymbol{p}_s)$$

is the instrumental asymmetry for reconstructing a positive or negative soft pion associated with a h^+h^- charm decay, induced by charge–asymmetric interaction cross section and reconstruction efficiency for low transverse momentum pions, and

$$n_s^{hh^*}(\boldsymbol{p}_s) = \frac{\int d\boldsymbol{p}_* d\boldsymbol{p}_{h^+} d\boldsymbol{p}_{h^-} \varrho_*(\boldsymbol{p}_*)\varrho_{hh^*}(\boldsymbol{p}_{h^+}, \boldsymbol{p}_{h^-}, \boldsymbol{p}_s \mid \boldsymbol{p}_*)\varepsilon_{hh}(\boldsymbol{p}_{h^+}, \boldsymbol{p}_{h^-})\varepsilon_s(\boldsymbol{p}_s)}{\int d\boldsymbol{p}_* d\boldsymbol{p}_{h^+} d\boldsymbol{p}_{h^-} d\boldsymbol{p}_s \varrho_*(p_*)\varrho_{hh^*}(\boldsymbol{p}_{h^+}, \boldsymbol{p}_{h^-}, \boldsymbol{p}_s \mid \boldsymbol{p}_*)\varepsilon_{hh}(\boldsymbol{p}_{h^+}, \boldsymbol{p}_{h^-})\varepsilon_s(\boldsymbol{p}_s)}$$

is the observed normalized density in phase space of the soft pion candidates reconstructed in our D^*–tagged $D^0 \to h^+h^-$ decays sample.

In App. A we prove that with a procedure similar to the one just outlined here for the $D^\star$–tagged $D^0 \to h^+h^-$ case, the asymmetries between the observed yields of D^*–tagged and untagged $D^0 \to K^-\pi^+$ and $\overline{D}^0 \to K^+\pi^-$ decays, when neglecting all terms of order $\mathcal{A}_{\rm CP}\delta$, $\mathcal{A}_{\rm CP}\delta^2$ and δ^2, can be written respectively as

$$A(K\pi^*) = \mathcal{A}_{\rm CP}(K^-\pi^+) + \delta(\pi_s)^{K\pi^*} + \delta(K\pi)^{K\pi^*} \quad \text{and} \tag{3.4}$$

$$A(K\pi) = \mathcal{A}_{\rm CP}(K^-\pi^+) + \delta(K\pi)^{K\pi}, \tag{3.5}$$

where

$$\delta(\pi_s)^{K\pi^*} = \int d\boldsymbol{p}_s n_s^{K\pi^*}(\boldsymbol{p}_s)\delta\varepsilon_s(\boldsymbol{p}_s)$$

is the instrumental asymmetry for reconstructing a positive or negative soft pion associated with a $K^\pm\pi^\mp$ charm decay,

$$\delta(K\pi)^{K\pi^*} = \int d\boldsymbol{p}_K d\boldsymbol{p}_\pi \; n_{K\pi}^{K\pi^*}(\boldsymbol{p}_K,\boldsymbol{p}_\pi) \; \delta\varepsilon_{K\pi}(\boldsymbol{p}_K,\boldsymbol{p}_\pi)$$

and

$$\delta(K\pi)^{K\pi} = \int d\boldsymbol{p}_K d\boldsymbol{p}_\pi \; n_{K\pi}^{K\pi}(\boldsymbol{p}_K,\boldsymbol{p}_\pi) \; \delta\varepsilon_{K\pi}(\boldsymbol{p}_K,\boldsymbol{p}_\pi)$$

are the instrumental asymmetries for reconstructing a $K^\pm\pi^\mp$ decay respectively for the tagged and the untagged case; these are expected from the difference in interaction cross–section with matter between positive and negative kaons or pions and charge–curvature asymmetries in track triggering and reconstruction. As for $\delta(\pi_s)^{hh^*}$, all other δ quantities considered here are function of the observed normalized densities in phase space of the final state particles observed in the specific event sample $n_s^{K\pi^*}(\boldsymbol{p}_s)$, $n_{K\pi}^{K\pi^*}(\boldsymbol{p}_K,\boldsymbol{p}_\pi)$ and $n_{K\pi}^{K\pi}(\boldsymbol{p}_K,\boldsymbol{p}_\pi)$ (see App. A).

If the kinematic distributions of soft pions are consistent in $K\pi^*$ and hh^* samples,

$$n_s^{K\pi^*}(\boldsymbol{p}_s) = n_s^{hh^*}(\boldsymbol{p}_s), \tag{3.6}$$

and if the distributions of D^0 decay products are consistent in $K\pi^*$ and $K\pi$ samples,

$$n_{K\pi}^{K\pi^*}(\boldsymbol{p}_K,\boldsymbol{p}_\pi) = n_{K\pi}^{K\pi}(\boldsymbol{p}_K,\boldsymbol{p}_\pi), \tag{3.7}$$

then $\delta(\pi_s)^{hh^*} = \delta(\pi_s)^{K\pi^*}$ and $\delta(K\pi)^{K\pi^*} = \delta(K\pi)^{K\pi}$. The two equalities in Eqs. (3.6) and (3.6) hold with good approximation since the topology of the three

decays of interest is very similar. Nevertheless, as discussed in Sect. 4.4, we explicitly enforce them in our analysis by an appropriate kinematic re–weighing of the event samples.[2] Finally, combining Eq. (3.3) with Eqs. (3.4) and (3.5) under these assumptions, the CP violating asymmetry in the $D^0 \to h^+h^-$ decay become accessible as

$$\mathcal{A}_{\rm CP}(hh) = A(hh^*) - A(K\pi^*) + A(K\pi). \tag{3.8}$$

In summary, the analysis strategy consists in measuring the asymmetries between the observed yields of charm and anticharm decays in three different event samples: D^*–tagged $D^0 \to h^+h^-$ decays, D^*–tagged $D^0 \to K^+\pi^-$ decays and untagged $D^0 \to K^+\pi^-$ decays. Then, using Eq. (3.8), and thanks to the hierarchy of branching ratios between these three sample, we extract the physical $\mathcal{A}_{\rm CP}$ subtracting all detector induced effects with a high degree of confidence that allows to keep the level of systematic uncertanties well below the statistical ones.

It is worth underlining explicitly the base assumptions that make our subtraction procedure possible. First, strong $p\bar{p}$ interactions are charge symmetric, *i. e.* primary D^0 and $\overline{D}^0$ mesons are produced in equal number as are primary D^{*+} and D^{*-} mesons. A small charge asymmetry in D^0 and $\overline{D}^0$ production as a function of η could be caused by charge or flavor correlations between the charmed meson and the beam particles. In $p\bar{p}$ collisions, this asymmetry is constrained, by CP symmetry of the strong interaction, to change sign for opposite η, and thus the net effect cancels out as long as the distribution of the decays in our sample is symmetric in η. Finally, we assume that the detection efficiency for the D^* can be expressed as the product of the efficiency for the soft pion times the efficiency for the D^0 final state.

While the first assumption does not need to be really proven, all the others have been tested directly on data, and any residual effect included in the systematic uncertainties as discussed in Chap. 6. Moreover, before applying this technique to data, we proved that our approach achieves the goal of suppressing detector induced asymmetries down to the permille level using Monte Carlo simulation, as described

[2] We need to equalize distributions with respect to the true momenta while we only access the distributions with respect to the measured momenta. Hence the assumption that event samples that have the same distribution with respect to the measured quantities also have the same distribution with respect to the true quantities is needed.

in the following. The Monte Carlo is used here only to test the effectiveness and robustness of the technique under arbitrary configurations of detector asymmetries. All the numbers entering the determination of the actual measurement are derived from data, with no direct input from simulation, that we do not assume to quantitatively reproduce any of the effects present in our real detector.

3.4 Validation of the analysis technique

The effectiveness of our methodology in the suppression of instrumental effects can be tested by repeating the analysis in simulated samples in which known instrumental and physics asymmetries are introduced. It is not necessary for this test to be meaningful that such simulated instrumental asymmetries exactly reproduce the situation found in real data (which is only approximately known). Conversely, the meaningfulness of the results is enhanced by the ability to test a variety of different simulated configurations, including effects stronger than in real data. Many different configurations for the input asymmetries were tested, covering a rather extended range. For each configuration, $\mathcal{O}(10^6)$ decays were simulated to reach the desired 0.1% sensitivity.

To achieve this goal in a reasonable time we used a resampling technique applied to a smaller set of statistically independent simulated samples. We present a detailed description of the resampling/reweighting algorithm in Sect. 3.4.1, and the results for the validation procedure in the Sect. 3.4.2. Only the $D^0 \to \pi^+\pi^-$ sample was tested as it is fully representative for the $D^0 \to K^+K^-$ case as well.

3.4.1 Reweighting algorithm for introduction of artificial asymmetries

We generated two indipendent Monte Carlo samples, with full detector simulation (see App. B for additional details), each consisting of about 250 000 decays: one of $D^{*+} \to D^0(\to \pi^-\pi^+)\pi_s^+$ decays, used to reconstruct the tagged $\pi\pi$ sample, and another of $D^{*+} \to D^0(\to K^-\pi^+)\pi_s^+$ decays, used to reconstruct both the tagged and the untagged $K\pi$ decays. For each of these three samples ('parent samples') we construct several samples (of equal or bigger size) by random sampling with replacement from the original dataset (bootstrapping). This provides several different

high–statistics samples, nearly statistically independent, with features similar to the initial parent sample, but saves us the huge computational load required to fully simulate through the CDF detector model many independent samples, each made of millions of events. On top of these resampled datasets different arbitrary input asymmetries are introduced and controlled by an event–specific weight applied to the generator–level information.

The resampling/reweighting algorithm is based on individual event weights. For each event of the parent Monte Carlo sample we extract a non–negative integer "weight", w, representing the number of times the event will be repeated in the final resampled/reweighted dataset. The value of the weight depends on the chosen input values for the asymmetries, which can depend on the features of the event itself. The input quantities of the algorithm are:

- the resampling factor, N, a positive integer that correspond to the mean multiplication factor of the parent sample size;
- the reconstruction efficiency ratio of positive and negative pions, $\varepsilon(\pi^+)/\varepsilon(\pi^-)$, an arbitrary parameter used to mimic instrumental asymmetries in pion reconstruction. This can be function of an arbitrary number of variables, like pion momenta, azimuthal angle, etc...;
- the reconstruction efficiency ratio of positive and negative kaons, $\varepsilon(K^+)/\varepsilon(K^-)$, analogous to above;
- the physical CP violating asymmetry $\mathcal{A}_{\rm CP}(K^-\pi^+)$;
- the physical CP violating asymmetry $\mathcal{A}_{\rm CP}(\pi^+\pi^-)$.

The algorithm for each event proceeds as follows.

We extract from a Poisson distribution with mean N the number of times n that this particular event is going to be picked up in the resampling procedure, so the value of w is initialized to n. For each of the n repetitions generator–level information is used to keep or drop the sampled event according to the desired values of relative efficiencies and physical asymmetries. As an example, to account for a certain $r = \varepsilon(\pi^+)/\varepsilon(\pi^-)$ value, say less than one, we look for a positive pion in the list of generated particles, and for each pion found in the event we extract from a uniform distributed probability a value p; if $p \geqslant r$ we reject the event, *i. e.* we

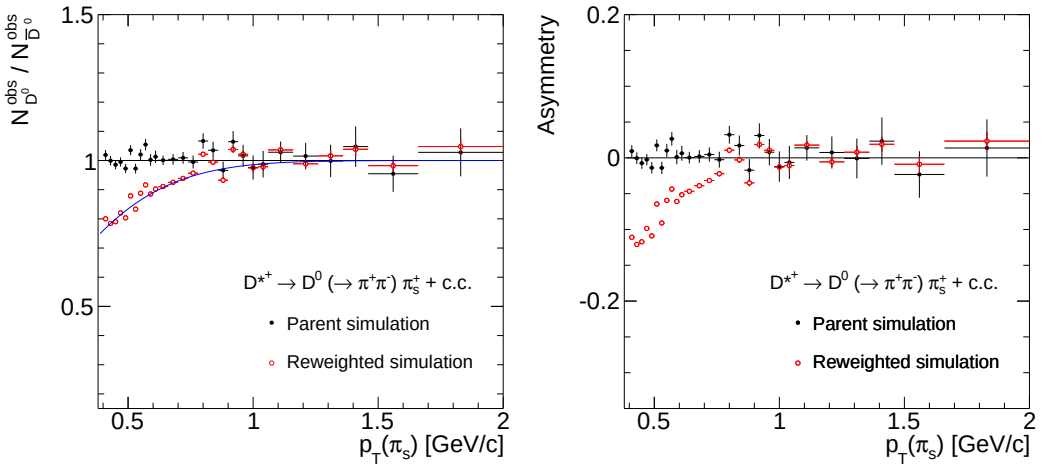

(a) (b)

Figure 3.2: *Ratio (a) and asymmetry (b) between simulated* $D^{*+} \to D^0(\to \pi^+\pi^-)\pi^+_s$ *and* $D^{*-} \to \overline{D}^0(\to \pi^+\pi^-)\pi^-_s$ *decays as a function of transverse momentum for the original ('parent') simulated sample (closed black points) and for a resampled dataset (open red points) of a factor 10 using the efficiency ratio represented by the blue curve is introduced.*

decrease the current weight w of one unit. A similar procedure is applied for all other input quantities. The same algorithm is applied to all three samples ($\pi\pi^\star$, $K\pi^\star$ and $K\pi$). Since we reconstruct also the untagged $D^0 \to K^-\pi^+$ decays from simulated $D^\star$ decays, in this case we ignore the pion from the $D^\star \to D^0\pi$ decay in the list of generated particles when calculating the final weight.

Fig. 3.2 (a) shows, as an example, how the ratio of positive and negative soft pions as a function of the track transverse momentum changes after applying our algorithm: black points are the parent sample of $D^{*+} \to D^0(\to \pi^+\pi^-)\pi^+_s$ decays, in which the ratio is constantly equal to 1 in all the p_T range, while red points are a dataset resampled by a factor 10 after applying a reweight that uses as input the reconstruction efficiency ratio

$$\frac{\varepsilon(\pi^+)}{\varepsilon(\pi^-)} = \mathrm{Erf}\left(\frac{3}{2}\, p_T + A\right) \tag{3.9}$$

with $A = 0.23$ and represented by the blue curve.

An initial test of the procedure, which also helps in detailing all the steps of the procedure itself, is performed using the following six different configurations:

(0) resampling $\times 10$ (this is used to check that the resampling procedure itself does not introduce additional biases);

(1) resampling $\times 10$ and p_T–dependent $\varepsilon(\pi^+)/\varepsilon(\pi^-)$ given by the expression in Eq. (3.9);

(2) resampling $\times 10$ and $\varepsilon(K^+)/\varepsilon(K^-) = 98\%$ constant;

(3) resampling $\times 10$ and $\mathcal{A}_{\rm CP}(\pi^+\pi^-) = 1.1\%$;

(4) resampling $\times 10$ and $\mathcal{A}_{\rm CP}(K^-\pi^+) = 0.8\%$;

(5) all of the above.

We reweight the $\pi\pi^\star$, $K\pi^\star$ and $K\pi$ samples according to each of these cases and for each we measure the observed asymmetries: $A(\pi\pi^\star)$, $A(K\pi^\star)$, $A(K\pi)$; then, using Eq. (3.8), we extract $\mathcal{A}_{\rm CP}(\pi^+\pi^-)$ and verify that it is consistent with the known input value.

It must be noted that owing to the finite size of the parent sample, small initial asymmetries due to statistical fluctuations are present there. These small asymmetries are unaffected by the resampling procedure, and propagate to all of our resampled dataset. The result obtained in each configuration defined above are therefore subtracted from the $\mathcal{A}_{\rm CP}(\pi^+\pi^-)$ value of the parent dataset.

Tab. 3.1 reports, as an example, the results from each single test for the original dataset (the unweighted case) and the six different resampling/reweighting cases. In the last columns there are three different $\mathcal{A}_{\rm CP}(\pi^+\pi^-)$ values: the absolute one is obtained using Eq. (3.8), while the second is the $\mathcal{A}_{\rm CP}(\pi^+\pi^-)$ value after subtracting the one obtained on the original unweighted sample, this is the one that should be compared with the input $\mathcal{A}_{\rm CP}(\pi^+\pi^-)$ value.

The resulting $\mathcal{A}_{\rm CP}(\pi^+\pi^-)$ from a single test is always in good agreement with the expectation from the parent sample. This test has been repeated 100 times. Fig. 3.3 shows the distributions of the bias,

$$\Delta\mathcal{A}_{\rm CP}(\pi^+\pi^-) = \mathcal{A}_{\rm CP}(\pi^+\pi^-) - \mathcal{A}_{\rm CP}(\text{unweighted}) - \mathcal{A}_{\rm CP}(\text{input}), \tag{3.10}$$

case by case; the distributions have mean value compatible with zero and r.m.s. width of about 0.08% as expected.

Reweighting configuration	$A(\pi\pi^\star)$ (%)	$A(K\pi^\star)$ (%)	$A(K\pi)$ (%)	$\mathcal{A}_{\rm CP}(\pi^+\pi^-)$ (%)		
				absolute	wrt unw. case	input value
Unweighted	-0.32 ± 0.15	$+0.37 \pm 0.16$	$+0.34 \pm 0.15$	-0.36 ± 0.27	-	-
0	-0.36 ± 0.05	$+0.38 \pm 0.05$	$+0.32 \pm 0.05$	-0.41 ± 0.08	-0.05 ± 0.08	0.00
1	$+4.22 \pm 0.05$	$+4.91 \pm 0.05$	$+0.32 \pm 0.05$	-0.37 ± 0.09	-0.01 ± 0.09	0.00
2	-0.36 ± 0.05	-0.62 ± 0.05	-0.70 ± 0.05	-0.43 ± 0.08	-0.07 ± 0.08	0.00
3	$+0.82 \pm 0.05$	$+0.38 \pm 0.05$	$+0.32 \pm 0.05$	$+0.76 \pm 0.08$	$+1.20 \pm 0.08$	1.10
4	-0.36 ± 0.05	$+1.10 \pm 0.05$	$+1.14 \pm 0.05$	-0.32 ± 0.08	-0.04 ± 0.08	0.00
5	$+5.34 \pm 0.05$	$+4.73 \pm 0.05$	$+0.13 \pm 0.05$	$+0.73 \pm 0.09$	$+1.09 \pm 0.09$	1.10

Table 3.1: *Results of the measurement applied to simulated samples for the different configurations specified in the text.*

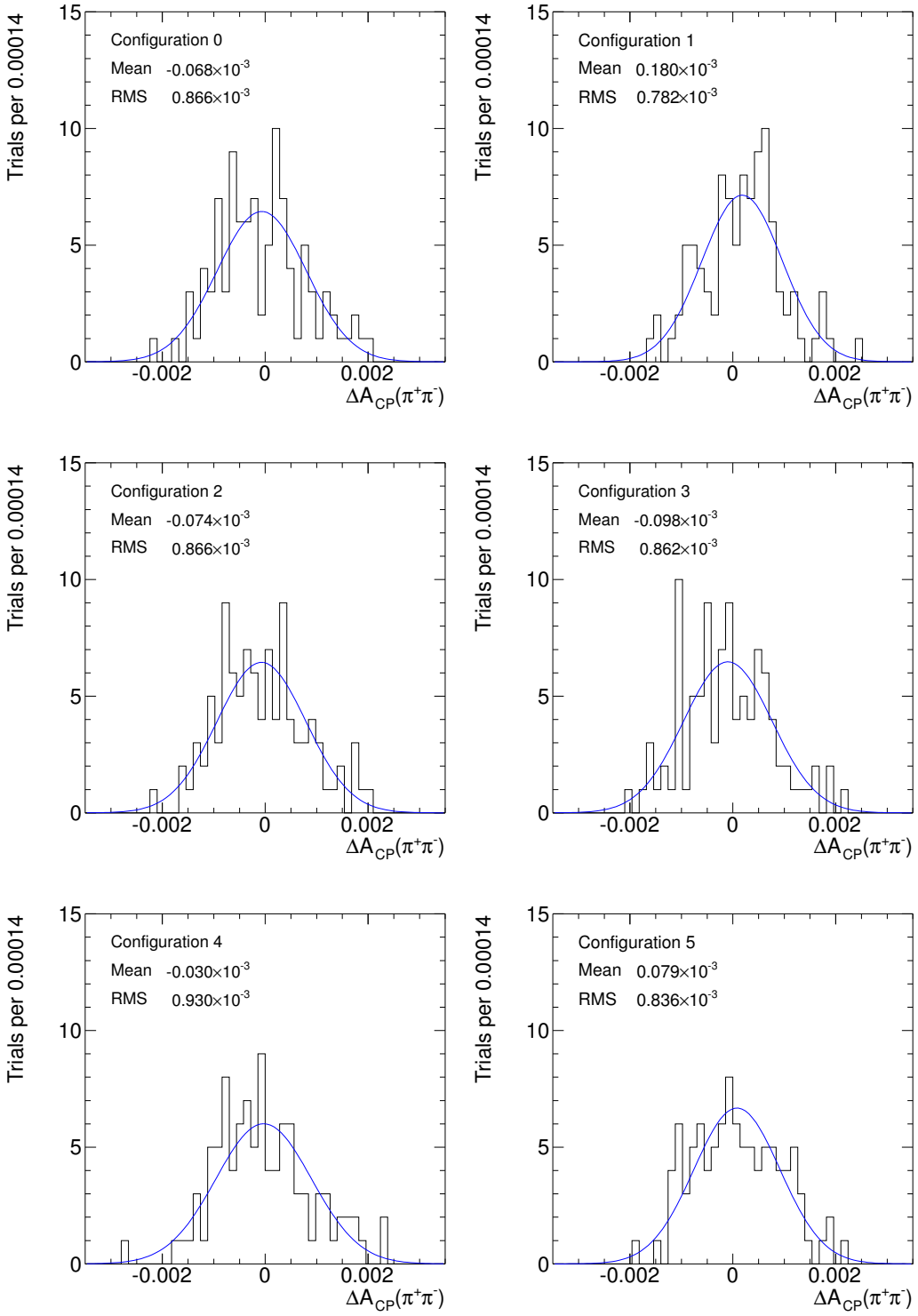

Figure 3.3: *Distributions of the asymmetry bias for the different reweighting configurations specified in the text.*

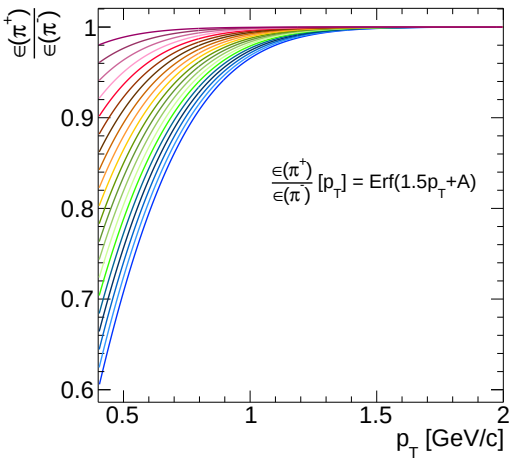

Figure 3.4: *Curves corresponding to the set of simulated ratios of efficiencies, used in our study, for reconstructing positive versus negative pions as a function of transverse momentum.*

3.4.2 Validation results

We performed our validation procedure on ensembles of simulated decays, weighted with the algoritm described above, each consisting of approximately one thousand trials. We compare the resulting asymmetry measured by our analysis method, $\mathcal{A}_{\rm CP}(\pi^+\pi^-)$, to the one given in input, by inspecting the mean value of the distribution of the residual, $\Delta\mathcal{A}_{\rm CP}(\pi^+\pi^-)$ given in Eq. (3.10), as a function of all the input parameters of the reweighting algorithm.

We first investigate the individual impact of each effect. We scan the value of a single input parameter across a range that covers larger variations than expected in data and assume all other effects are zero. First a p_T–dependent function that represents the dependence observed in data is used to parameterize the soft pion reconstruction efficiency ratio as $\varepsilon(\pi^+)/\varepsilon(\pi^-) = \mathrm{Erf}\,(1.5 \cdot p_T + A)$, where p_T is in GeV/c and various values of the constant A have been tested so that the efficiency ratio at 400 MeV/c spans the $[0.6, 1]$ range as shown in Fig. 3.4. Then, the kaon reconstruction efficiency ratio $\varepsilon(K^-)/\varepsilon(K^+)$ is varied in the $[0.6, 1]$ range. Finally, a range $-10\% < \mathcal{A}_{\rm CP} < 10\%$ is tested for the physical CP–violating asymmetry in $D^0 \to K^-\pi^+$ and $D^0 \to \pi^+\pi^-$ decays.

The results are shown in Fig. 3.5. Cancellation of instrumental asymmetries is

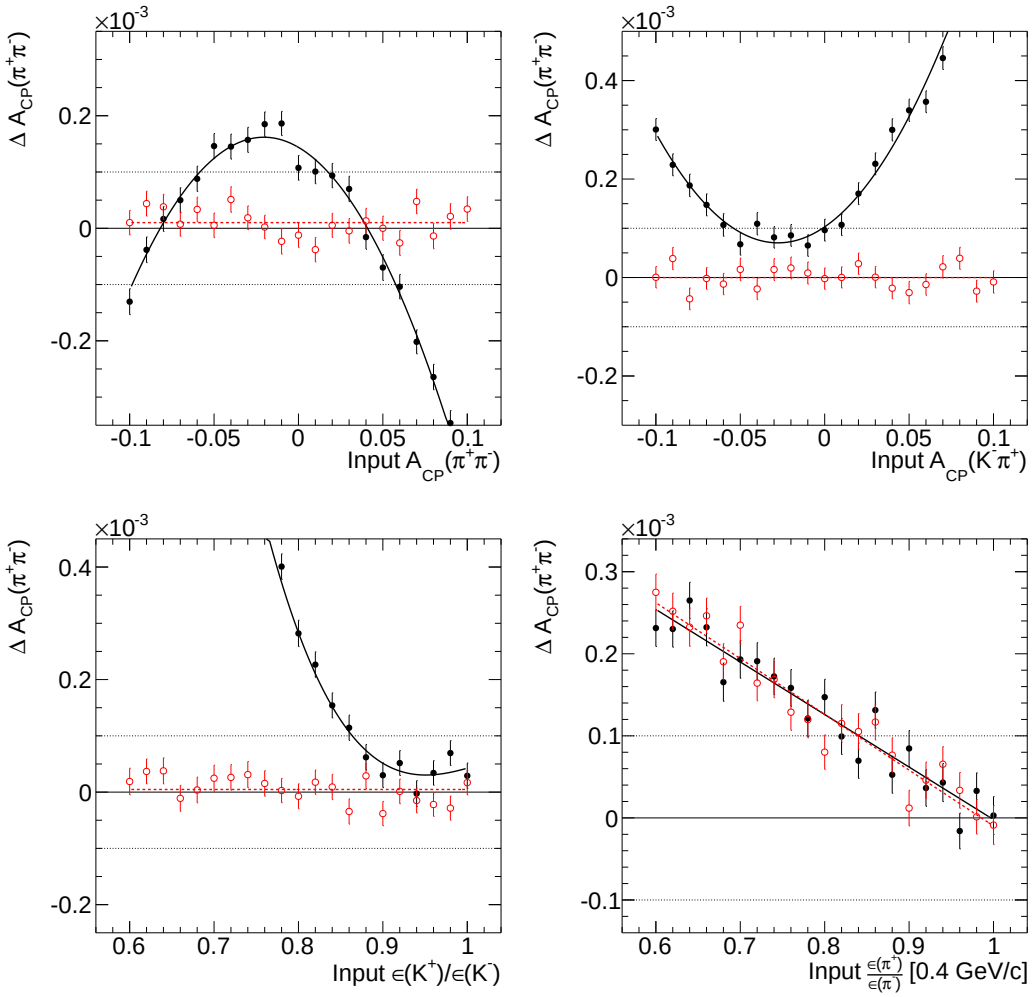

Figure 3.5: *Asymmetry residual as a function of the input quantity varied. Other effects are assumed zero (open red points) or different from zero (closed black points).*

achieved at the sub–permille level even with input effects of size much larger than estimated in data. Fig. 3.5 also shows the results of a more complete test in which other effects are simulated, in addition to the quantities varied in the single input parameter scan: a p_T–dependent relative efficiency $\varepsilon(\pi^+)/\varepsilon(\pi^-)$, corresponding to 80% at 400 MeV/c, $\varepsilon(K^-)/\varepsilon(K^+) = 98\%$, $\mathcal{A}_{\rm CP}(K^-\pi^+) = 0.8\%$ and $\mathcal{A}_{\rm CP}(\pi^+\pi^-) = 1.1\%$. Larger variations of the residual are observed with respect to the previous case. This is expected as a consequence of nonlinear interaction of effects in higher–order terms, that are not completely cancelled by our procedure.

Finally we tested our analysis procedure using realistic values for the detector effects. The p_T dependence of $\varepsilon(\pi^+)/\varepsilon(\pi^-)$ is determined, from a fit to the

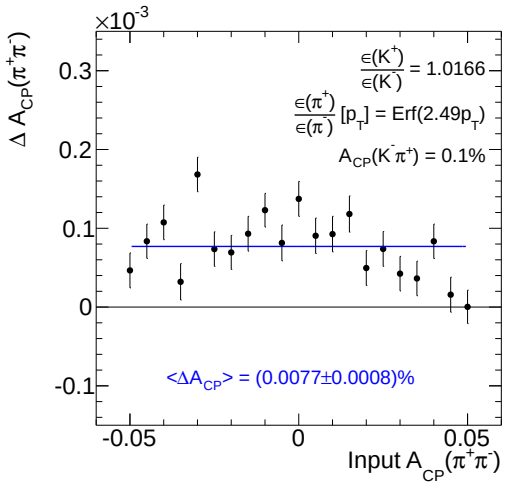

Figure 3.6: *Asymmetry residual as a function of the physical CP–violating asymmetry in $D^0 \to \pi^+\pi^-$ decays. Realistically sized effects other than shown in the scan are also simulated. The line represents the average over the $-5\% < \mathcal{A}_{CP}(\pi^+\pi^-) < 5\%$ range.*

data (Fig. 3.1), to be distributed as $\mathrm{Erf}\,(2.49\ p_T)$, with p_T in GeV/c. We use $\varepsilon(K^+)/\varepsilon(K^-)$ approximately equal to $\varepsilon(K^+\pi^-)/\varepsilon(K^-\pi^+) = 1.0166$ [73], *i. e.* we assume equal efficiency for reconstructing positive and negative pions at $p_T > 2\,\mathrm{GeV}/c$. We assume $\mathcal{A}_{\mathrm{CP}}(K^-\pi^+) = 0.1\%$, ten times larger than the current experimental sensitivity. A $-5\% < \mathcal{A}_{\mathrm{CP}}(\pi^+\pi^-) < 5\%$ range is tested in steps of 0.5% for the physical asymmetry to be measured.

The results are shown in Fig. 3.6. The maximum observed bias is of the order of 0.02%, one order of magnitude smaller than the statistical resolution on the present measurement. The observed residual bias is $(0.0077 \pm 0.0008)\%$ averaged over the $\mathcal{A}_{\mathrm{CP}}(\pi^+\pi^-)$ range probed. These results demonstrate the reliability of our method in extracting a precise and unbiased measurement of CP violation in D^0 meson decays into K^+K^- and $\pi^+\pi^-$ final states, even in the presence of sizable unknown instrumental asymmetries.

Chapter 4

Event Selection

This chapter describes the reconstruction and selection of the samples of charm decays used in this measurement starting from the events collected by the CDF II displaced–track trigger.

4.1 Data sample

The analysis uses the data collected between February 2002 and January 2010 by the trigger on displaced tracks, whose on–line selection requirements are described in Sect. 2.2.3 and summarized in Tab. 2.1. After the application of the standard CDF data–quality requirements (see Sect. 2.2.4), the sample size corresponds to an integrated luminosity of about $5.9\,\mathrm{fb}^{-1}$. In the following we outline the reconstruction of off–line $D^0 \to h^+h^{(\prime)-}$ candidates and we describe the specific selection of the four samples (D^*–tagged $D^0 \to \pi^+\pi^-$, $D^0 \to K^+K^-$, $D^0 \to K^-\pi^+$ and untagged $D^0 \to K^-\pi^+$) used in the analysis. In Sect. 4.4 we also describe how the different samples are candidate–by–candidate weighted in order to equalize their kinematic distributions as needed by our procedure of detector asymmetries subtraction.

4.2 Reconstruction of $D^0 \to h^+h^{(\prime)-}$ candidates

The off–line selection is designed with the aim of retaining the largest possible number of $D^0 \to h^+h^{(\prime)-}$ decays collected at trigger level with accurately measured momenta and decay vertices and avoiding any requirements that may induce asymmetries between the number of selected D^0 and $\overline{D}^0$ mesons. The reconstruction is based solely on tracking, disregarding any information on particle identification.

The default tracking algorithm, as described in Sect. 2.2.2, disregards the effect of multiple scattering in the COT. According to a standard CDF procedure,

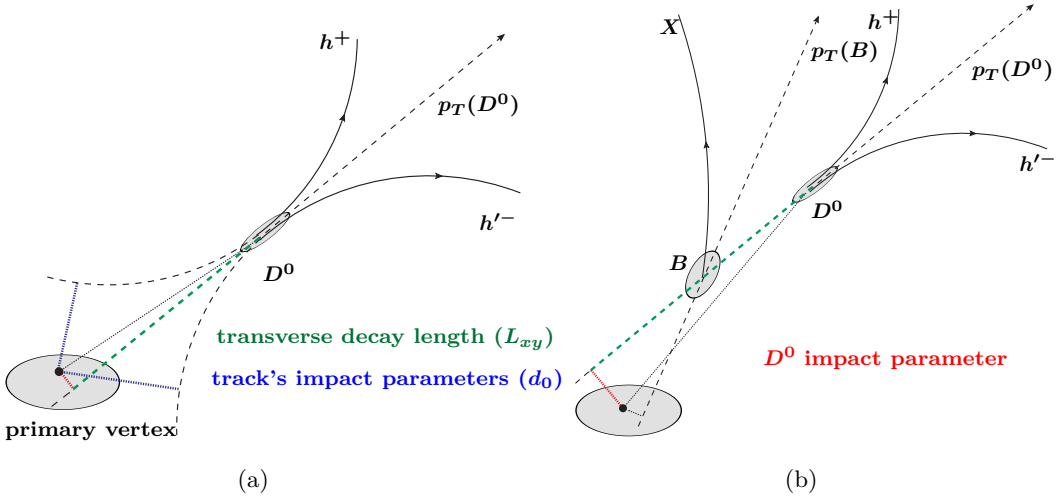

Figure 4.1: *Schematic representation, in the plane transverse to the beam, of the topologies of prompt (a) and secondary (b)* $D^0 \to h^+h'^-$ *decays. Dimensions are not in scale.*

we compensate for this approximation by refitting the tracks, after rescaling the covariance matrix of the COT track with an appropriate set of scale factors which have been determined on data. The rescaled COT track is used to seed the refit of the combined COT–SVX II tracks. The refitting uses an algorithm based on the Kalman filtering [74] and includes energy–loss corrections for kaons, pions and protons, according to the chosen mass assignment for each particle. This procedure has been carefully studied and validated by independent analyses when performing calibrations for the precision measurements of b–hadron masses [75].

Standard quality criteria on the minimum number of associated silicon and drift chamber hits are applied to each track to ensure precisely measured momenta and decay vertices in three–dimensions. In addition, both tracks are required to have $p_T > 2.2\,\mathrm{GeV}/c$, $|\eta| < 1$, and impact parameter between 0.1 and 1 mm.

The reconstruction of D^0 candidates considers all pairs of oppositely charged tracks selected with this criteria. Moreover, only track pairs compatible with having fired the trigger are used. Since SVT tracks are reconstructed with a different fitting algorithm with respect to the off–line tracks, the sample selected by the off–line analysis may contain candidates which did not satisfy the trigger selection ("volunteers"). The presence of volunteers may alter the kinematic distributions of our samples and could potentially introduce unwanted biases in the measurement

Tracks	Units	Requirement
Axial silicon hits	–	≥ 3
90° silicon hits	–	≥ 2
Small angle stereo silicon hits	–	≥ 1
Axial COT SL hits	–	≥ 10
Stereo COT SL hits	–	≥ 10
Total COT hits	–	≥ 40
p_T	GeV/c	> 2.2
$\lvert\eta\rvert$	–	< 1.0
Impact parameter	μm	[100, 1000]
D^0 candidate	Units	Requirement
Product of track's charges	e^2	-1
Transverse decay length	μm	> 200
Scalar sum of track's p_T	GeV/c	> 4.5
Impact parameter	μm	< 100
χ^2 of the vertex fit	–	< 30
χ^2_{xy} of the vertex fit	–	< 15
$\lvert\eta\rvert$	–	< 1
Track's azimuthal separation	degrees	[2, 90]
$m_{\pi^+\pi^-}$	GeV/c^2	[1.2, 2.4]

Table 4.1: *Summary of the selection requirements for* $D^0 \to h^+h^{(\prime)-}$ *decays.*

by partially invalidating the subtraction of detector effects when comparing the asymmetries measured in the three $D^0 \to h^+h^{(\prime)-}$ samples of interest. Thus we excluded them by requiring a close match[1] between the off–line track pair forming the $D^0 \to h^+h^{(\prime)-}$ candidate and two SVT tracks in each event; then the complete set of trigger requirements was applied to the SVT quantities of the matched tracks, thus repeating the real trigger decision in the off–line analysis.

The two tracks are constrained to originate from a common vertex by a kinematic fit subject to standard quality requirements. We then arbitrarily assigned the charged pion mass to both tracks and ask the $\pi^+\pi^-$ mass of candidates to be in the

[1]The algorithm required proximity in curvature and azimuthal opening angle between SVT tracks and off–line tracks.

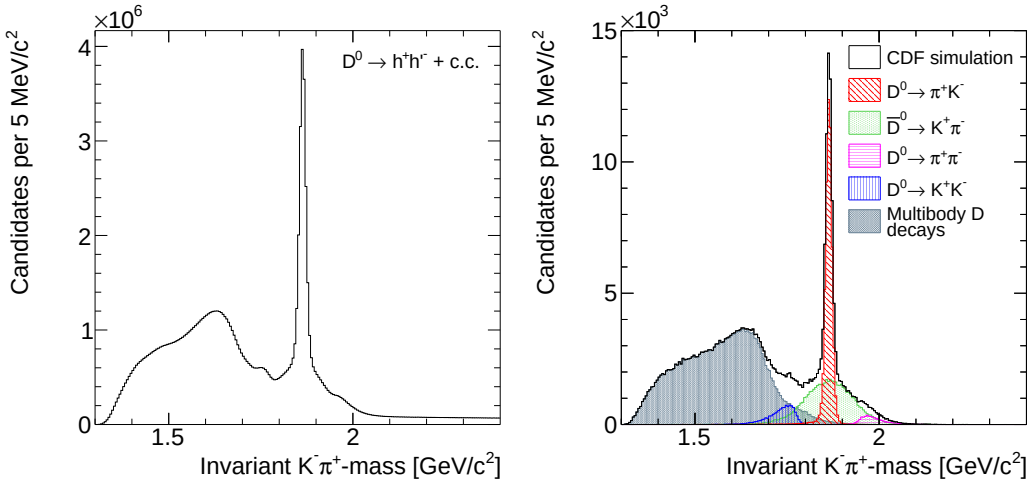

(a) (b)

Figure 4.2: *Comparison between the $K^-\pi^+$ mass distributions of the untagged sample (a) and of a simulated sample of inclusive charm decays (b).*

range $[1.2, 2.4]\,\mathrm{GeV}/c^2$, to retain all signals of interest and sideband regions sufficiently wide to study backgrounds. The decay topology is graphically represented in Fig. 4.1 (a). The two tracks are required to have a scalar sum of transverse momenta greater than $4.5\,\mathrm{GeV}/c$ and have an azimuthal separation $2^\circ < \Delta\phi < 90^\circ$ to remove pairs of quasi–collinear tracks which can occur in hadronic jets due to light–quark fragmentation, or in highly occupied regions of the detector due to combinations of fake tracks, and pairs of azimuthally–opposed tracks coming from back–to–back jets of generic QCD background. We require L_{xy} to exceed $200\,\mu$m to reduce background from decays of hadrons that do not contain heavy quarks. We also require the impact parameter of the D^0 candidate with respect to the beam to be smaller than $100\,\mu$m to remove most of the charmed mesons produced in weak decays of bottom–flavored hadrons (secondary charm, see Fig. 4.1 (b)).

The complete list of all off–line requirements applied to select the $D^0 \to h^+h^{(\prime)-}$ decays are summarized in Tab. 4.1. In the rare (0.04%) occurrence that multiple $D^0 \to h^+h^{(\prime)-}$ decays sharing the same tracks are reconstructed in the event, we retain the one having the best vertex fit quality.

Fig. 4.2 shows the $K^-\pi^+$ mass distribution for the resulting sample, which is referred to as "untagged" in the following since no D^* decay reconstruction has

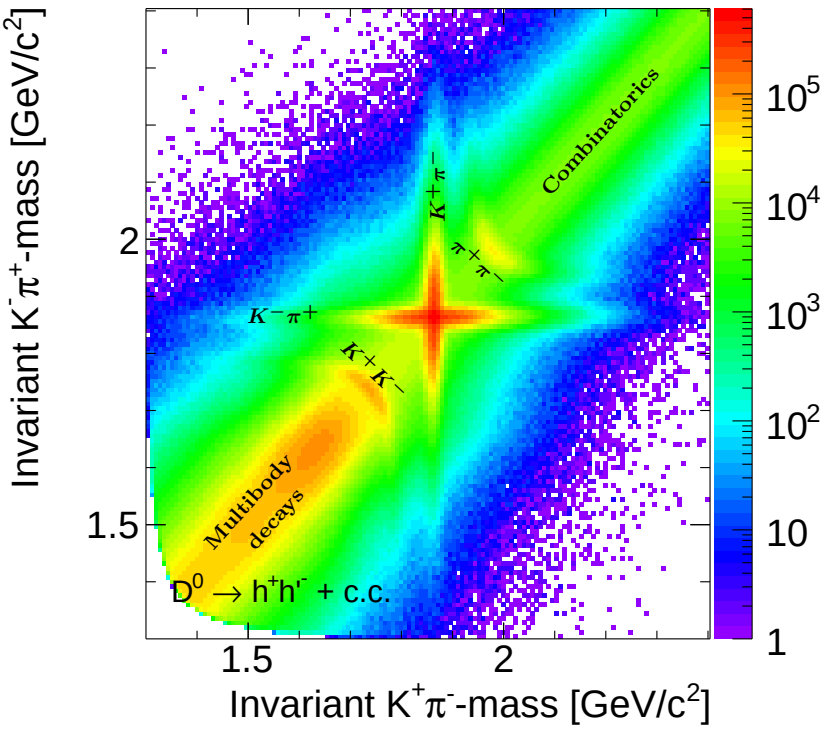

Figure 4.3: *Distribution of* $K^-\pi^+$ *mass as a function of* $K^+\pi^-$ *mass for the untagged sample. Logarithmic scale on* z *axis.*

been imposed at this stage. The distribution of a sample of simulated inclusive charmed decays is also shown for comparison. Only a single charmed meson decay per event is simulated without the underlying event. The prominent narrow signal, about $8\,\mathrm{MeV}/c^2$ wide, is dominated by $D^0 \to K^-\pi^+$ decays (whose branching–ratio is $\mathcal{B} \approx 3.8\%$). A broader structure, also centered on the known D^0 mass, are $\overline{D}^0 \to K^+\pi^-$ candidates reconstructed with swapped K and π mass assignments to the outgoing particles. Approximately 29 million D^0 and $\overline{D}^0$ mesons decaying into $K^\pm\pi^\mp$ final states are reconstructed. The two smaller enhancements at lower and higher masses than the D^0 signal are due to mis–reconstructed $D^0 \to K^+K^-$ ($\mathcal{B} \approx 0.38\%$) and $D^0 \to \pi^+\pi^-$ ($\mathcal{B} \approx 0.14\%$) decays, respectively. Two sources of background contribute. A component of random track pairs that accidentally meets the selection requirements (combinatorial background) is most visible at masses higher than $2\,\mathrm{GeV}/c^2$, but populates almost uniformly the whole mass range. A large shoulder due to mis–reconstructed multibody charm decays peaks at a mass

of approximately $1.6\,\mathrm{GeV}/c^2$. Simulation studies show that this is mainly composed of $D^0 \to K^-\pi^+\pi^0$ decays ($\mathcal{B} \approx 14\%$) in which the neutral pion is not reconstructed but contains also a contamination from $D^+ \to K^-2\pi^+$ decays ($\mathcal{B} \approx 9.5\%$), where the softer of the two charged pions is not reconstructed, $D^0 \to K^-\ell^+\nu_\ell$ decays ($\mathcal{B} \approx 6.7\%$), where the lepton is mis–reconstructed as a pion and the neutrino is not detected, and other much more suppressed three or four–body cham decays.

The sample composition is even more clearly detailed when plotting the $K^-\pi^+$ mass versus the $K^+\pi^-$ mass as in Fig. 4.3. Here the cross–shaped region corresponds to the $K^+\pi^-$ (vertical arm) and $K^-\pi^+$ (orizzontal arm) final state, while the hyperbolic regions at lower (higher) mass values are K^+K^- ($\pi^+\pi^-$) decays.

4.3 Reconstruction of $D^{*+} \to D^0(\to h^+h^{(\prime)-})\pi_s^+$ candidates

In the "tagged" samples reconstruction, we form $D^{*+} \to D^0\pi_s^+$ candidates by associating with each D^0 candidate all tracks present in the same event. The additional particle is required to satisfy basic quality requirements for the numbers of associated silicon and drift chamber hits, to be central ($|\eta| < 1$) and to have transverse momentum greater that $400\,\mathrm{MeV}/c$. We assume this particle to be a pion ("soft pion") and we match its trajectory to the D^0 vertex with simple requirements on relative separation: impact parameter smaller than $600\,\mu$m and longitudinal distance from the primary vertex smaller than 1.5 cm. Since the impact parameter of the low–energy pion has degraded resolution with respect to those of the D^0 tracks, no real benefit is provided by a full three–track vertex fit for the D^* candidate. We retain D^* candidates with $D^0\pi_s$ mass smaller than $2.02\,\mathrm{GeV}/c^2$.

The $D^0\pi_s$ mass is calculated using the vector sum of the momenta of the three particles as D^* momentum, and the known D^0 mass in the determination of the D^* energy. This quantity has the same resolution advantages of the more customary $\Delta m_{h^+h^{(\prime)-}} = m_{h^+h^{(\prime)-}\pi_s^+} - m_{h^+h^{(\prime)-}} - m_{\pi^+}$ mass difference, where m_{π^+} is the known charged pion mass, used by both B–factories and previous CDF analyses and has the additional advantage that it is independent of the mass assigned to the D^0 decay products, which is a useful feature in a precision analysis like ours, where even small effects may be a reason of concern. Therefore all $D^{*+} \to D^0(\to h^+h^{(\prime)-})\pi_s^+$

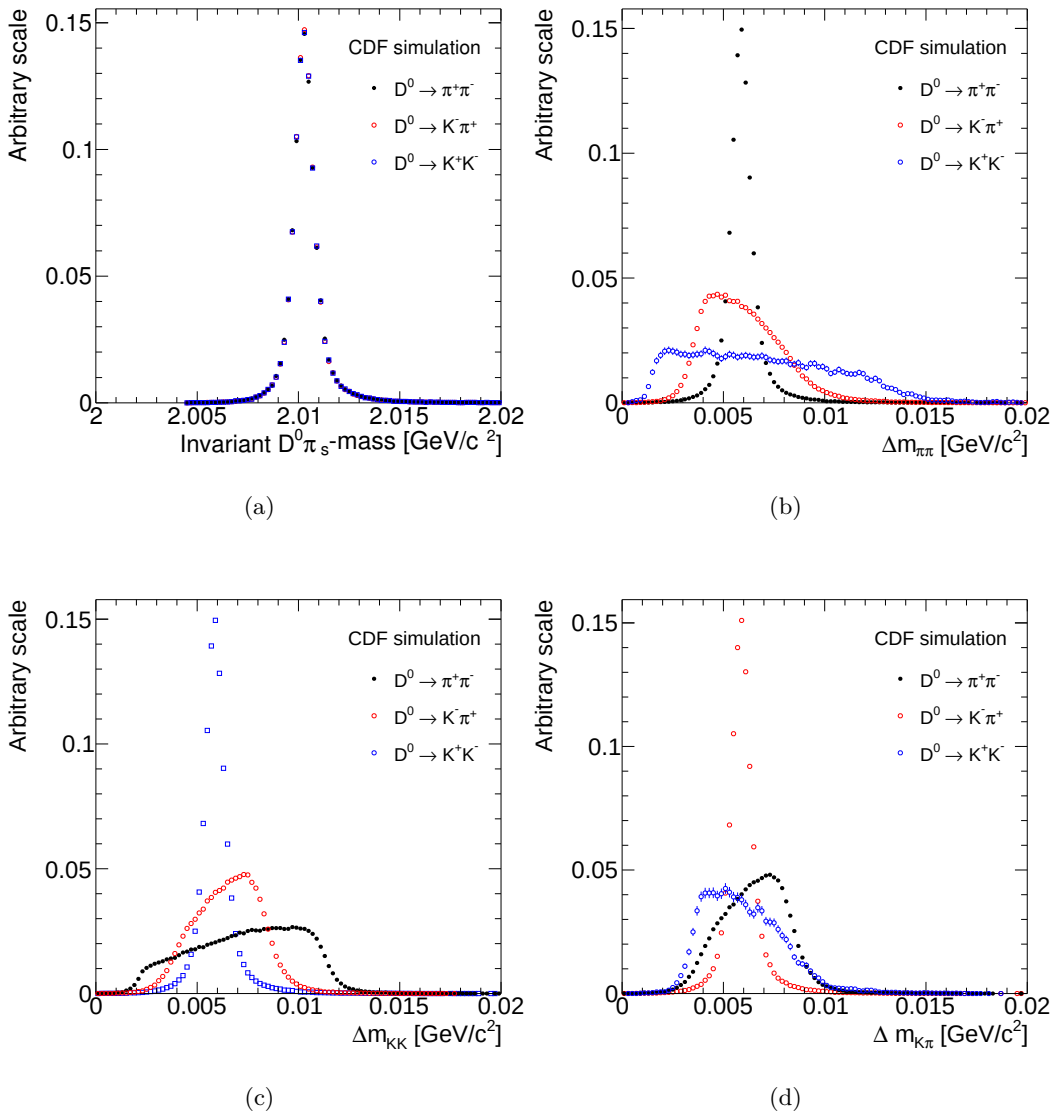

Figure 4.4: *Comparison between the* $D^0\pi_s$ *mass (a) and* $\Delta m_{h^+h^{(\prime)-}}$ *(b)–(d) distributions of a simulated sample of* $D^{*+} \to D^0\pi_s^+$ *with the* $D^0 \to \pi^+\pi^-$ *(red empty points),* $D^0 \to K^-K^+$ *(blue empty square) and* $D^0 \to K^-\pi^+$ *(black filled points). In both variables the mass resolution is about* $0.8\,\mathrm{MeV}/c^2$ *but only in the former distribution the* $D^0 \to h^+h^{(\prime)-}$ *modes have exactly the same shape.*

Soft pion for D^* candidates	Units	Requirement
Silicon hits	–	≥ 1
COT hits	–	≥ 30
p_T	MeV/c	> 400
$\|\eta\|$	–	< 1
Impact parameter	μm	< 600
$\|z_0\|$ from primary vertex	cm	< 1.5
$m_{D^0\pi_s}$	GeV/c^2	< 2.02

Table 4.2: *Summary of the selection cuts for the low momentum tracks that form the $D^* \to D^0\pi$ candidates. Variables names are defined in the text.*

modes, since fully reconstructed, have the same $D^0\pi_s$ mass distribution. Fig. 4.4 shows, the comparison between $m_{D^0\pi_s}$ and $\Delta m_{h^+h^{(\prime)-}}$ distributions of simulated $D^{*+} \to D^0(\to h^+h^{(\prime)-})\pi_s^+$ decays.

Tab. 4.2 summarizes all requirements applied in reconstructing the $D^* \to D^0\pi_s$ decays of our sample. In the 2% of the cases in which multiple D^* candidates are associated with a single D^0 candidate, we randomly choose only one D^* candidate for further analysis.

In each tagged sample ($D^0 \to \pi^+\pi^-$, $D^0 \to K^+K^-$ and $D^0 \to K^-\pi^+$) we require the corresponding two–body mass to lie within 24 MeV/c^2 of the nominal D^0 mass, as shown in Figs. 4.5 (a)–(c). Figs. 4.5 (d)–(f) show the resulting $D^0\pi_s$ mass distribution. A clean D^* signal is visible superimposed on background components that are different in each D^0 channel. In $D^0 \to \pi^+\pi^-$ and $D^0 \to K^-\pi^+$ decays, the background is mainly due to random pions associated with a real D^0 candidate. In the $D^0 \to K^+K^-$ case, there is also a substantial contribution from mis–reconstructed multibody charged and neutral charmed decays that yields a broader enhancement underneath the signal peak. The distribution of the latter component is easily identified when comparing the data distributions of Figs. 4.5 (b) and (e) with Figs. 4.6 (b) and (e), respectively, where the corresponding simulated distributions are plotted. We reconstruct approximately 215 000 D^*–tagged $D^0 \to \pi^+\pi^-$ decays, 476 000 D^*–tagged $D^0 \to K^+K^-$ decays and 5 million D^*–tagged $D^0 \to \pi^+K^-$ decays.

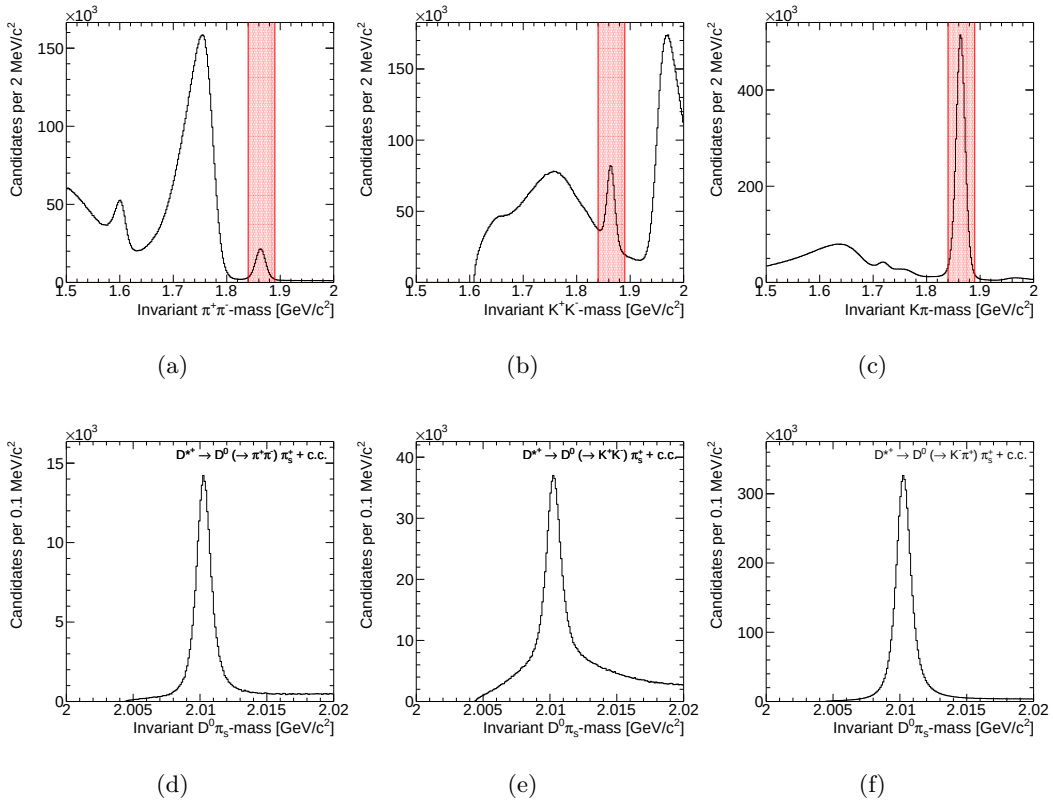

Figure 4.5: *Distributions of $\pi^+\pi^-$ (a), K^+K^- (b) and $K\pi$ (c) mass. Regions used to define the tagged samples are shaded. Distribution of $D^0\pi_s$ mass for tagged $D^0 \to \pi^+\pi^-$ (d), $D^0 \to K^+K^-$ (e) and $D^0 \to K^-\pi^+$ (f) samples selected in the shaded regions.*

4.4 Kinematics equalization

Because detector–induced asymmetries depend on kinematics, the asymmetry cancellation is realized accurately only if the kinematic distributions across the three samples are the same. Although the samples have been selected using the same requirements, small kinematic differences between decay channels may persist due to the different masses involved. We extensively searched for any such residual effect across several kinematic distributions and reweighted the tagged $D^0 \to h^+h^-$ and untagged $D^0 \to K^-\pi^+$ distributions to reproduce the tagged $D^0 \to K^-\pi^+$ ones when necessary. For each channel, identical reweighting functions were used for charm and anticharm decays.

Sideband regions were defined according to the specific features of each tagged

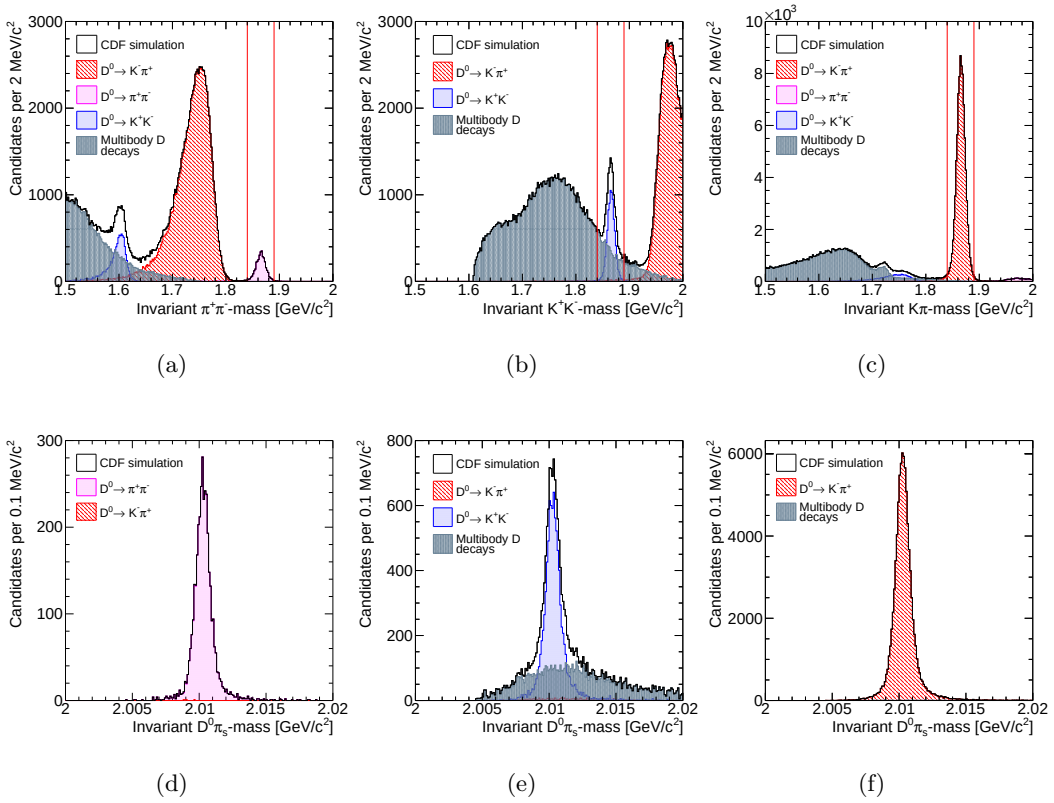

Figure 4.6: *Distributions of $\pi^+\pi^-$ (a), K^+K^- (b) and $K\pi$ (c) mass for a simulated sample of inclusive charm decays. Regions used to define the tagged samples are indicated by two vertical lines. Distribution of $D^0\pi_s$ mass for tagged $D^0 \to \pi^+\pi^-$ (d), $D^0 \to K^+K^-$ (e) and $D^0 \to K^-\pi^+$ (f) simulated samples selected in the regions delimited by the vertical lines.*

sample. For the $K\pi^*$ and $\pi\pi^*$ samples we use as sideband the region at higher $m_{D^0\pi_s}$ values ($[2.015, 2.020]\,\mathrm{GeV}/c^2$) since in these cases we need to subtract just the random pions background. In the KK^* case, instead, we choose as sideband the candidates populating the D^* signal window but that have a lower $m_{K^+K^-}$ value ($m_{D^0} - 8\sigma < m_{K^+K^-} < m_{D^0} - 5\sigma$ where $\sigma = 8\,\mathrm{MeV}/c^2$), because of the presence of the multibody component; this is motivated by the fact that this mass range is the one in which the relative ratio of multibody decays and D^0 plus random pions yields better matches the one observed beneath the $D^{\star+} \to (K^+K^-)\pi^+$ peak in the signal region. Background was not subtracted from the distributions of the untagged sample. We simply selected decays with $K^+\pi^-$ or $K^-\pi^+$ mass within $24\,\mathrm{MeV}/c^2$ from the known D^0 mass, corresponding approximately to a cross–shaped $\pm 3\sigma$ range

in the two–dimensional distribution of Fig. 4.3. The background contamination in this region (about 6%) introduces a small imperfection in the reweighting procedure between tagged and untagged sample, that has a negligible impact on the final measurement as it will be described in Chap. 6 where a systematic uncertainty has been assessed for its possible effect.

We compared background–subtracted distributions for tagged $h^+h^{(\prime)-}$ decays, studying a large set of π_s kinematic variables (p_T, η, ϕ_0, d_0 and z_0). We observed small discrepancies only in the transverse momentum and pseudorapidity distributions as shown in Figs. 4.7 and Fig. 4.8. The ratio between the two distributions was used to extract a smooth curve used as a candidate–specific weight. A similar study of D^0 distributions (p_T, η and ϕ) for tagged and untagged $D^0 \to K^-\pi^+$ decays showed discrepancies only in the distributions of transverse momentum and pseudo–rapidity (see Fig. 4.9) which were reweighted accordingly.[2]

All entries in distributions shown in the remainder of this thesis are reweighted according to the transverse momentum and pseudo–rapidity of the corresponding candidates unless otherwise stated.

[2]In all cases, we assume that the two effects are indipendent, *i. e.* the total weight is the product of the p_T and η weights. We have verified *a posteriori* that this assumption is a good approximation.

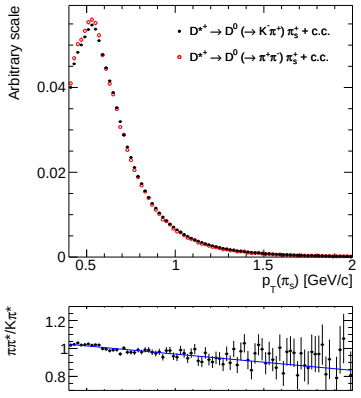

(a)

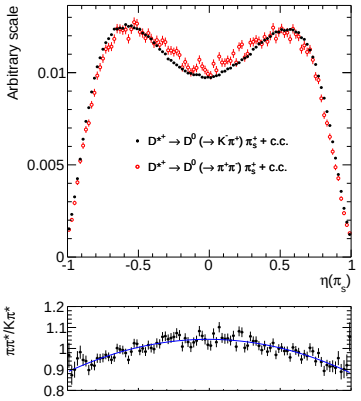

(b)

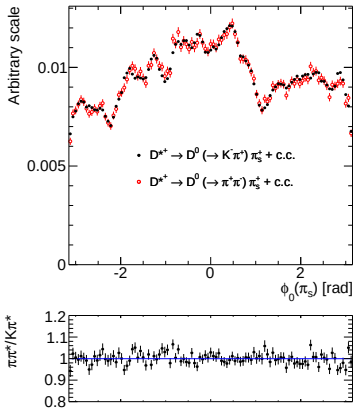

(c)

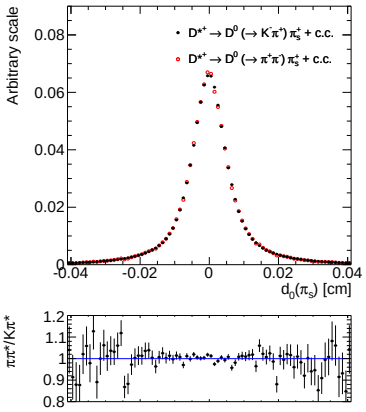

(d)

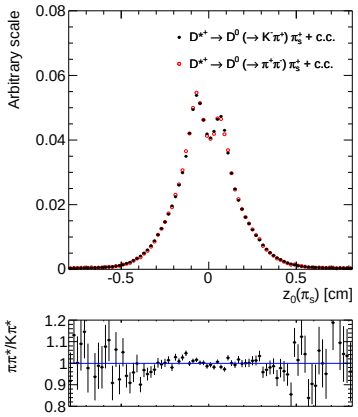

(e)

Figure 4.7: *Comparison between normalized kinematic distributions of $\pi\pi^*$ (red empty points) and $K\pi^*$ (black filled points) candidates: soft pion p_T (a), η (b), ϕ_0 (c), d_0 (d) and z_0 (e). Distributions are background–subtracted.*

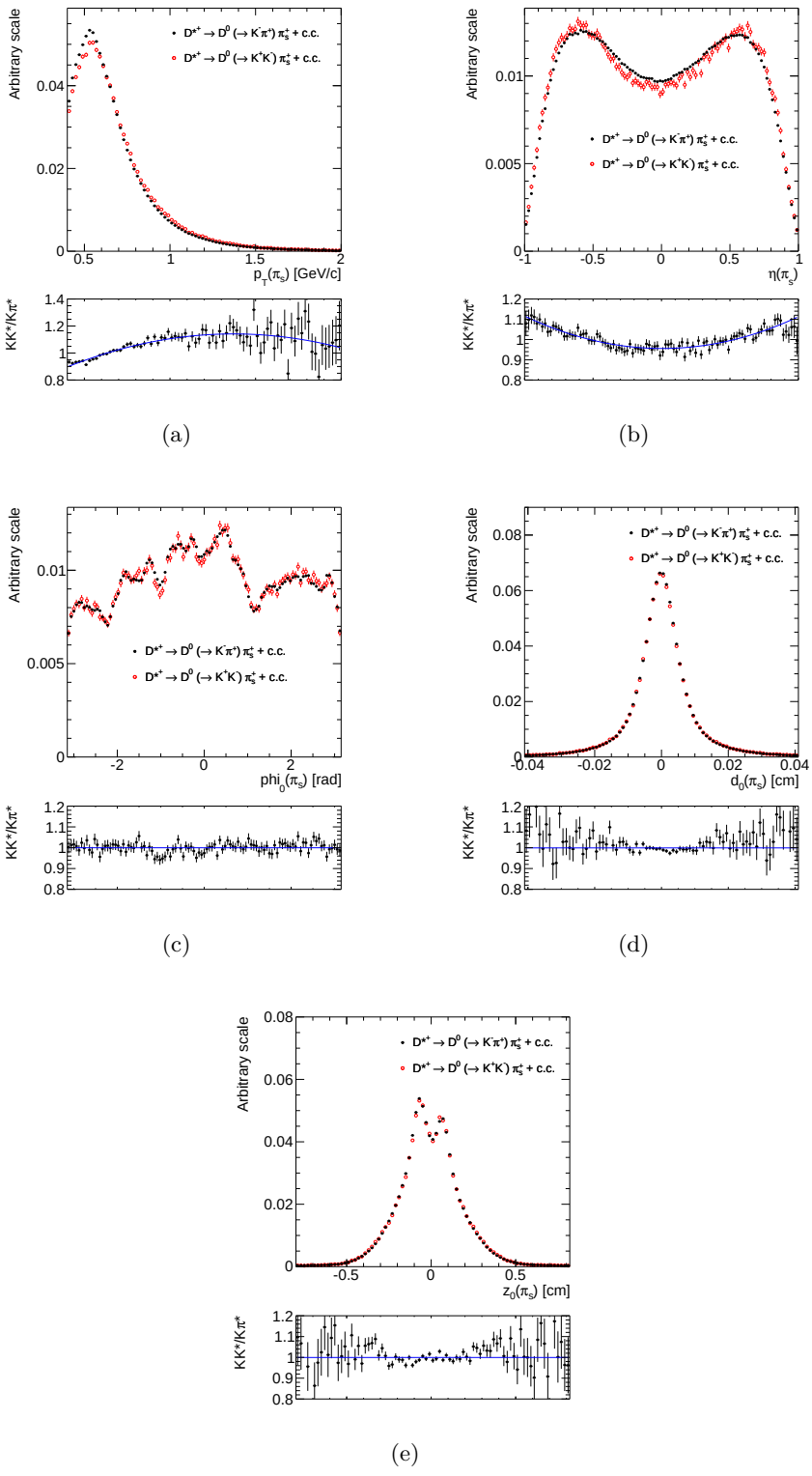

(a) (b) (c) (d) (e)

Figure 4.8: *Comparison between normalized kinematic distributions of KK^* (red empty points) and $K\pi^*$ (black filled points) candidates: soft pion p_T (a), η (b), ϕ_0 (c), d_0 (d) and z_0 (e). Distributions are background–subtracted.*

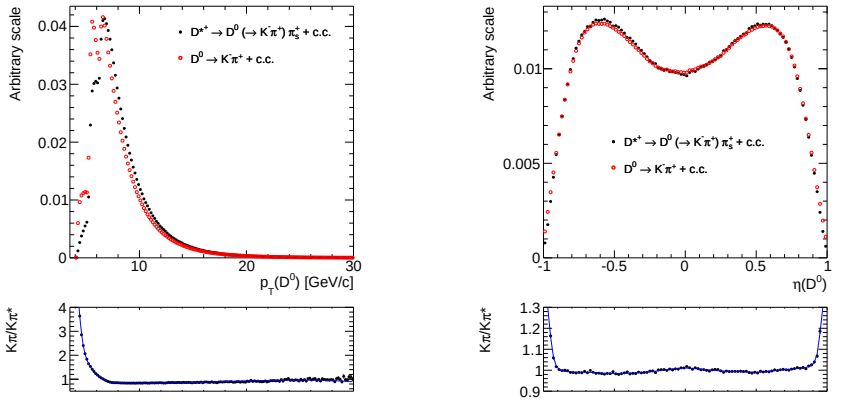

(a)

(b)

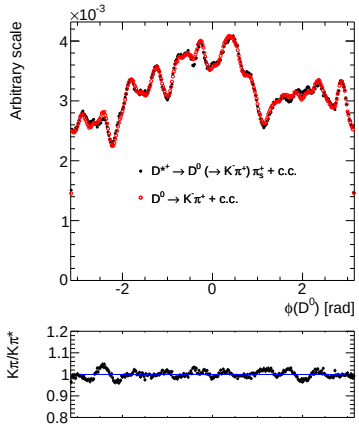

(c)

Figure 4.9: *Comparison between normalized kinematic distributions of tagged (black filled points) and untagged (red empty points) $D^0 \to K^-\pi^+$ candidates: D^0 transverse momentum (a), pseudo–rapidity (b) and azimutal angle (c). Tagged distributions are background–subtracted, untagged ones are not.*

Chapter 5

Determination of Observed Asymmetries

In the following we describe the method used to separate, on statistical basis, the charm yields from backgrounds and extract the observed asymmetries in the numbers of charm and anticharm mesons of the four event samples of interest.

5.1 Mass fits to extract the number of signal events

The asymmetries between observed numbers of D^0 and $\overline{D}^0$ signal candidates are determined with fits of the D^* (tagged samples) and D^0 (untagged sample) mass distributions. The mass resolution of the CDF tracker is sufficient to separate the different decay modes of interest. Backgrounds are modeled and included in the fits. In all cases we use a joint binned fit that minimizes a combined χ^2 quantity, defined as $\chi^2_{\rm tot} = \chi^2_+ + \chi^2_-$, where χ^2_+ and χ^2_- are the individual chi–squared for the D^0 and $\overline{D}^0$ distributions. Due to the large size of our samples, that have few precedents in high energy physics analyses, the use of an unbinned likelihood fit would require impractically large amounts of computing power and provide very little advantage in statistical precision. The functional form that describes the mass shape is assumed to be the same for charm and anticharm, although a few parameters are determined by the fit independently in the two samples. The functional form of the mass shape for all signals is obtained from simulation and the values of its parameters adjusted based on data. The effect of this adjustment is discussed in Chap. 6 where a systematic uncertainty is also assessed.

5.1.1 Fit of tagged samples

We extract the asymmetry of tagged samples by fitting the numbers of reconstructed $D^{*\pm}$ events in the $D^0\pi_s^+$ and $\overline{D}^0\pi_s^-$ mass distributions. Because all $D^0 \to h^+h^{(\prime)-}$ modes have the same $D^0\pi_s^+$ mass distribution (see Fig. 4.4), we use a single shape to fit all tagged signals. We also assume that the shape of the background from random pions associated with a real neutral charm particle are the same. Systematic uncertainties due to variations in the shapes are discussed in a later chapter.

The general features of the signal distribution are extracted from simulated samples. The model is adjusted and finalized in a fit of the $D^0\pi_s$ mass of copious and pure tagged $K^-\pi^+$ decays. We fit the average histogram of the charm and anticharm samples, $m = (m_+ + m_-)/2$, where m_+ is the D^{*+} mass distribution and m_- the D^{*-} one. The resulting signal shape is then used in the joint fit to measure the asymmetry between charm and anticharm signal yields.

The signal is described by a Johnson function [76],

$$\mathscr{J}(x|\mu,\sigma,\delta,\gamma) = \frac{1}{\mathscr{N}_J}\,\frac{e^{-\frac{1}{2}\left[\gamma\,+\,\delta\,\sinh^{-1}\left(\frac{x-\mu}{\sigma}\right)\right]^2}}{\sqrt{1+\left(\frac{x-\mu}{\sigma}\right)^2}},$$

that accounts for the asymmetric tail of the distribution, plus two Gaussians,

$$\mathscr{G}(x|\mu,\sigma) = \frac{1}{\mathscr{N}_G}\,e^{\frac{1}{2}\left(\frac{x-\mu}{\sigma}\right)^2},$$

for the central bulk:

$$\begin{aligned}\wp_{\rm sgn}(m|\vec{\theta}_{sgn}) = f_J\,\mathscr{J}(m|m_{D^*}+\mu_J,\sigma_J,\delta_J,\gamma_J)\\ +(1-f_J)\,[f_{G1}\mathscr{G}(m|m_{D^*}+\mu_{G1},\sigma_{G1})\\ +(1-f_{G1})\mathscr{G}(m|m_{D^*}+\mu_{G2},\sigma_{G2})]\,.\end{aligned}$$

The signal parameters $\vec{\theta}_{sgn}$ include the relative fraction, f_J, between the Johnson and the Gaussian components; the shift from the nominal $D^{*\pm}$ mass of the Johnson distribution's core, μ_J, and the two Gaussians, $\mu_{G1(2)}$; the widths of the Johnson distribution's core, σ_J, and the two Gaussians, $\sigma_{G1(2)}$; the parameters δ_J and γ_J determine, instead, the asymmetry in the Johnson distribution's tails.

For the random pion background we use an empirical shape form extracted from data by forming an artificial random combination of a well–reconstructed D^0 meson

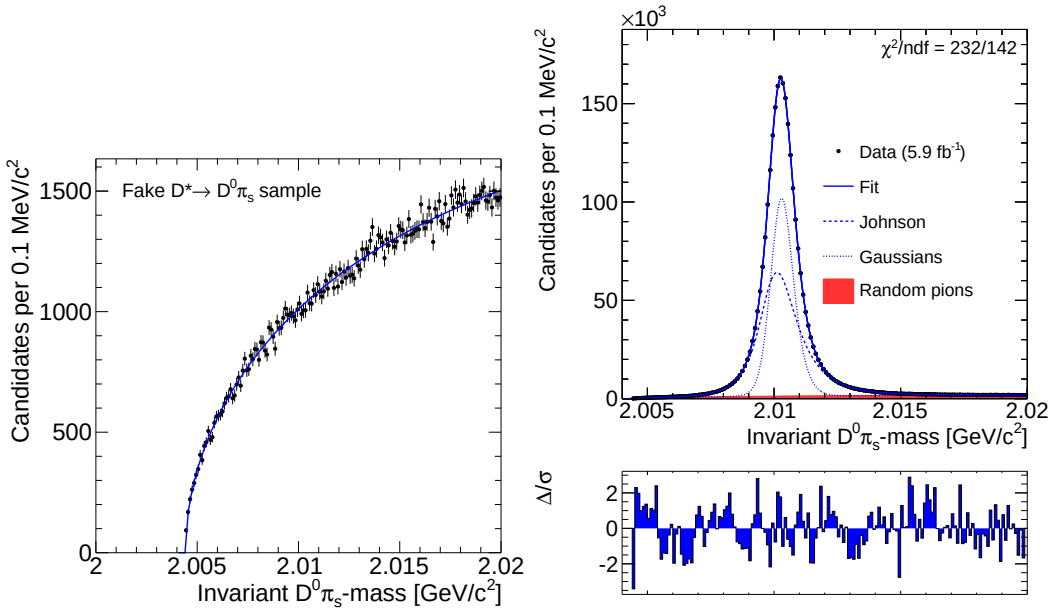

(a) (b)

Figure 5.1: *Distribution of $D^0\pi_s$ mass of a sample of fake $D^* \to D^0\pi_s$ decays artificially made through the combination of well–reconstructed D^0 mesons from an event with soft pions from all other events (a). Result of the preliminary fit to the $K\pi^*$ sample (b): the total fit projection (solid blue line) is shown along with the double Gaussian bulk (dotted blue line), the Johnson tail (dashed blue line) and the random pions background (filled red area).*

from each event combined with pions from other events (see Fig. 5.1 (a)):

$$\wp_{\rm bkg}(m|\vec{\theta}_{\rm bkg}) = \mathscr{B}(m|m_{D^0} + m_\pi, b_{\rm bkg}, c_{\rm bkg})$$

with

$$\mathscr{B}(x|a,b,c) = \frac{1}{\mathscr{N}_B}\,(x-a)^b e^{-c(x-a)}.$$

The total function used in this initial fit is

$$N_{\rm sgn}\wp_{\rm sgn}(m|\vec{\theta}_{\rm sgn}) + N_{\rm bkg}\wp_{\rm bkg}(m|\vec{\theta}_{\rm bkg}).$$

Each function is defined only above the threshold value of $m_{D^0}+m_\pi \approx 2.0044\,{\rm GeV}/c^2$ and is properly normalized in the fit range, which extends from threshold up to $2.02\,{\rm GeV}/c^2$, through the coefficients $\mathscr{N}_J$, $\mathscr{N}_G$ and $\mathscr{N}_B$.

Fig. 5.1 (b) shows the results of this preliminary fit where all parameters have been left free to float. Despite the huge number of events fitted, about 5.5 million,

Parameter	Units	Fitted value and error
f_J	–	0.54 ± 0.03
μ_J	MeV/c^2	-0.34 ± 0.02
σ_J	MeV/c^2	0.97 ± 0.07
γ_J	–	-0.38 ± 0.02
δ_J	–	1.14 ± 0.03
f_{G1}	–	0.59 ± 0.02
μ_{G1}	MeV/c^2	$(5 \pm 8) \times 10^{-3}$
σ_{G1}	MeV/c^2	0.391 ± 0.005
μ_{G2}	MeV/c^2	0.19 ± 0.03
σ_{G2}	MeV/c^2	0.60 ± 0.01

Table 5.1: *Values of D^* signal shape parameters as extracted from the preliminary fit of Fig. 5.1. Parameters which are zero within 1σ are fixed to zero in the subsequent analysis.*

the projection of the fit function is in very good agreement with the data histogram, with a χ^2/ndf of 232/142, as also demonstrated by distribution of the normalized residuals shown by the bottom plot.

We then fix the resulting signal parametrization (see Tab. 5.1) and simultaneously fit the $D^0\pi_s$ mass distributions of D^{*+} and D^{*-} candidates with independent normalizations to extract the asymmetry. As an exception the parameter δ_J is not fixed, but varies independently for charm and anticharm decays for reasons that will be explained later in this section. The background shape parameters, $b_{\rm bkg}$ and $c_{\rm bkg}$, are common in the two samples and are also determined by the fit. Fig. 5.2 (a) and (b) show the projections of this simultaneous fit on the $D^0\pi_s$ mass distribution, for the tagged $D^0 \to K^-\pi^+$ sample, as well as the value of the combined χ^2 at the minimum which is 385 per 304 degrees of freedom.

Fig. 5.2 (c) shows the projection on the asymmetry distribution as a function of the $D^0\pi_s$ mass. The asymmetry histogram, a, is constructed by evaluating the bin–by–bin asymmetry from the two mass histograms $a = (m_+ - m_-)/(m_+ + m_-)$. The variation of the asymmetry as a function of mass indicates backgrounds with asymmetries different from the signal one. As shown by the plot of the relative difference between the fit and the data at the bottom of Fig. 5.2 (c), the fit correctly

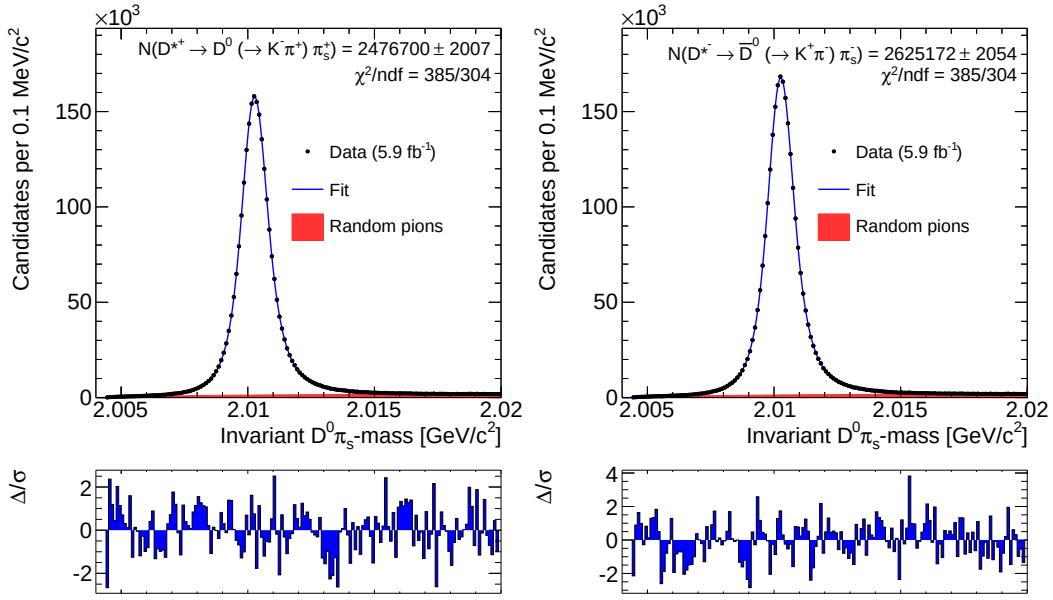

(a) (b)

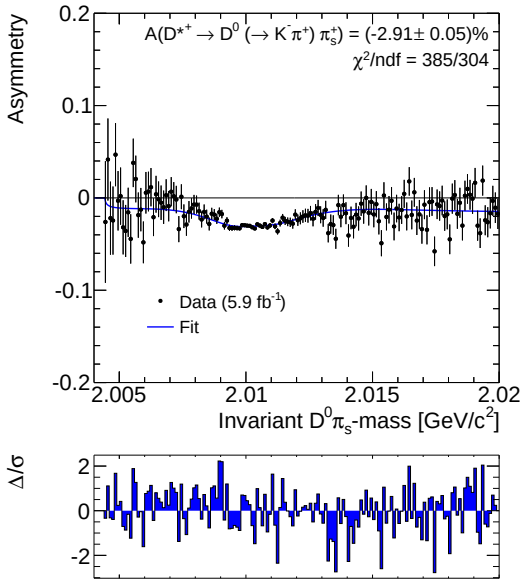

(c)

Figure 5.2: *Results of the combined fit of the tagged $D^0 \to K^-\pi^+$ sample. Distribution of $D^0\pi_s$ mass for charm (a), and anticharm (b) decays, and asymmetry as a function of the mass (c). Fit results are overlaid.*

describes the asymmetry across the whole mass range.

We allowed independent δ_J parameters in the charm and anticharm samples because the $D^0\pi_s$ mass distribution for D^{*+} candidates exhibits slightly larger tails and a different width than the corresponding distribution for D^{*-} candidates. The relative difference between the fitter δ_J values is

$$A(\delta_J) = \frac{\delta_J^{D^{*+}} - \delta_J^{D^{*-}}}{\delta_J^{D^{*+}} + \delta_J^{D^{*-}}} = (-4.4 \pm 0.8) \times 10^{-3}.$$

By allowing the parameter δ_J to vary independently for charm and anticharm decays the χ^2/ndf value improves from 414/306 to 385/304. We do not expect this difference to be due to an asymmetric background because the difference is maximally visible in the signal region, where the kinematic correlation between $D^0\pi_s$ mass and π_s transverse momentum is stronger. Indeed, small differences between D^{*+} and D^{*-} shapes may be expected because the drift chamber has different resolutions for positive and negative particles at low momenta. We allowed independent δ_J parameters for our central fit, because this provides a significantly improved description of the asymmetry as a function of $D^0\pi_s$ mass in the signal region (Fig. 5.2 (c)). In Sect. 6.1.4 we report a systematic uncertainty associated with this assumption. No significant improvement in fit quality is observed when leaving other signal shape parameters free to vary independently for D^{*+} and D^{*-} candidates.

The background's shape parameters are fitted to be $b_{\rm bkg} = 0.67 \pm 0.01$ and $c_{\rm bkg} = 37 \pm 2\,{\rm GeV}^{-1}c^2$; as for the signal shape, these are then fixed when fitting the tagged $D^0 \to h^+h^-$ samples.

The plots in Figs. 5.3 and 5.4 show the fit results for tagged $D^0 \to \pi^+\pi^-$ and $D^0 \to K^-K^+$ samples, respectively. In the $D^0 \to K^+K^-$ fit we include an additional component from mis–reconstructed multibody decays. Because signal plus random pion shapes are fixed to those obtained by fitting the tagged $K\pi$ sample (Fig. 5.2), the shape of this additional multibody component is conveniently extracted from the combined fit on data and is described by

$$\wp_{\rm mbd}(m|\vec{\theta}_{\rm mbd}) = f_{\rm mdb} J(m|m_{D^*} + \mu_{\rm mbd}, \sigma_{\rm mbd}, \delta_{\rm mbd}, \gamma_{\rm mbd}) + (1 - f_{\rm mbd})\mathscr{B}(m|m_{D^0} + m_\pi, b_{\rm mbd}, c_{\rm mbd}).$$

The total function used to fit the KK^* sample is then

$$N_{\rm sgn}\wp_{\rm sgn}(m|\vec{\theta}_{\rm sgn}) + N_{\rm bkg}\wp_{\rm bkg}(m|\vec{\theta}_{\rm bkg}) + N_{\rm mbd}\wp_{\rm mbd}(m|\vec{\theta}_{\rm mbd}).$$

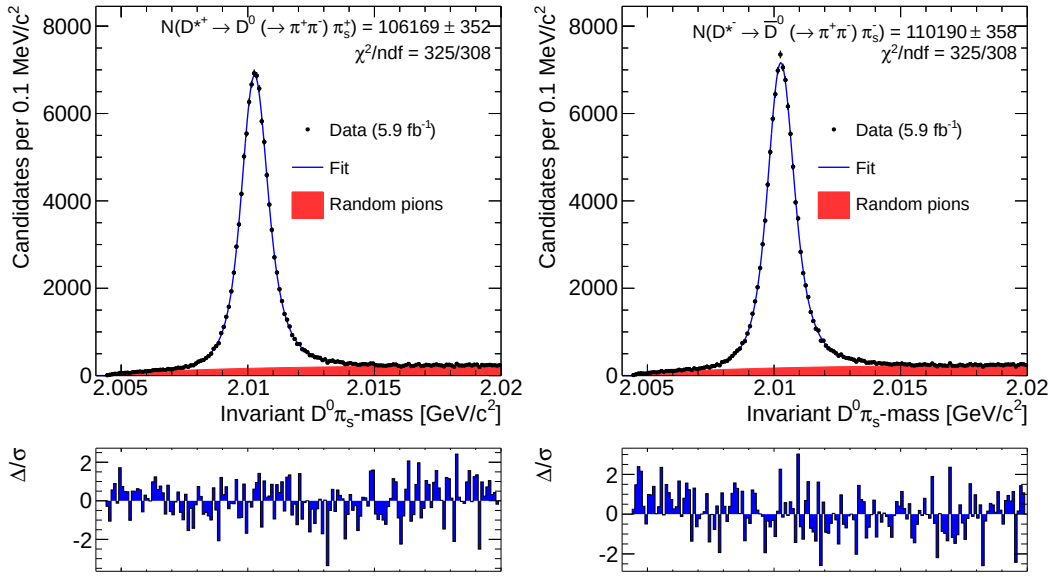

(a) (b)

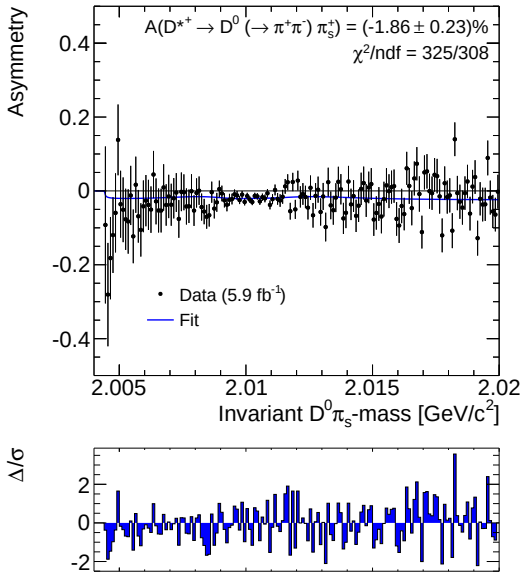

(c)

Figure 5.3: *Results of the combined fit of the tagged $D^0 \to \pi^+\pi^-$ sample. Distribution of $D^0\pi_s$ mass for charm (a), and anticharm (b) decays, and asymmetry as a function of the mass (c). Fit results are overlaid.*

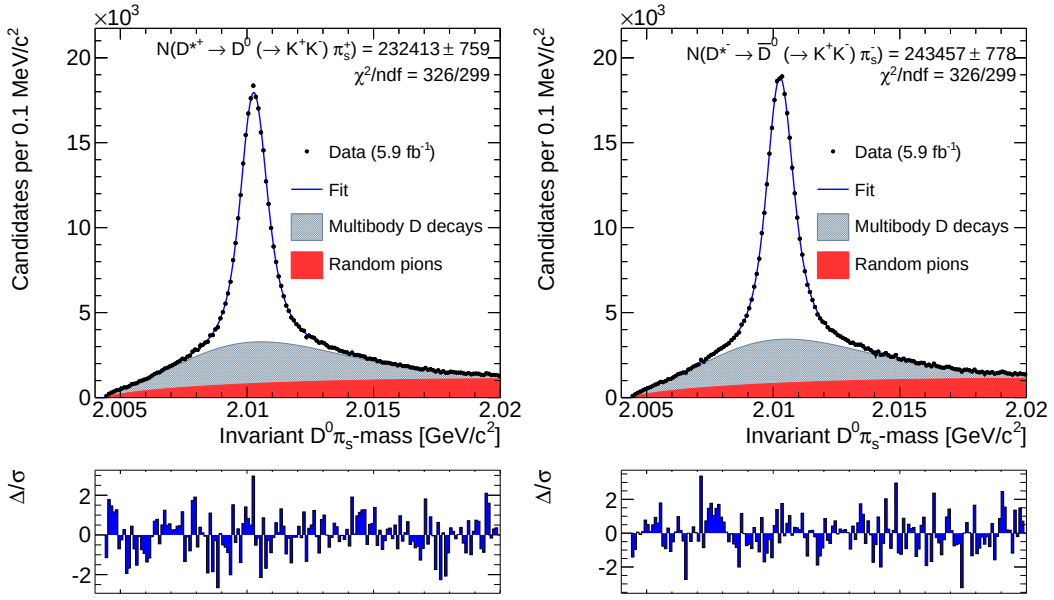

(a) (b)

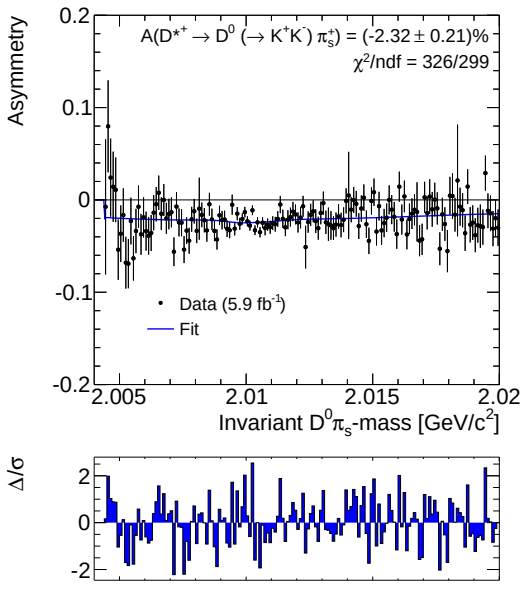

(c)

Figure 5.4: *Results of the combined fit of the tagged $D^0 \to K^+K^-$ sample. Distribution of $D^0\pi_s$ mass for charm (a) and anticharm (b) decays, and asymmetry as a function of the mass (c). Fit results are overlaid.*

Parameter	Units	Fitted value and error
f_{mbd}	–	0.14 ± 0.02
μ_{mbd}	MeV/c^2	-11.65 ± 0.07
σ_{mbd}	MeV/c^2	0.236 ± 0.002
γ_{mbd}	–	-18.14 ± 0.03
δ_{mbd}	–	3.880 ± 0.007
b_{mbd}	–	0.97 ± 0.05
c_{mbd}	GeV$^{-1}c^2$	310 ± 32

Table 5.2: *Shape parameters of the multibody D decays component as extracted from the fit of the KK^* sample.*

The resulting shape parameters for the multibody D decays component are listed in Tab. 5.2.

We observe the following asymmetries for signals in the three tagged samples:

$$A(\pi\pi^*) = (-1.86 \pm 0.23)\%, \tag{5.1}$$

$$A(KK^*) = (-2.32 \pm 0.21)\%, \tag{5.2}$$

$$A(K\pi^*) = (-2.910 \pm 0.049)\%. \tag{5.3}$$

From the fits we extract also the asymmetries of the backgrounds:

$$\begin{aligned} A(\text{random pions}, \pi\pi^*) &= (-2.42 \pm 0.55)\%, \\ A(\text{random pions}, KK^*) &= (-1.30 \pm 0.50)\%, \\ A(\text{random pions}, K\pi^*) &= (-1.55 \pm 0.28)\%, \\ A(\text{multibody}) &= (-2.66 \pm 0.43)\%. \end{aligned} \tag{5.4}$$

As a sanity check, we note that A(random pions) is measured to be consistent within the three tagged sample. Moreover, the raw asymmetry of the partially reconstructed multibody decays is also compatible with the one of Eq. (5.3): this background is mainly composed of $D^{*+} \to D^0(\to K^-\pi^+\pi^0)\pi_s^+$ decays where the neutral pion is not reconstructed and then, if we neglect possible CP–violating effects, it is expected to show the same detector–induced asymmetry of the fully reconstructed $D^{*+} \to D^0(\to K^-\pi^+)\pi_s^+$ decay, once the kinematic distributions of the soft pion are equalized.

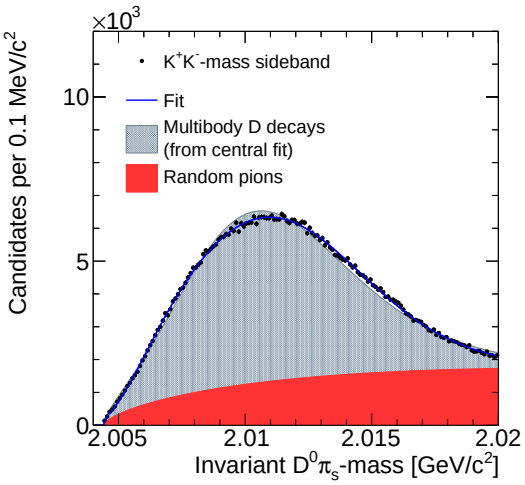

Figure 5.5: *Comparison between the multibody D decays shape used in the KK^* fit with data events in the sideband region $m_{D^0} - 8\sigma < m_{K^+K^-} < m_{D^0} - 5\sigma$ where $\sigma = 8\,\mathrm{MeV}/c^2$.*

Moreover, to check the reliability of the shape of multibody D decays obtained in the KK^* fit, we compared it with an alternative one obtained from sideband data ($m_{D^0} - 8\sigma < m_{K^+K^-} < m_{D^0} - 5\sigma$ where $\sigma = 8\,\mathrm{MeV}/c^2$) as shown in Fig. 5.5. The shape estimated by the central fit describes the sideband data fairly well; the small differences may be expected since the composition of the $m_{K^+K^-}$ sideband in terms of physics background may be not the same as the one in the signal region ($|m_{K^+K^-} - m_{D^0}| < 24\,\mathrm{MeV}/c^2$). Nevertheless, if we repeat the KK^* fit fixing the $D^0\pi_s$ mass shape of the multibody D decays component to the one obtained fitting the sideband data (blue curve of Fig. 5.5) the value of the $A(KK^*)$ changes by no more than 5×10^{-4}, thus increasing our confindence in our fitting procedure.

5.1.2 Fit of the untagged sample

In untagged $K\pi$ decays no soft pion is associated with the neutral charm to form a D^* candidate so there is no identification of its charm or anticharm content. We infer the flavor of the neutral charm meson on a statistical basis using the mass resolution of the tracker and the quasi–flavor-specific nature of neutral charm decays into $K\pi$ final states. The role of mass resolution is evident in Fig. 4.3, which shows the distribution of $K^-\pi^+$ mass as a function of $K^+\pi^-$ mass for the sample

of untagged $D^0 \to h^+h^{(\prime)-}$ decays. The cross–shaped structure at the center of the plot is dominated by $K\pi$ decays. In each mass projection the narrow component of the structure is due to decays where the chosen $K\pi$ assignment is correct. The broader component is due to decays where the $K\pi$ assignment is swapped. In the momentum range of interest, the observed widths of these two components differ by an order of magnitude. Because of the CKM hierarchy of couplings, approximately 99.6% of neutral charm decays into a $K^-\pi^+$ final state are from Cabibbo–favored decays of D^0 mesons, while only 0.4% by the doubly–Cabibbo–suppressed decays of $\overline{D}^0$ mesons, and viceversa for $K^+\pi^-$ decays. Therefore, the narrow (broad) component in the $K^-\pi^+$ projection is dominated by D^0 ($\overline{D}^0$) decays. Similarly, the narrow (broad) component in the $K^+\pi^-$ projection is dominated by $\overline{D}^0$ (D^0) decays.

We determine the number of charm and anticharm decays with a joint fit of the $K^+\pi^-$ and $K^-\pi^+$ mass distributions. We randomly divide the data into two independent sub–samples, equal in size, whose events are evenly distributed in time ("odd" and "even" samples). We arbitrarily chose to reconstruct the $K^-\pi^+$ mass for candidates of the odd sample and the $K^+\pi^-$ mass for candidates of the even sample. In the odd sample the decay $D^0 \to K^-\pi^+$ is considered "right sign" (RS) because it is reconstructed with proper mass assignment. In the even sample it is considered a "wrong sign" (WS) decay, since it is reconstructed with swapped mass assignment. The opposite holds for the $\overline{D}^0 \to K^+\pi^-$ decay.

We extract the asymmetry in the untagged sample from a joint binned fit of the two sub–samples. The shapes used are the same for odd and even samples. The fit determines the number of $D^0 \to K^-\pi^+$ (RS decays) from the odd sample and the number of $\overline{D}^0 \to K^+\pi^-$ (RS decays) from the even sample.[1] We split the total untagged sample in half to avoid the need to account for correlations. The reduction in statistical power has little practical effect since half of the untagged $K\pi$ decays is still a factor 30 (67) more abundant than the tagged K^+K^- ($\pi^+\pi^-$) decays, and the corresponding statistical uncertainty gives a negligible contribution to the uncertainty of the final result.

The mass shapes used in the combined fit of the untagged sample are extracted

[1] For this reason we will indicate the different components without mentioning the charge in the final state: $D \to K\pi$ RS, $D \to K\pi$ WS, $D \to \pi\pi$.

from simulated events and adjusted by fitting the $K\pi$ mass distribution in data. All functions described in the following are properly normalized when used in fits.

The mass line shape of RS ($D^0 \to K^-\pi^+$ and $\overline{D}^0 \to K^+\pi^-$) decays is parameterized using the following analytical expression:

$$\begin{aligned}\wp_{\rm RS}(m|\vec{\theta}_{\rm RS}) = f_{{\rm RS}T}\mathscr{T}(m|m_{D^0}+\mu_{\rm RS1},\alpha_{\rm RS},\beta_{\rm RS}) \\ + (1-f_{{\rm RS}T})\Big[f_{\rm RS1}\mathscr{G}(m|m_{D^0}+\mu_{\rm RS1},\sigma_{\rm RS1}) \\ + (1-f_{\rm RS1})\mathscr{G}(m|m_{D^0}+\mu_{\rm RS2},\sigma_{\rm RS2})\Big],\end{aligned}$$

where

$$\mathscr{T}(x|\mu,\alpha,\beta) = \frac{1}{\mathscr{N}_T}\, e^{\alpha(x-\mu)}{\rm Erfc}(\beta(x-\mu))$$

with $\mathscr{N}_T$ normalization factor and ${\rm Erfc}(x) = \frac{2}{\sqrt{\pi}}\int_x^{+\infty} e^{-t^2}dt$. We use the sum of two Gaussians to parameterize the bulk of the distribution, while the function $\mathscr{T}$ describes the tail at lower masses due to the soft photon emission. The parameter $f_{{\rm RS}T}$ is the relative contribution of the tail. The parameters $\mu_{\rm RS1(2)}$ are possible shifts in mass from the known D^0 mass. Because the soft photon emission makes the mass distribution asymmetric, the means of the Gaussians cannot be assumed to be the same. Therefore m_{D^0} is fixed in the parameterization while $\mu_{\rm RS1(2)}$ are determined by the fit.

The mass distribution of WS ($D^0 \to K^+\pi^-$ and $\overline{D}^0 \to K^-\pi^+$) decays is parameterized using the same functional form used to model RS decays, but has different parameters: $\wp_{\rm WS}(m|\vec{\theta}_{\rm WS})$.

The mass distribution of $D^0 \to \pi^+\pi^-$ decays is modeled using the following functional form:

$$\begin{aligned}\wp_{\pi\pi}(m|\vec{\theta}_{\pi\pi}) = +f_{T1}\mathscr{T}(m|m_0+\mu_{T1},\alpha_{T1},\beta_{T1}) + f_{T2}\mathscr{T}(m|m_0+\mu_{T2},\alpha_{T2},\beta_{T2}) \\ + (1-f_{T1}-f_{T2})\Big[f_{\pi\pi1}\mathscr{G}(m|m_0+\mu_{\pi\pi1},\sigma_{\pi\pi1}) \\ + (1-f_{\pi\pi1})\mathscr{G}(m|m_0+\mu_{\pi\pi2},\sigma_{\pi\pi2})\Big].\end{aligned}$$

The bulk of the distribution is described by two Gaussians. Two tail functions $\mathscr{T}$ are added for the low and high–mass tails due to soft photon emission and incorrect mass assignment, respectively. The parameters $\mu_{\pi\pi1(2)}$ and $\mu_{T1(2)}$ represent shifts in

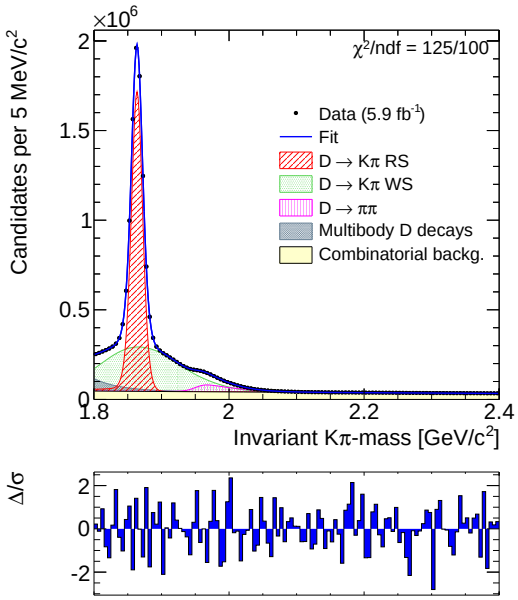

Figure 5.6: *Average (m) of the distribution of $K^+\pi^-$ mass in the even sample and $K^-\pi^+$ mass in the odd sample with fit projections overlaid.*

mass from the empirical value of the most probable $m_{K\pi}$ mass of the mis–assigned $D^0 \to \pi^+\pi^-$ decays, $m_0 = 1.967\,\mathrm{GeV}/c^2$, which is fixed in the fit.

The mass distributions of the partially reconstructed multibody decays and combinatorial background are modeled using decreasing exponential functions,

$$\mathscr{E}(m|\lambda) = \frac{1}{\mathscr{N}_E}\, e^{\lambda(m-m_{\min})},$$

with coefficients λ_{mbd} and λ_{comb}, respectively. $\mathscr{N}_E$ is a normalization factor and $m_{\min}$ is fixed to the lower edge of the fit range ($1.8\,\mathrm{GeV}/c^2$).

The function used in the fit is then

$$N_{\mathrm{RS}}\wp_{\mathrm{RS}}(m|\vec{\theta}_{\mathrm{RS}}) + N_{\mathrm{WS}}\wp_{\mathrm{WS}}(m|\vec{\theta}_{\mathrm{WS}}) + N_{\pi\pi}\wp_{\pi\pi}(m|\vec{\theta}_{\pi\pi}) + N_{\mathrm{mbd}}\wp_{\mathrm{mbd}}(m|b_{\mathrm{mbd}}) + N_{\mathrm{comb}}\wp_{\mathrm{comb}}(m|b_{\mathrm{comb}}),$$

where N_{RS}, N_{WS}, $N_{\pi\pi}$, N_{mbd}, N_{comb} are the event yields for RS decays ($D^0 \to K^-\pi^+$ and $\overline{D}^0 \to K^+\pi^-$), WS decays ($D^0 \to K^+\pi^-$ and $\overline{D}^0 \to K^-\pi^+$), $D^0 \to \pi^+\pi^-$ decays, partially reconstructed multibody decays, and combinatorial background, respectively.

The fit is limited to the mass range $[1.8, 2.4]\,\mathrm{GeV}/c^2$ to avoid the need for modeling most of the partially reconstructed charm meson decays. The ratio $N_{\mathrm{RS}}/N_{\mathrm{mbd}}$

and the parameter $\lambda_{\rm mbd}$ are fixed from simulated inclusive D^0 and D^+ decays. The contamination from partially reconstructed D_s^+ decays is negligible for masses greater that $1.8\,\mathrm{GeV}/c^2$.

The result of the fit of the average histogram is shown in Fig. 5.6. In this preliminary fit we let the number of events vary in each of the various components, the parameters of the two Gaussians describing the bulk of the $D^0 \to h^+h^{(\prime)-}$ distributions, and the slope of the combinatorial background $\lambda_{\rm comb}$. We assume that the small tails are described accurately enough by the simulation. The resulting shape parameters with relative errors are listed in Tab. 5.3.

Odd and even samples are fitted jointly using the same shapes for each component to determine the asymmetry of RS decays. All shape parameters are fixed to the ones extracted in the preliminary fit, with the only exception of the slope of the combinatorial background which is left free to vary and constrained to be the same between odd and even samples. Because by construction no asymmetry in $D^0 \to \pi^+\pi^-$ decays and combinatorial background is expected, we include the following constraints: $N_{\pi\pi}^{\rm odd} = N_{\pi\pi}^{\rm even}$ and $N_{\rm comb}^{\rm odd} = N_{\rm comb}^{\rm even}$, while the other yields are determined by the fit independently in the two samples. Fig. 5.7 (a) and (b) show the fit projections for odd and even samples. Fig. 5.7 (c) shows the projection of the simultaneous fit on the asymmetry as a function of the $K\pi$ mass. The combined χ^2/ndf at the minimum is 249/231, extremely good for a sample of about 30 million events.

The observed asymmetry for the $D^0 \to K^-\pi^+$ RS decays is

$$A(K\pi) = (-0.832 \pm 0.033)\%. \tag{5.5}$$

The asymmetry for the WS decays ($D^0 \to K^-\pi^+$ and $\overline{D}^0 \to K^+\pi^-$ decays reconstructed with the swapped mass assignment to their final state particles) is estimated to be $(+0.651 \pm 0.052)\%$. By construction the WS raw asymmetry must be equal in size, and opposite in sign, to the RS one within the uncertainties. Considering the two measurements as independent, we find a statistical discrepancy of 3.4σ. This discrepancy is however mis–leading because, while the estimate of the asymmetry of the RS decays is very reliable, as we will see when systematic uncertainties will be discussed, the estimate of the raw asymmetry in the WS decays is affected by much larger systematic errors due to the uncertainty in the shape of

Parameter	Units	Fitted value and error
f_{RS1}	–	0.47 ± 0.01
μ_{RS1}	MeV/c^2	-1.30 ± 0.02
σ_{RS1}	MeV/c^2	10.77 ± 0.08
μ_{RS2}	MeV/c^2	-1.07 ± 0.01
σ_{RS2}	MeV/c^2	7.23 ± 0.04
$f_{\mathrm{RS}T}$	–	2.77×10^{-2} (fixed from simulation)
α_{RS}	$\mathrm{GeV}^{-1}c^2$	13.2 (fixed from simulation)
β_{RS}	$\mathrm{GeV}^{-1}c^2$	57.4 (fixed from simulation)
f_{WS1}	–	0.44 ± 0.05
μ_{WS1}	MeV/c^2	52 ± 3
σ_{WS1}	MeV/c^2	51 ± 1
μ_{WS2}	MeV/c^2	-17 ± 2
σ_{WS2}	MeV/c^2	44.7 ± 0.8
$f_{\mathrm{WS}T}$	–	0.14 (fixed from simulation)
α_{WS}	$\mathrm{GeV}^{-1}c^2$	6.17 (fixed from simulation)
β_{WS}	$\mathrm{GeV}^{-1}c^2$	31.3 (fixed from simulation)
$f_{\pi\pi 1}$	–	0.77 ± 0.06
$\mu_{\pi\pi 1}$	MeV/c^2	-5.8 ± 0.3
$\sigma_{\pi\pi 1}$	MeV/c^2	13.4 ± 0.3
$\mu_{\pi\pi 2}$	MeV/c^2	60 ± 20
$\sigma_{\pi\pi 2}$	MeV/c^2	56 ± 5
f_{T1}	–	5.58×10^{-2} (fixed from simulation)
μ_{T1}	MeV/c^2	24.7 (fixed from simulation)
α_{T1}	$\mathrm{GeV}^{-1}c^2$	19.9 (fixed from simulation)
β_{T1}	$\mathrm{GeV}^{-1}c^2$	151.8 (fixed from simulation)
f_{T2}	–	62.8×10^{-2} (fixed from simulation)
μ_{T2}	MeV/c^2	15.5 (fixed from simulation)
α_{T2}	$\mathrm{GeV}^{-1}c^2$	-29.6 (fixed from simulation)
β_{T2}	$\mathrm{GeV}^{-1}c^2$	-35.1 (fixed from simulation)
λ_{mbd}	$\mathrm{GeV}^{-1}c^2$	-25.57 (fixed from simulation)

Table 5.3: *Shape parameters of RS (top), WS (middle top), $D \to \pi\pi$ (middle bottom) and multibody D (bottom) decays as extracted from the preliminary fit of Fig. 5.6. Parameters which are zero within 1σ are fixed to zero in the subsequent analysis.*

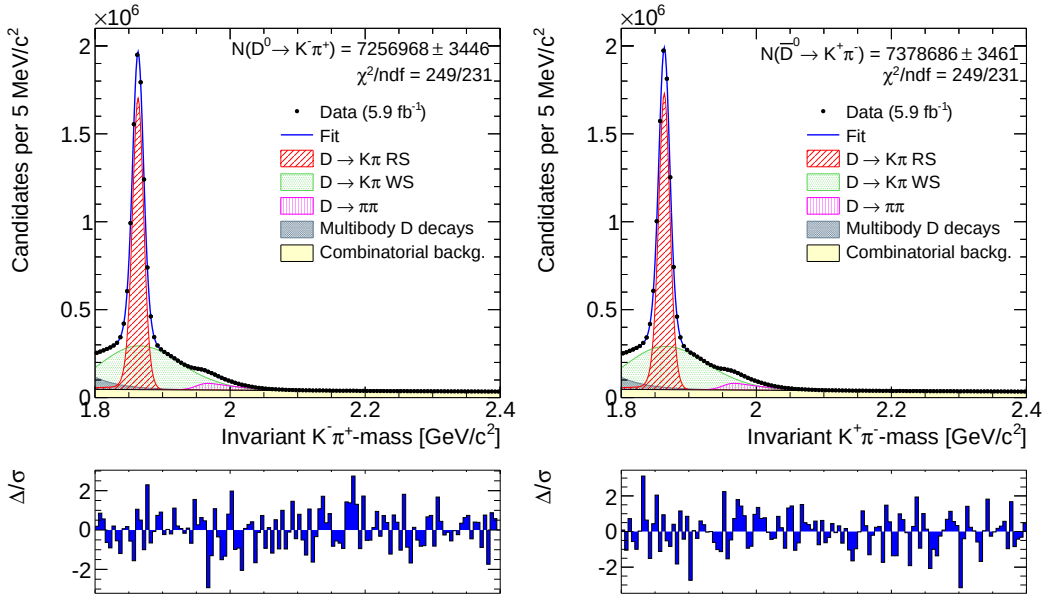

(a) (b)

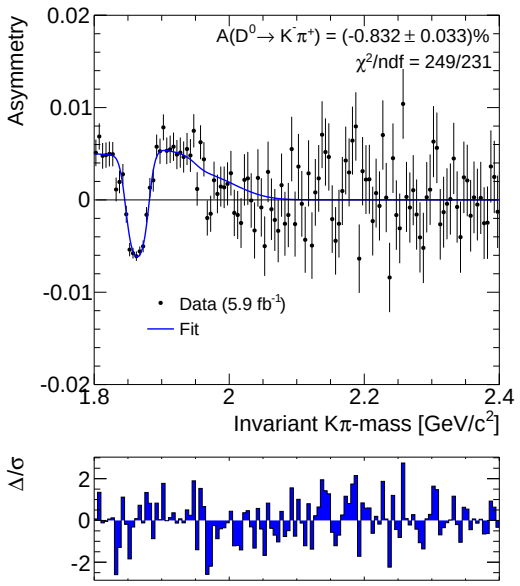

(c)

Figure 5.7: *Results of the combined fit of the untagged $D^0 \to K^-\pi^+$ sample. Distribution of $K^-\pi^+$ mass for the odd sample (a), $K^+\pi^-$ mass for the even sample (b) and asymmetry as a function of the mass (c). Fit results are overlaid.*

the mass distribution that are difficult to estimate reliably.[2] Therefore we chose to use only the value of the asymmetry derived from the RS mass peak and ignore the value derived from the WS. However, as a cross-check, we repeated the fit enforcing $A(K\pi) = A(\mathrm{RS}) = -A(\mathrm{WS})$. With this constraint the fit measures an anymmetry which differs from Eq. (5.5) by 0.034%. Such a difference is smaller than the systematic uncertanty we asses in Sect. 6.1.5 for the assumed RS and WS mass shapes.

The raw asymmetry of the partially reconstructed multibody D decays is measured to be $(0.76 \pm 0.36)\%$. The combinatorial background slope if found to be $\lambda_{\mathrm{comb}} = -0.546 \pm 0.005\,\mathrm{GeV}^{-1}c^2$.

5.2 Corrected asymmetries and stat only result

Combining the observed asymmetry in the D^*–tagged $D^0 \to \pi^+\pi^-$ ($D^0 \to K^+K^-$) decays, Eq. (5.1) (Eq. (5.2)), with the ones observed in the two Cabibbo–favored samples, Eq. (5.3) and Eq. (5.5), through Eq. (3.8) we measure the time–integrated CP–violating asymmetries in $D^0 \to h^+h^-$ decays

$$\mathcal{A}_{\mathrm{CP}}(D^0 \to \pi^+\pi^-) = (+0.22 \pm 0.24)\%, \tag{5.6}$$

$$\mathcal{A}_{\mathrm{CP}}(D^0 \to K^+K^-) = (-0.24 \pm 0.22)\%, \tag{5.7}$$

where the errors still do not contain any contribution from systematic sources. As expected from the huge number of reconstructed decays, this measurement has the potential to become the most precise to date, with statistical uncertainties that are about 1/2 (2/3) of current B–factories results (see Tab. 1.1) for the $D^0 \to \pi^+\pi^-$ ($D^0 \to K^+K^-$) mode, if systematic uncertainties are kept under control.

While a detailed comparison with B–factories measurements will be presented in Chap. 7, after systematic uncertainties will be assed (see Chap. 6), here we want to stress the improvement with respect to previous CDF measurements performed on the first $123\,\mathrm{pb}^{-1}$ of integrated luminosity, where about 7 000 (16 000) $D^0 \to \pi^+\pi^-$

[2] A detailed study of the mass shape of WS decays implies also a detailed knowledge of the tail of partially reconstructed charm decays at masses larger than $1.8\,\mathrm{GeV}/c^2$. In our fit, instead, we assume a simplified model for this component and we use a single mass shape to inclusively model all D^0 and $D^+_{(s)}$ decays in both RS and WS mass assignments.

$(D^0 \to K^+K^-)$ decays were reconstructed [56]:

$$\begin{aligned} \mathcal{A}_{\rm CP}(D^0 \to \pi^+\pi^-) &= (+1.0 \pm 1.3\ (stat.) \pm 0.6\ (syst.))\%, \\ \mathcal{A}_{\rm CP}(D^0 \to K^+K^-) &= (+2.0 \pm 1.2\ (stat.) \pm 0.6\ (syst.))\%, \end{aligned} \qquad \text{(CDF on } 123\,\text{pb}^{-1}\text{)}.$$

In doing such a comparison is important to note that, apart from the factor 6 improvement due to the growth in number of events analyzed, our results of Eqs. (5.6) and (5.7) already include the charge asymmetry correction for the soft pion's reconstruction efficiency, while this effect is accounted in (and is essential the only contribution to) the total systematic uncertainties of the previous measurement. The fully data–driven methodology, developed and used in this thesis, to correct for detector–induced asymmetries represents then an important improvement with respect to the previous analysis where a mixture of data–driven and simulation–based corrections were instead used.

Chapter 6

Evaluation of Systematic Uncertainties

In this chapter we discuss and asses the systematic uncertanties which affect our measurements, showing that thanks to completely data–driven method used in the analysis they do not dominate the uncertainty on the final result.

6.1 Source of systematic uncertainties

The strategy of the measurement is designed to strongly suppress systematic uncertainties. However, we still need to consider a few residual sources that can impact the results: approximations in the suppression of detector–induced asymmetries; production asymmetries; contamination from secondary D mesons; assumptions and approximations in fits, which include specific choice of analytic shapes, differences between distributions associated with charm and anticharm decays, and contamination from unaccounted backgrounds; and finally assumptions and limitations of kinematic reweighting.

Most of the systematic uncertainties are evaluated by modifying the fit functions to include systematic variations and repeat the fits on data. The differences between results of modified fits and the central one are used as systematic uncertainties. This usually overestimates the observed size of systematic uncertainties, which include an additional statistical component. However, the additional uncertainty is negligible, given the size of the event samples involved. All sources of systematic uncertainty are detailed below. A summary is given in Tab. 6.2.

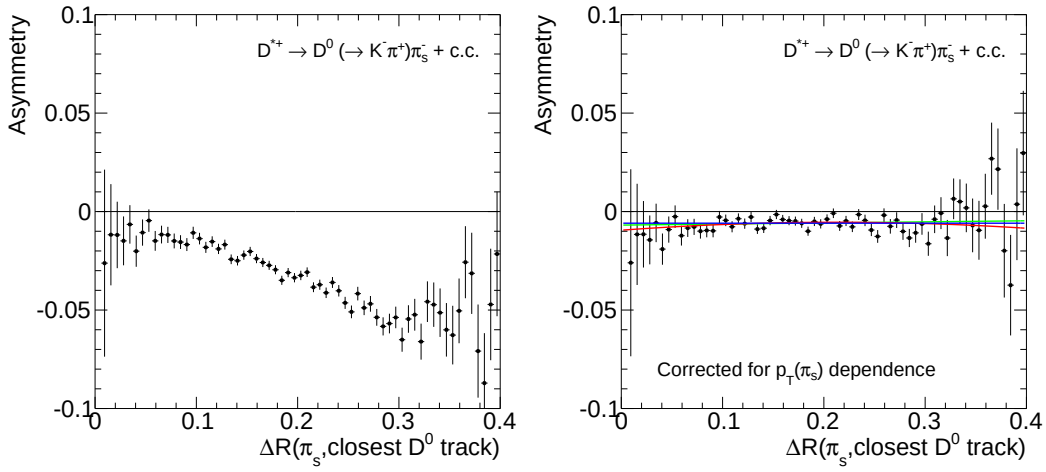

(a) (b)

Figure 6.1: *Raw $K\pi^*$ asymmetry as a function of the opening angle between the soft pion track and the closest D^0 track before (a) and after (b) the correction of the soft pion's p_T–dependent effect of Fig. 3.1. Figure (b) also shows the result of increasing order polynomial fits to the data points.*

6.1.1 Approximations in the suppression of instrumental effects

We check the reliability of the cancellation of all detector–induced asymmetries on simulated samples as described in Sect. 3.4. The analysis was repeated on several statistical ensembles in which we introduce known CP–violating asymmetries in the $D^0 \to h^+h^{(\prime)-}$ decays and instrumental effects (asymmetric reconstruction efficiency for positive and negative soft pions and kaons) dependent on a number of kinematic variables (*e. g.* transverse momentum). These studies constrain the size of residual instrumental effects that might not be fully cancelled by our method of linear subtraction of asymmetries of Eq. (3.8). Moreover, they also assess the impact of possible correlations between reconstruction efficiencies of D^0 decay–products and the soft pion, which have been assumed negligible in the analysis.

We further checked the latter assumption on data by searching for any variation of the observed asymmetry as a function of the proximity between the soft pion and the charm meson trajectories. In particular we studied the dependence of $A(K\pi^*)$ as a function of the opening angle, $\Delta R = \sqrt{\Delta\phi^2 + \Delta\eta^2}$, between the soft pion track and the closest D^0 track. In doing so it is important to notice that, due to kinematic

constraints, ΔR is strictly correlated to the soft pion transverse momentum, so we expect to observe some kind of dependence of the raw asymmetry from ΔR induced by the big p_T dependence, shown in Fig. 3.1, caused by the COT's super–layers layout. To disentangle this effect from a possible one due to non–factorization of reconstruction efficiencies we then reweight the $K\pi^\star$ sample in order to cancel such dependence. Fig. 6.1 shows $A(K\pi^*)$ versus ΔR before (a) and after such reweighting (b).

When the soft pion's p_T–dependent effect is corrected the raw asymmetry appears to be flat as a function of ΔR, as quantitatively confirmed by the result of increasing order polynomial fits: moving from a zero (blue curve), to first (green curve), to second (red curve) order polinomial the χ^2/ndf goes from 181/157, to 180/156, to 179/155. This proves that possible effects of non–factorizable efficiencies, if present, are completely negligible with respect to the statistical resolution of our final measurements.

We then assess a $\Delta\mathcal{A}_{\rm CP}(h^+h^-) = 0.009\%$ uncertainty, which corresponds to the maximum shift, increased by one standard deviation, observed in the result of our test with realistic values for the simulated effects and for true CP–violating asymmetries in input ranging from -5% to $+5\%$ (see Fig. 3.6).

6.1.2 Production asymmetries

Charm production in high–energy $p\bar{p}$ collisions is dominated by CP–conserving $c\bar{c}$ production through strong interaction. No production asymmetries are expected by integrating over the whole phase space. However, the CDF acceptance covers a limited region of the phase space, where CP conservation may not be exactly realized. Correlations with the $p\bar{p}$ initial state may induce pseudo–rapidity–dependent asymmetries between the number of produced charm and anticharm mesons. These asymmetries are constrained by CP conservation to change sign for opposite values of η. The net effect is then expected to vanish if the pseudo–rapidity distribution of the sample is symmetric.

As shown in Fig. 6.2 for a clean sample of $D^{*+} \to D^0(\to K^-\pi^+)\pi_s^+$ decays, our samples have only approximately symmetric η distributions with $\mathcal{O}(1\%)$ of forward—backward asymmetry. This could cause a non perfect cancellation of possible production asymmetries, which could potentially bias the measured $\mathcal{A}_{\rm CP}$'s.

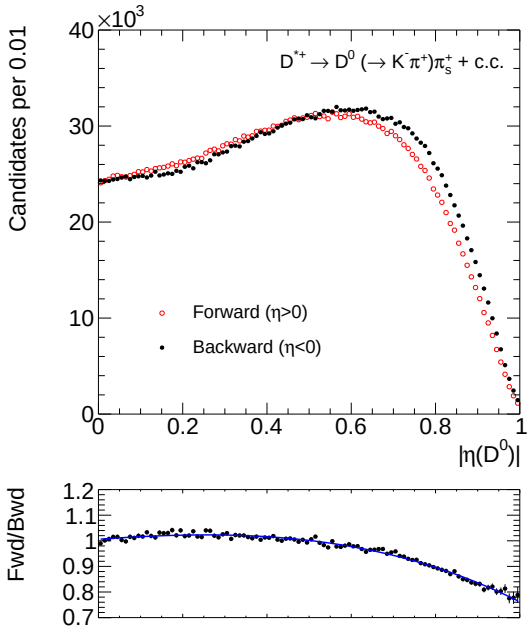

Figure 6.2: *Distributions of* $|\eta(D^0)|$ *for a clean sample of* $D^{*+} \to D^0(\to K^-\pi^+)\pi_s^+$ *decays for candidates in the forward (red empty points) and backward (black filled points). The bottom plot shows the ratio of forward over backward candidates, which is used to reweight the sample and enforce a perfect symmetry in the* η *distribution.*

To set an upper limit to the possible effect of the small η asymmetries observed in the samples used in this analysis, we repeated the fits enforcing a perfect η symmetry by reweighting. We observe variations of $\Delta\mathcal{A}_{\rm CP}(K^+K^-) = 0.03\%$ and $\Delta\mathcal{A}_{\rm CP}(\pi^+\pi^-) = 0.04\%$ between the fit results obtained with and without reweighting. Conservatively we take these small differences as an estimate of the size of possible residual effects. The cancellation of production asymmetries achieved in $p\bar{p}$ collisions (an initial CP–symmetric state) recorded with a polar–symmetric detector provide a significant advantage in high–precision CP violation measurements over experiments conducted in pp collisions.

6.1.3 Contamination of D mesons from B decays

A contamination of charm mesons produced in b–hadron decays could bias the results. Violation of CP symmetry in b–hadron decays may result in asymmetric production of charm and anticharm mesons. This may be large for a single exclusive

mode, but the effect is expected to vanish for inclusive $B \to DX$ decays [77]. However, we use the impact parameter distribution of D mesons to statistically separate primary and secondary mesons and assign a systematic uncertainty.

If f_B is the fraction of D mesons originating from B decays, the observed asymmetry is the linear combination of the observed asymmetry for primary D mesons and the one for secondary D mesons:

$$A = f_B A(D \text{ secondary}) + (1 - f_B) A(D \text{ primary}). \tag{6.1}$$

The asymmetry observed in secondary D mesons can be generated by CP violation in the b–hadron decay that produces the D meson and CP violation in the decay of the D meson itself. It is approximated as the sum of the physical CP violating asymmetry of b–hadrons averaged over inclusive $B \to DX$ decays, and the asymmetry one would observe if the D mesons were produced directly:

$$A(D \text{ secondary}) = \mathcal{A}_{\rm CP}(B \to DX) + A(D \text{ primary}). \tag{6.2}$$

Hence, combining Eq. (6.1) and Eq. (6.2), the asymmetry observed in each sample is given by

$$\begin{aligned} A(hh^{(\prime)*}) &= f_B(hh^{(\prime)*})\ \mathcal{A}_{\rm CP}(B \to DX) + A(hh^{(\prime)*} \text{ primary}) \\ A(K\pi) &= f_B(K\pi)\ \mathcal{A}_{\rm CP}(B \to DX) + A(K\pi \text{ primary}). \end{aligned}$$

Because the fraction of secondary D mesons is independent of their decay mode, we assume $f_B(hh^*) = f_B(K\pi^*)$. The contribution of CP violation in b–hadron decays may affect the final asymmetries as

$$\mathcal{A}_{\rm CP}(hh) = f_B \mathcal{A}_{\rm CP}(B \to DX) + \mathcal{A}_{\rm CP}(D^0 \to hh), \tag{6.3}$$

where f_B is estimated in the untagged $K^-\pi^+$ sample because the two terms arising from the tagged components cancel in the subtraction provided by Eq. (3.8).

In this analysis, the contamination from secondary D decays (see Fig. 4.1 (b)) is reduced by requiring the impact parameter of the D^0 candidate (IP) not to exceed $100\,\mu$m. The fraction f_B of residual D mesons originating from B decays has been determined by fitting the distribution of the impact parameter of untagged $D^0 \to K^-\pi^+$ decays selected within $\pm 24\,\text{MeV}/c^2$ of the known D^0 mass. We use two Gaussian distributions to model the narrow peak from primary D mesons and a

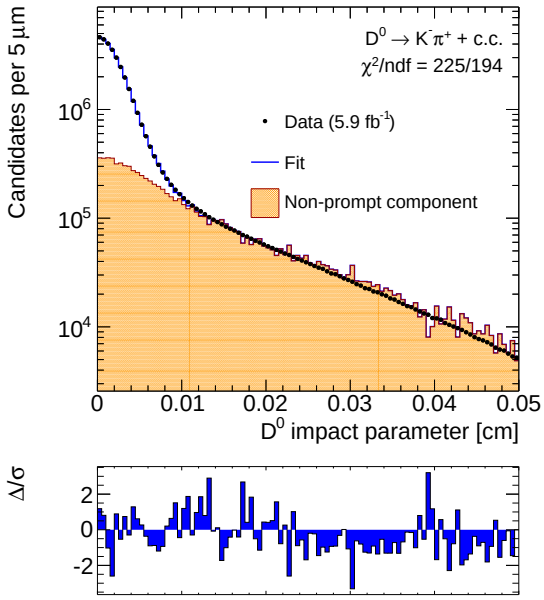

Figure 6.3: *Impact parameter distribution of D^0 candidates in the $D^0 \to K^-\pi^+$ signal region. Top plot with data and fit projections overlaid uses a logarithmic scale vertically. Bottom plot shows fractional difference between data and the fit on a linear scale.*

binned histogram, extracted from a simulated sample of inclusive $B \to DX$ decays, to model the secondary component. Fig. 6.3 shows the data with the fit projection overlaid. A residual contamination of 16.6% of $B \to DX$ decays is estimated.

To constrain the size of the effect from CP violation $\mathcal{A}_{\rm CP}(B \to DX)$ we repeated the analysis inverting the impact parameter selection. This selects a sample enriched in $D^0 \to K^-\pi^+$ decays coming from B decays. We reconstruct about 900 000 decays with an asymmetry, $A(K\pi) = (-0.647 \pm 0.172)\%$, consistent with the value of Eq. (5.5), used in our measurement. Figs. 6.4 (a)–(c) show the projections of the fit with the reversed impact parameter cut. The quality of the combined fit is not fully satisfactory, with data points up to more than 5σ away from the fit in the RS signal region, as a consequence of the poor modeling provided by the shapes extracted on the central sample. However, the raw asymmetry is well described as a function of the $K\pi$ mass, thus increasing our confidence in the reliability of the estimated $A(K\pi)$.

The expression for the observed asymmetry in this sample is written in Eq. (6.2).

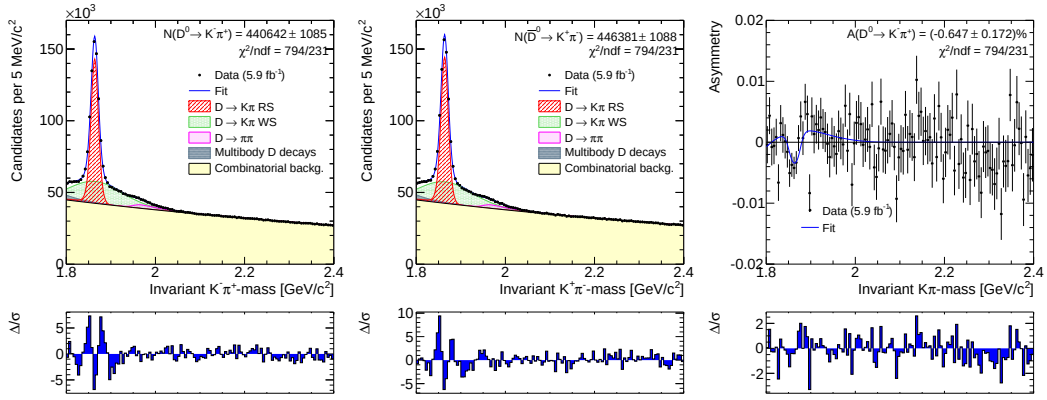

(a) (b) (c)

Figure 6.4: *Results of the combined fit of the untagged* $D^0 \to K^-\pi^+$ *sample with reversed impact parameter cut. Distribution of* $K^-\pi^+$ *mass for the odd sample (a),* $K^+\pi^-$ *mass for the even sample (b) and asymmetry as a function of the mass (c). Fit results are overlaid.*

The difference between the above asymmetry and the one observed in the central analysis (Eq. (6.3)) equals

$$\begin{aligned} A(\mathrm{IP} > 100\,\mu\mathrm{m}) - \mathrm{A}(\mathrm{IP} < 100\,\mu\mathrm{m}) &= (1 - f_B)\ \mathcal{A}_{\mathrm{CP}}(B \to DX) \\ &= (-0.18 \pm 0.17)\%. \end{aligned} \tag{6.4}$$

Using $f_B = 16.6\%$ we obtain $\mathcal{A}_{\mathrm{CP}}(B \to DX) = (-0.21 \pm 0.20)\%$ showing that no evidence for a bias induced by secondary D mesons is present. Since there is no evidence of CP asymmetry from non–promptly produced cham induced from B decays, one would be allowed to conclude that the systematic uncertainty due to this effect is negligible, could perform the measurement removing the cut on the D^0 impact parameter and reduce the statistical resolution, however, to be conservative, we assign a systematic uncertainty, based on Eq. (6.3), evaluated as

$$f_B\ \mathcal{A}_{\mathrm{CP}}(B \to DX) = \frac{f_B}{1 - f_B}\ \Delta = 0.034\%,$$

where f_B equals 16.6% and Δ corresponds to the 0.17%, *i. e.* one standard deviation of the difference in Eq. (6.4).

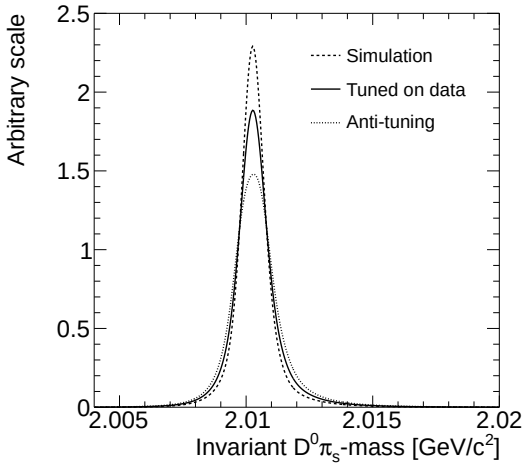

Figure 6.5: *Shape of $D^0\pi_s$ mass as extracted from simulation without tuning, with data tuning and with anti-data tuning.*

6.1.4 Assumptions in the fits of tagged samples

6.1.4.1 Shapes of fit functions

The mass shape extracted from simulation has been adjusted using data for a more accurate description of the observed signal shape. A systematic uncertainty is associated with the finite accuracy of this tuning and covers effect of possible mismodeling of the shapes of the fit components.

Fig. 6.5 shows a comparison between the shape extracted from the simulation and the templates used in the fit after the tuning. It also shows an additional template, named "anti–tuned" where the corrections that adjust the simulation to data have been inverted. If $f(m)$ is the template tuned on data, and $g(m)$ is the template extracted from the simulation, the anti–tuned template is constructed as $h(m) = 2f(m) - g(m)$. We repeated the measurement using the templates extracted from the simulation without any tuning, and those corresponding to the anti–tuning. The maximum variations from the central fit results, $\Delta\mathcal{A}_{\rm CP}(\pi^+\pi^-) = 0.009\%$ and $\Delta\mathcal{A}_{\rm CP}(K^+K^-) = 0.058\%$, are assigned as systematic uncertainties. The larger effect observed in the $D^0 \to K^+K^-$ case comes from the additional degrees of freedom introduced in the fit by the multibody decays component.

In addition, we performed a cross–check of the shape used for background of real D^0 mesons associated with random tracks. In the analysis, the shape parameters

Case	χ^2/ndf of the $K\pi^\star$ fit	$\Delta\mathcal{A}_{\rm CP}(\pi^+\pi^-)$ [%]	$\Delta\mathcal{A}_{\rm CP}(K^+K^-)$ [%]
δ_J, $b_{\rm bkg}$, $c_{\rm bkg}$ combined	414/306	0.019	0.012
δ_J, $b_{\rm bkg}$ combined, $c_{\rm bkg}$ free	397/305	0.072	0.018
δ_J, $c_{\rm bkg}$ combined, $b_{\rm bkg}$ free	401/305	0.048	0.018
δ_J combined, $b_{\rm bkg}$, $c_{\rm bkg}$ free	396/304	0.088	0.027
$b_{\rm bkg}$ combined, δ_J, $c_{\rm bkg}$ free	384/303	0.020	0.022
$c_{\rm bkg}$ combined, δ_J, $b_{\rm bkg}$ free	384/303	0.015	0.025
δ_J, $b_{\rm bkg}$, $c_{\rm bkg}$ free	383/302	0.012	0.012

Table 6.1: *Variation on the results with respect to the central fit with different input conditions to the tagged fits: combined (free) refers to the status of the corresponding shape parameter which in the fit is constrained to be the same (allowed to vary independently) between positive and negative samples.*

of $D^0 \to h^+h^-$ fits are constrained to the values obtained in the higher statistics tagged $D^0 \to K^-\pi^+$ sample. If the parameters are left floating in the fit, only a negligible variation on the final result ($< 0.003\%$) is observed.

6.1.4.2 Charge–dependent mass distributions

We observe small differences between distributions of $D^0\pi_s$ mass for positive and negative D^* candidates. These are ascribed to possible differences in tracking resolutions between low–momentum positive and negative particles. Such differences may impact our results at first order and would not be corrected by our subtraction method.

To determine a systematic uncertainty, we repeat the fit after separately constraining the signal shapes to be the same and leaving background shapes to vary independently for positive and negative D^* candidates, trying the combinations listed in Tab. 6.1. The values of the shape parameters in $D^0 \to h^+h^-$ fits are always fixed to the ones obtained from the $D^0 \to K^-\pi^+$ sample. The maximum variations with respect to the central fits are used as systematic uncertainties. They occur when both background shapes' parameters vary independently for positive and negative samples, while the parameter δ_J of the signal Johnson function is constrained to be the same. The maximum variations are $\Delta\mathcal{A}_{\rm CP}(\pi^+\pi^-) = 0.088\%$ and $\Delta\mathcal{A}_{\rm CP}(K^+K^-) = 0.027\%$.

6.1.4.3 Asymmetries from residual backgrounds

A further source of systematic uncertainty is the approximation used in the subtraction of physics backgrounds in some of the tagged samples.

Using simulation we estimate that a 0.77% contamination from physics backgrounds enters the $\pm 24\,\mathrm{MeV}/c^2$ $K^-\pi^+$ signal range, dominated by the tail from partially reconstructed multibody D^0 decays (as shown in Figs. 4.6 (c) and (e)). This component is included in the fit of the KK^* sample, which provides an estimate of the asymmetry of this contamination (Eq. (5.4)), but is neglected in the fit of the $K\pi^*$ sample. The product of the contaminating fraction times the additional asymmetry of the contaminant determines a common systematic uncertainty that affects both the $\mathcal{A}_{\mathrm{CP}}(K^-K^+)$ and $\mathcal{A}_{\mathrm{CP}}(\pi^+\pi^-)$, since $A(K\pi^*)$ enters the determination of both results. This is the only component that impacts the systematic uncertainty of the $D^0 \to K^+K^-$ result. Indeed, in the fit to the $D^0\pi_s$ mass that determines the raw K^+K^- asymmetry, we fitt any residual physics background contribution, absorbing the effect of any further background asymmetry in the statistical uncertainty. An additional systematic contribution affects the $D^0 \to \pi^+\pi^-$ result. In the fits to the $D^0\pi_s$ mass for the determination of the raw $\pi^+\pi^-$ asymmetry we assume the residual backgrounds to be negligible. Using simulation we estimate that a 0.22% contamination from physics backgrounds enters the $\pm 24\,\mathrm{MeV}/c^2$ $\pi^+\pi^-$ signal range, dominated by the tail of the $D^0 \to K^-\pi^+$ signal (as shown in Figs. 4.6 (a) and (d)). The asymmetry of this contamination is determined from the fit of the $K\pi^*$ sample (Eq. (5.3)). Again, the associated systematic uncertainty is the product of the contaminating fraction times the additional asymmetry of the contaminant.

In summary, neglecting residual backgrounds in the $K\pi^*$ and $\pi\pi^*$ fits yields a maximum effect of 0.005% on the measured asymmetries for both $D^0 \to \pi^+\pi^-$ and $D^0 \to K^+K^-$.

6.1.5 Assumptions in the fits of untagged samples

6.1.5.1 Shapes of fit functions

We follow the same strategy used for the tagged case to assign the systematic uncertainty associated with possible mis–modeling of the shapes in fits of the untagged sample.

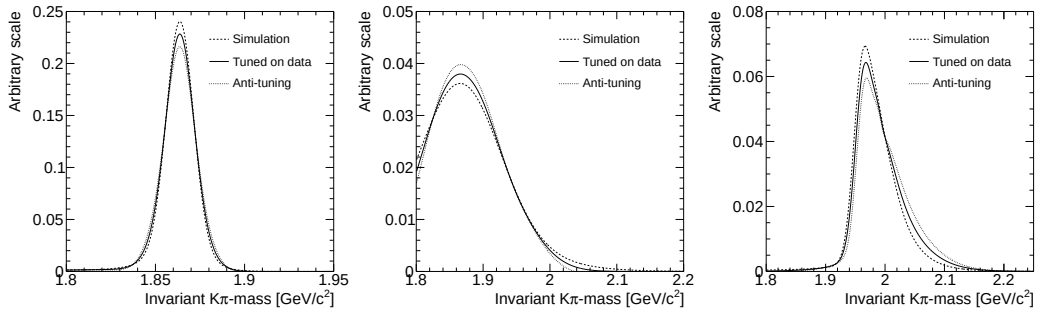

(a) (b) (c)

Figure 6.6: *Shapes of $K^{\pm}\pi^{\mp}$ mass from simulation without tuning, with data tuning, and with anti-data tuning for RS (a) and WS (b) $K^{\pm}\pi^{\mp}$ decays, and for $\pi^{+}\pi^{-}$ decays (c).*

Fig. 6.6 shows the comparison between templates extracted from the simulation without any tuning, those tuned to data (and used in the central fit), and the anti–tuned ones. We repeated the fit using these alternative templates; the maximum variation from the central fit, $\Delta A(K\pi) = 0.005\%$, is used as the systematic uncertainty.

6.1.5.2 Charge–dependent mass distributions

Since in the untagged case we reconstruct a neutral final state, we expect the mass shapes of all components to be the same for charm (odd) and anticharm (even) samples. However, we repeated the simultaneous fit under different assumptions to assign the systematic uncertainty associated with possible residual differences which may be induced by the artificial swap of the mass assignment of one sample with respect to the other. The parameters of the Gaussian distributions used to model the bulk of the mass distributions were left free to vary independently for the odd and even samples, and separately for the RS, WS and $D^0 \to \pi^+\pi^-$ components. We assume no difference between mass distributions of combinatorial background and neglect any possible effect in the small fraction of partially reconstructed decays, which is present above $1.8\,\mathrm{GeV}/c^2$.

The differences between estimated shape parameters in odd and even samples do not exceed 3σ, showing compatibility between the shapes. A systematic uncertainty of 0.044% is obtained by summing in quadrature the shifts from the central value

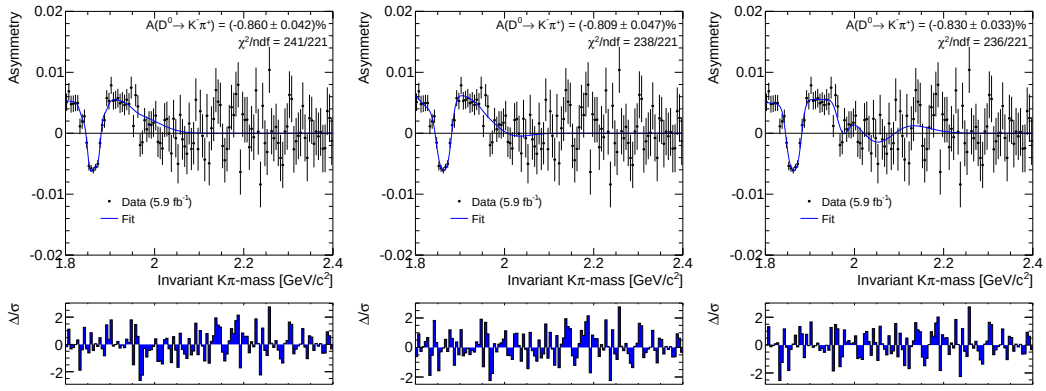

(a) (b) (c)

Figure 6.7: *Projections on the asymmetry as a function of the invariant $K\pi$–mass for indipendent variations of RS (a), WS (b) and $D \to \pi\pi$ (c) shapes in odd and even samples.*

of the estimated asymmetries in the three different cases (see Fig. 6.7).

6.1.5.3 Asymmetries from residual physics backgrounds

In the measurement of the asymmetry of Cabibbo–favored $D^0 \to K^-\pi^+$ decays, we neglected the contribution from the small, but irreducible, component of doubly–Cabibbo–suppressed (DCS) $D^0 \to K^+\pi^-$ decays. Large CP violation in DCS decays may bias the charge asymmetry we attribute to $D^0 \to K^-\pi^+$ decays. To consider this possibility, we assign a systematic uncertainty corresponding to

$$f_{\rm DCS}\ \mathcal{A}_{\rm CP}(D^0 \to K^+\pi^-) = f_{\rm DCS}\ \Delta = 0.013\%,$$

where $f_{\rm DCS} = 0.39\%$ is the known [7] fraction of DCS decays with respect to Cabibbo–favored decays and $\Delta = 2.2\%$ corresponds to one standard deviation of the current measured limit on the CP violating asymmetry $\mathcal{A}_{\rm CP}(D^0 \to K^+\pi^-)$, as reported in Ref. [7].

In the central fit for the untagged $D^0 \to K^-\pi^+$ sample, no asymmetry in $D^0 \to \pi^+\pi^-$ decays or combinatorial background is allowed, as expected by the way the untagged sample is defined. We confirmed the validity of this choice by fitting the asymmetry with independent yields for these two components in the charm and anticharm samples. The fitted asymmetries are compatible with zero within

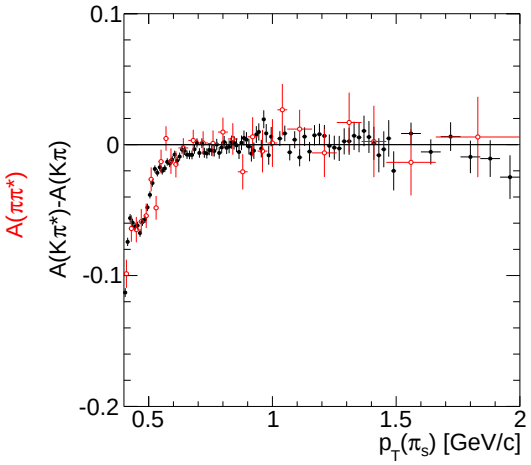

Figure 6.8: *Comparison between* $A(\pi\pi^*)$ *(open red points) and* $A(K\pi^*) - A(K\pi)$ *(closed black points) as a function of the soft pion's tranverse momentum.*

uncertainties and the result corresponds to a $\Delta A(K\pi) = 0.011\%$ variation from the central fit; we ascribe such a variation to statistical fluctuations and we do not consider this an additional contribution to the systematic error.

6.1.6 Limitations of kinematic reweighting

The tagged event samples were reweighted after subtracting the background, sampled in signal mass sidebands. We constrained the size of possible residual systematic uncertainties by repeating the fit of tagged $D^0 \to h^+h^-$ after a reweighting without any sideband subtraction. The variation in observed asymmetries was found to be negligible with respect to other systematic uncertainties.

In reweighting the untagged sample we did not subtract the background. The signal distributions have been extracted by selecting a mass region corresponding approximately to a cross–shaped window of $\pm 3\sigma$ in the two–dimensional space $(m_{K^-\pi^+}, m_{K^+\pi^-})$ of Fig. 4.3. To assign a systematic uncertainty we extracted the signal distributions and reweighted the data using a smaller cross-shaped region of $\pm 2\sigma$, *i. e.* within $16\,\mathrm{MeV}/c^2$ of the nominal D^0 mass. The background contamination decreases from 6% to 4%. We repeated the analysis and found $A(K\pi) = (-0.831 \pm 0.033)\%$ corresponding to a variation from the central fit of $< 0.001\%$, thus negligible with respect to other systematic uncertainties.

The negligible impact of the kinematic reweight on our measurement is somewhat expected: the reweighting procedure is formally necessary in the analysis method to cancel any possible difference between detector–induced asymmetries which have a dependence on the kinematical features of the specific decays sample. These are intrinsically small because of all $D^0 \to h^+h^{(\prime)-}$ decays (tagged and untagged) have been selected with exactly the same requirements (both at on–line and off–line level) and have very similar decay topologies. As an example, we shown, in Fig. 6.8, the observed asymmetry, as a function of $p_T(\pi_s)$, in the $\pi\pi^*$ sample in comparison to the combination of observed asymmetries in the Cabibbo–favored tagged and untagged $D^0 \to K^-\pi^+$ decays, $A(K\pi^*) - A(K\pi)$, when no equalization of soft pion's distributions has been performed; the compatibility between the two histograms graphically proves that the kinematic reweight has a negligible effect on the effectiveness of the p_T–dependent correction of the soft pion's charge asymmetry for the the determination of $\mathcal{A}_{\rm CP}(\pi^+\pi^-)$.

6.2 Total systematic uncertainty

Tab. 6.2 summarizes the systematic uncertainties considered in the measurement. Assuming them independent and summing in quadrature, we obtain a total systematic uncertainty of 0.11% on the observed CP violating asymmetry of $D^0 \to \pi^+\pi^-$ decays and 0.09% in $D^0 \to K^+K^-$ decays. Their sizes are approximately half of the statistical uncertainties.

Source	$\Delta\mathcal{A}_{\rm CP}(\pi^+\pi^-)$ [%]	$\Delta\mathcal{A}_{\rm CP}(K^+K^-)$ [%]
Approximations in the suppression		
of detector effects	0.009	0.009
Production asymmetries	0.040	0.030
Contamination of secondary D mesons	0.034	0.034
Shapes assumed in fits	0.010	0.058
	$(0.009 \oplus 0.005)$	$(0.058 \oplus 0.005)$
Charge-dependent mass distributions	0.098	0.052
	$(0.088 \oplus 0.044)$	$(0.027 \oplus 0.044)$
Asymmetries from residual backgrounds	0.014	0.014
	$(0.005 \oplus 0.013)$	$(0.005 \oplus 0.013)$
Total	0.113	0.092

Table 6.2: *Summary of systematic uncertainties. The uncertainties reported for the last three sources result from the sum in quadrature of the contributions in the tagged and untagged fits shown in parethesis.*

Chapter 7

Final Results

This chapter presents the final results of the measurement described in this thesis and a comparison with other existing measurements.

7.1 Time–integrated asymmetries in $D^0 \to \pi^+\pi^-$ and $D^0 \to K^+K^-$ decays

We measure the time–integrated CP–violating asymmetries in $D^0 \to \pi^+\pi^-$ and $D^0 \to K^+K^-$ decays to be

$$\mathcal{A}_{\rm CP}(D^0 \to \pi^+\pi^-) = \big(+0.22 \pm 0.24\ (stat.) \pm 0.11\ (syst.)\big)\%, \tag{7.1}$$

$$\mathcal{A}_{\rm CP}(D^0 \to K^+K^-) = \big(-0.24 \pm 0.22\ (stat.) \pm 0.09\ (syst.)\big)\%, \tag{7.2}$$

in agreement with CP conservation in the time–evolution of these decays. These are the most precise determinations of these quantities to date, and significantly improve on previous world average.

7.1.1 Direct and indirect CP violation

A useful comparison with results from other experiments is achieved by approximating the observed asymmetry with a linear combination (Eq. (1.25)) of a direct component, $\mathcal{A}_{\rm CP}^{\rm dir}$, and an indirect component, $\mathcal{A}_{\rm CP}^{\rm ind}$, through a coefficient that is the mean proper decay time of charm mesons in the data sample. The direct component corresponds to a difference in width between charm and anticharm decays into the same final state. The indirect component is due to the probability for a charm meson to oscillate into an anticharm one being different from the probability for an anticharm meson to oscillate into a charm one (CP violation in mixing) and to the possibility of having CP violation in the interference between mixing and decay.

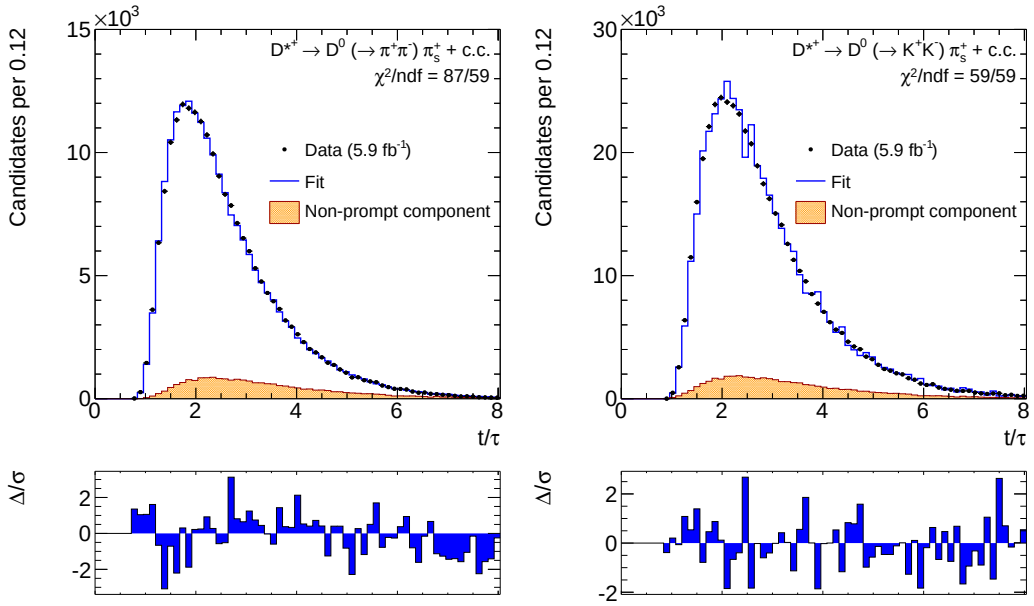

(a) (b)

Figure 7.1: *Distribution of proper decay time (in units of D^0 lifetime) for sideband–subtracted tagged $D^0 \to \pi^+\pi^-$ (a) and $D^0 \to K^+K^-$ (b) data. Fit results are overlaid including the component from secondary charmed mesons (orange).*

The decay time of each D^0 meson, t, is determined as

$$t = \frac{L_{xy}}{c\,(\beta\gamma)_T} = L_{xy}\,\frac{m_{D^0}}{c\;p_T}, \tag{7.3}$$

where $(\beta\gamma)_T = p_T/m_{D^0}$ is the transverse Lorentz factor. This is an unbiased estimate of the actual decay time only for primary charmed mesons. For secondary charm, the decay time of the parent B meson should be subtracted. The mean decay times of our signals are determined from a fit to the proper decay time distribution of sideband–subtracted tagged decays (see Fig. 7.1). The fit includes components for primary and secondary D mesons, whose shapes are modeled from simulation. Simulation is used to extract the information on the mean decay time of secondary charmed decays, using the known true decay time. The proportions between primary and secondary are also determined from the fit and are consistent with results of the fit to the D^0 impact parameter in data (analogous to the one described in Sect. 6.1.3). We determine a mean decay time of 2.40 ± 0.03 and 2.65 ± 0.03, in units of D^0 lifetime, for $D^0 \to \pi^+\pi^-$ and $D^0 \to K^+K^-$ decays, respectively. The quoted uncertainty is the sum in quadrature of statistical and systematic contribu-

tions. The small difference in the two samples is caused by the slightly different kinematics of the two decays, which impacts their trigger acceptances.

Each of our measurements defines a band in the respective $(\mathcal{A}_{\rm CP}^{\rm ind}, \mathcal{A}_{\rm CP}^{\rm dir})$ plane with slope $-\langle t \rangle / \tau$ (see Eq. (1.25)). Similar bands can be drawn for *BABAR* and Belle measurements, with slope -1 [54, 55], due to unbiased acceptance in decay time. They are shown in Fig. 7.2, which displays their relationship. The bands represent $\pm 1\sigma$ uncertainties and show that all measurements are compatible with CP conservation (the point at the origin in the two–dimensional plane).

The results of the three experiments can be easily combined under the assumption of Gaussian uncertainties. We construct combined confidence regions in the $(\mathcal{A}_{\rm CP}^{\rm ind}, \mathcal{A}_{\rm CP}^{\rm dir})$ plane, denoted with 68% and 95% confidence level ellipses. The corresponding averaged values for the asymmetries are

$$\mathcal{A}_{\rm CP}^{\rm dir}(D^0 \to \pi^+\pi^-) = (0.04 \pm 0.69)\%, \qquad \mathcal{A}_{\rm CP}^{\rm ind}(D^0 \to \pi^+\pi^-) = (0.08 \pm 0.34)\%,$$
$$\mathcal{A}_{\rm CP}^{\rm dir}(D^0 \to K^+K^-) = (-0.24 \pm 0.41)\%, \qquad \mathcal{A}_{\rm CP}^{\rm ind}(D^0 \to K^+K^-) = (0.00 \pm 0.20)\%,$$

in which the uncertainties represent one–dimensional 68% confidence level intervals.

Assuming negligible direct CP violation in both decay modes, the observed asymmetry is only due to mixing, $\mathcal{A}_{\rm CP}(h^+h^-) \approx \mathcal{A}_{\rm CP}^{\rm ind}\ \langle t \rangle / \tau$, yielding

$$\mathcal{A}_{\rm CP}^{\rm ind}(D^0 \to \pi^+\pi^-) = \big(+0.09 \pm 0.10\ (stat.) \pm 0.05\ (syst.)\big)\%,$$
$$\mathcal{A}_{\rm CP}^{\rm ind}(D^0 \to K^+K^-) = \big(-0.09 \pm 0.08\ (stat.) \pm 0.03\ (syst.)\big)\%.$$

As already stated in Sect. 1.4.1, assuming that no large beyond–Standard Model weak phases appear in the decay amplitudes, $\mathcal{A}_{\rm CP}^{\rm ind}$ is independent of the final state. Therefore the two measurements can be averaged, assuming correlated systematic uncertainties, to obtain a precise determination of CP violation in charm mixing:

$$\mathcal{A}_{\rm CP}^{\rm ind}(D^0) = \big(-0.01 \pm 0.06\ (stat.) \pm 0.04\ (syst.)\big)\%.$$

This corresponds to the following upper limits on CP violation in charm mixing:

$$|\mathcal{A}_{\rm CP}^{\rm ind}(D^0)| < 0.13\ (0.16)\% \text{ at the } 90\ (95)\% \text{ CL}.$$

The enrichment in longer–lived decays in the CDF sample offers a significant advantage over B–factories in sensitivity on the time–dependent component, as shown in Figs. 7.3 (a) and (c).

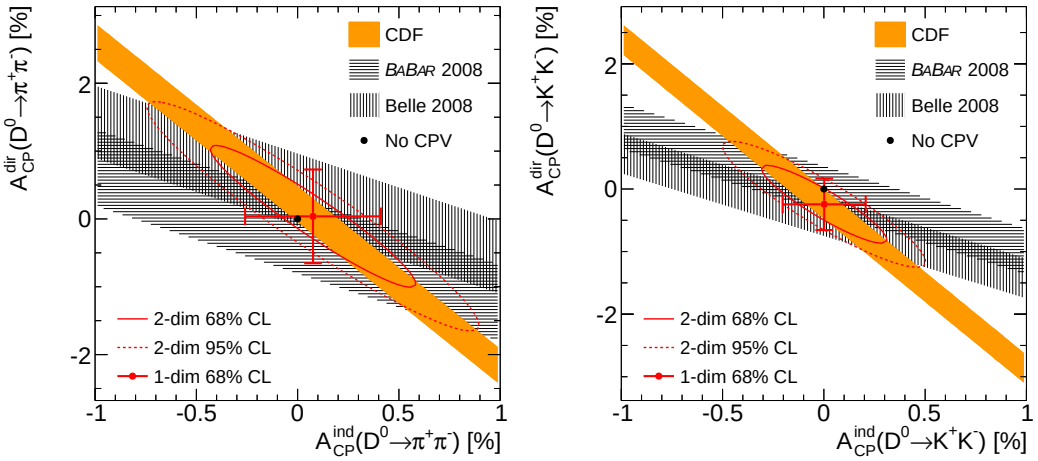

(a) (b)

Figure 7.2: *Comparison of the present results with Belle and BABAR measurements of time-integrated CP-violating asymmetry in* $D^0 \to \pi^+\pi^-$ *(a) and* $D^0 \to K^+K^-$ *(b) decays displayed in the* $(\mathcal{A}_{CP}^{ind}, \mathcal{A}_{CP}^{dir})$ *plane. The point with error bars denotes the central value of the combination of the three measurements with one-dimensional 68% confidence level uncertainties.*

Conversely, assuming that CP symmetry is conserved in charm mixing, our results are readily comparable to measurements obtained at B–factories. As shown in Figs. 7.3 (b) and (d), again this result is the world's most precise.

7.1.2 Difference of asymmetries

A useful comparison with theory predictions is achieved by calculating the difference between the asymmetries observed in the $D^0 \to K^+K^-$ and $D^0 \to \pi^+\pi^-$ decays, $\Delta\mathcal{A}_{\rm CP}$. Since the difference in decay–time acceptance is small, $\Delta\langle t\rangle/\tau = 0.26\pm0.01$, when assuming that no large CP–violating phases from New Physics contributions enter the decay amplitudes (the indirect asymmetry is universal), most of the indirect CP–violating asymmetry cancels in the subtraction. Hence $\Delta\mathcal{A}_{\rm CP}$ approximates the difference in direct CP–violating asymmetries of the two decays.

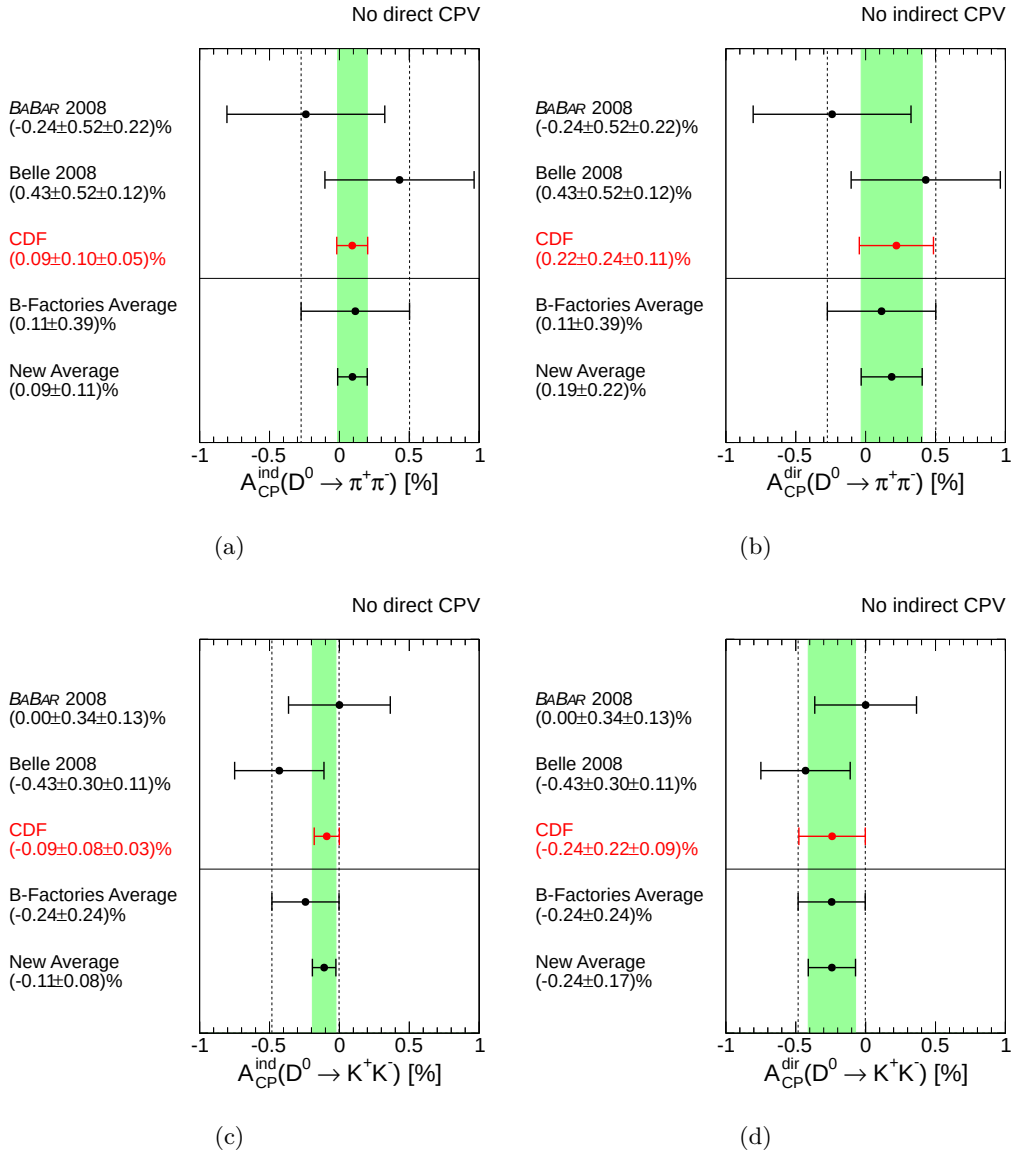

Figure 7.3: *Comparison of the present results with results from Belle and* BABAR *assuming no direct, (a) and (c), or indirect, (b) and (d), CP violation. In each plot the* 1σ *band of the B-factories' average is displayed in blue, while the new average that includes the CDF result is shown in green.*

Using the observed asymmetries from Eqs. (5.1) and (5.2), we determine

$$\begin{aligned}\Delta\mathcal{A}_{\rm CP} &= \mathcal{A}_{\rm CP}(K^+K^-) - \mathcal{A}_{\rm CP}(\pi^+\pi^-) = A(KK^*) - A(\pi\pi^*) \\ &= \Delta\mathcal{A}_{\rm CP}^{\rm dir} + \frac{\Delta\langle t\rangle}{\tau}\,\mathcal{A}_{\rm CP}^{\rm ind}(D^0) \\ &= \left(-0.46 \pm 0.31\ (stat.) \pm 0.12\ (syst.)\right)\%.\end{aligned}$$

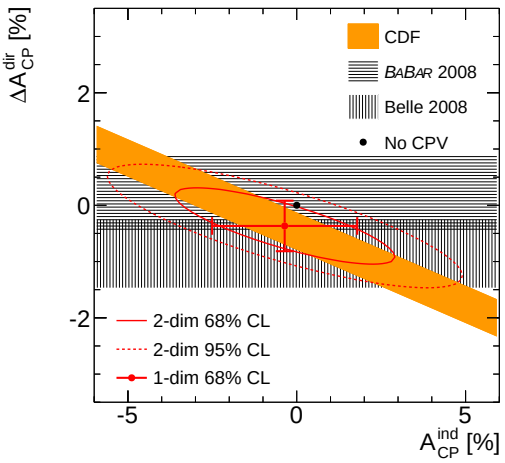

Figure 7.4: *Difference between direct CP–violating asymmetries in the K^+K^- and $\pi^+\pi^-$ final states as a function of the indirect asymmetry. Belle and BABAR measurements are also reported for comparison. The point with error bars denotes the central value of the combination of the three measurements with one–dimensional 68% confidence level uncertainties.*

The systematic uncertainty is dominated by the 0.12% uncertainty from the shapes assumed in the mass fits, and their possible dependence on the charge of the D^* meson. This is determined by combining the difference of shifts observed in Sects. 6.1.4.1 and 6.1.4.2 including correlations: $(0.058 - 0.009)\% = 0.049\%$ and $(-0.027 - 0.088)\% = 0.115\%$. Smaller contributions include a 0.009% from the finite precision associated to the suppression of detector–induced effects (see Sect. 6.1.1), and a 0.005% due to the 0.22% background we ignore under the $D^0 \to \pi^+\pi^-$ signal (see Sect. 6.1.4.3). The effects of production asymmetries and contamination from secondary charm decays cancel in the difference.

We see no evidence of a difference in CP violation between $D^0 \to K^+K^-$ and $D^0 \to \pi^+\pi^-$ decays. Fig. 7.4 shows the difference in direct asymmetries, $\Delta\mathcal{A}_{CP}^{dir}$, as a function of the indirect asymmetry compared with experimental results from BABAR and Belle [42, 43]. The bands represent $\pm 1\sigma$ uncertainties. The measurements, combined assuming Gaussian uncertainties, provide 68% and 95% confidence level regions in the $(\Delta\mathcal{A}_{CP}^{dir}, \mathcal{A}_{CP}^{ind})$ plane, denoted with ellipses. The corresponding values for the asymmetries are $\Delta\mathcal{A}_{CP}^{dir} = (-0.37 \pm 0.45)\%$ and $\mathcal{A}_{CP}^{ind} = (-0.35 \pm 2.15)\%$.

This thesis represents a pioneering measurement of high precision charm CP

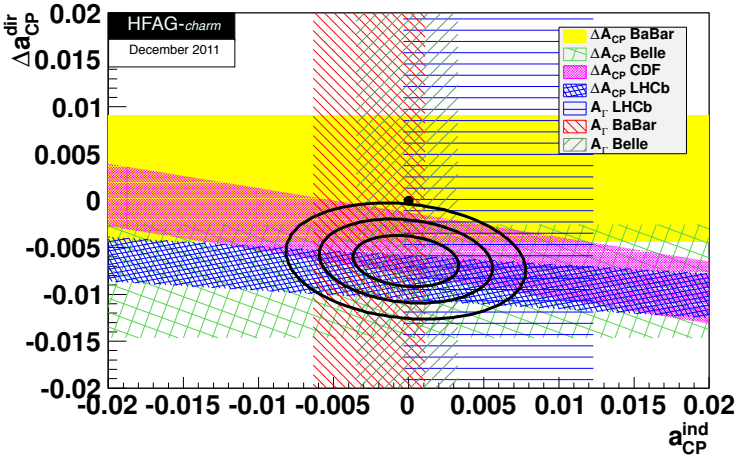

Figure 7.5: *Combination of all available measurements of CP violation in singly–Cabibbo–suppressed two–body D^0 decays as performed by the HFAG [41]. The bands represent $\pm 1\sigma$ intervals and the two–dimensional 68%, 95% and 99.7% CL regions, plotted as ellipses, are obtained assuming Gaussian and uncorrelated uncertainties.*

violation at hadron colliders that has been continued by LHCb, which recently reported a more precise measurement of the difference of the time–integrated CP asymmetries in $D^0 \to K^-K^+$ and $D^0 \to \pi^-\pi^+$ decays using $0.62\,\text{fb}^{-1}$ of the data collected in 2011 [78]. The choice of measuring only the difference, $\Delta\mathcal{A}_{\rm CP}(h^+h^-)$, instead of the two single asymmetries, is necessary at the LHC in order to cancel with enough precision the unknown bias induced by the CP–asymmetric pp initial state, which does not ensures a charge–symmetric production of charmed mesons in the collision. With a sample corresponding to approximately twice (three times) more $D^0 \to \pi^+\pi^-$ ($D^0 \to K^+K^-$) events than the ones used in this thesis, LHCb finds $\Delta\mathcal{A}_{\rm CP}(h^+h^-) = (-0.82 \pm 0.21\ (stat.) \pm 0.11\ (syst.))\%$, corresponding to a 3.5σ deviation from zero, thus claiming the first evidence of CP violation in the charm sector.

HFAG performed a combination of all the available measurements of CP violation in $D^0 \to h^+h^-$ decays in the plane $(\mathcal{A}_{\rm CP}^{\rm ind}, \Delta\mathcal{A}_{\rm CP}^{\rm dir})$, as shown in Fig. 7.5 [41]. The data is consistent with no CP violation with a P–value of 0.128%; the central values for the individual parameters are: $\mathcal{A}_{\rm CP}^{\rm ind}(D^0) = (-0.02 \pm 0.23)\%$ and $\Delta\mathcal{A}_{\rm CP}^{\rm dir}(h^+h^-) = (-0.65 \pm 0.18)\%$. The comparison of these numbers with the ones obtained in this thesis clearly shows that our measurements still give an important contribution to the world average.

Conclusions

In summary, this thesis reports the results of the most precise measurement of CP violation in singly–Cabibbo–suppressed $D^0 \to \pi^+\pi^-$ and $D^0 \to K^+K^-$ decays to date. Within the CDF II detector, we reconstruct signals of $\mathcal{O}(10^5)$ decays in an event sample of $p\bar{p}$ collision data corresponding to approximately $5.9\,\mathrm{fb}^{-1}$ of integrated luminosity collected by a trigger on displaced tracks. A new fully data–driven method to cancel instrumental effects has been developed for this measurement and provides effective suppression of systematic uncertainties to the 0.1% level, approximately half the magnitude of the statistical ones.

We find no evidence of CP violation and measure

$$\mathcal{A}_{\mathrm{CP}}(D^0 \to \pi^+\pi^-) = (+0.22 \pm 0.24\ (\mathit{stat.}) \pm 0.11\ (\mathit{syst.}))\% \quad \text{and}$$
$$\mathcal{A}_{\mathrm{CP}}(D^0 \to K^+K^-) = (-0.24 \pm 0.22\ (\mathit{stat.}) \pm 0.09\ (\mathit{syst.}))\%.$$

These are the most precise determinations from a single experiment to date and supersede the corresponding results of Ref. [56].

Assuming negligible direct CP violation in $D^0 \to \pi^+\pi^-$ and $D^0 \to K^+K^-$ decays, the above results, combined with the high–valued average proper decay time of the charmed mesons in our sample with respect to the B–facotries ones, provide a stringent general constraint on CP violation in $D^0 - \overline{D}^0$ mixing, $|\mathcal{A}_{\mathrm{CP}}^{\mathrm{ind}}(D^0)| < 0.13\%$ at the 90% CL, which probes significant regions of the parameter space of charm phenomenology where discrimination between Standard Model and New Physics dynamics becomes possible [79, 80].

The results presented in this thesis have been published by *Physical Review D* in January 2012 [1].

Appendix A

Observed Asymmetries in the $D^0 \to K^-\pi^+$ Samples

In this appendix, with a procedure similar to the one presented in Sect. 3.3 for the D^*–tagged $D^0 \to h^+h^-$ case, we outline the mathematical derivation of the observed asymmetries of Eqs. (3.4) and (3.5).

A.1 D^*–tagged $D^0 \to K^-\pi^+$

Assuming factorization of efficiencies for reconstructing the neutral charmed meson and the soft pion, the number of observed D^*–tagged $\overline{(}D\overline{)}^0 \to K^\mp\pi^\pm$ is

$$N^{\rm obs}_{\overline{(}D\overline{)}^0} = \frac{N_{D^*}}{2}\ \mathcal{B}(D^* \to D^0\pi)\ \mathcal{B}(\overline{(}D\overline{)}^0 \to K^\mp\pi^\pm) \int d\boldsymbol{p}_* d\boldsymbol{p}_s d\boldsymbol{p}_K d\boldsymbol{p}_\pi\ \varrho_{*\pm}(\boldsymbol{p}_*)\ \varrho_{K\pi^*}(\boldsymbol{p}_K, \boldsymbol{p}_\pi, \boldsymbol{p}_s \,|\, \boldsymbol{p}_*)\ \varepsilon_{K^\mp\pi^\pm}(\boldsymbol{p}_K, \boldsymbol{p}_\pi)\ \varepsilon_{s\pm}(\boldsymbol{p}_s),$$

where N_{D^*} is the total number of D^{*+} and D^{*-} mesons produced; $\mathcal{B}(D^* \to D^0\pi)$ and $\mathcal{B}(\overline{(}D\overline{)}^0 \to K^\mp\pi^\pm)$ are the branching fractions of $D^{*\pm} \to \overline{(}D\overline{)}^0\pi^\pm$, assumed to be charge symmetric, and $\overline{(}D\overline{)}^0 \to K^\mp\pi^\pm$ respectively; $\boldsymbol{p}_*$, $\boldsymbol{p}_s$, $\boldsymbol{p}_\pi$ and $\boldsymbol{p}_K$ are the three–momenta of the D^*, π_s, pion and kaon respectively; $\varrho_{*\pm}$ is the densities in phase space of $D^{*\pm}$ mesons; $\varrho_{K\pi^*}$ is the density in phase space of the soft pion and the $K^\mp\pi^\pm$ pair from D^0 decay; $\varepsilon_{K^\mp\pi^\pm}$ is the detection efficiency of the $K^\mp\pi^\pm$ pair from the $\overline{(}D\overline{)}^0$ decay and $\varepsilon_{s\pm}$ is the detection efficiencies of the positive/negative soft pion. Densities are normalized, as usual, to unity.

The difference between charm and anticharm event yields is therefore

$$\begin{aligned} N^{\rm obs}_{D^0} - N^{\rm obs}_{\overline{D}^0} = N_{D^*}\ \mathcal{B}(D^* \to D^0\pi)\ \overline{\mathcal{B}}(D^0 \to K\pi) \int & d\boldsymbol{p}_* d\boldsymbol{p}_s d\boldsymbol{p}_K d\boldsymbol{p}_\pi \\ & \varrho_*(\boldsymbol{p}_*)\ \varrho_{K\pi^*}(\boldsymbol{p}_K, \boldsymbol{p}_\pi, \boldsymbol{p}_s \,|\, \boldsymbol{p}_*)\ \varepsilon_{K^\mp\pi^\pm}(\boldsymbol{p}_K, \boldsymbol{p}_\pi)\ \varepsilon_s(\boldsymbol{p}_s) \\ & \Big\{ \big[1 + \delta\varrho_*(\boldsymbol{p}_*)\big](1 + \mathcal{A}_{\rm CP})\big[1 + \delta\varepsilon_{K\pi}(\boldsymbol{p}_K, \boldsymbol{p}_\pi)\big]\big[1 + \delta\varepsilon_s(\boldsymbol{p}_s)\big] \\ & \quad - \big[1 - \delta\varrho_*(\boldsymbol{p}_*)\big](1 - \mathcal{A}_{\rm CP})\big[1 - \delta\varepsilon_{K\pi}(\boldsymbol{p}_K, \boldsymbol{p}_\pi)\big]\big[1 - \delta\varepsilon_s(\boldsymbol{p}_s)\big] \Big\} \end{aligned}$$

where we introduced the time–integrated $\mathcal{A}_{\rm CP} = \mathcal{A}_{\rm CP}(D^0 \to K^-\pi^+)$ and we have defined the following additional quantities:

$$\overline{\mathcal{B}}(D^0 \to K\pi) = \frac{\mathcal{B}(D^0 \to K^-\pi^+) + \mathcal{B}(\overline{D}^0 \to K^+\pi^-)}{2},$$

$$\begin{aligned} \varrho_* &= \frac{\varrho_{*+} + \varrho_{*-}}{2}, & \delta\varrho_* &= \frac{\varrho_{*+} - \varrho_{*-}}{\varrho_{*+} + \varrho_{*-}}, \\ \varepsilon_s &= \frac{\varepsilon_{s+} + \varepsilon_{s-}}{2}, & \delta\varepsilon_s &= \frac{\varepsilon_{s+} - \varepsilon_{s-}}{\varepsilon_{s+} + \varepsilon_{s-}}, \\ \varepsilon_{K\pi} &= \frac{\varepsilon_{K^-\pi^+} + \varepsilon_{K^+\pi^-}}{2}, & \delta\varepsilon_{K\pi} &= \frac{\varepsilon_{K^-\pi^+} - \varepsilon_{K^+\pi^-}}{\varepsilon_{K^-\pi^+} + \varepsilon_{K^+\pi^-}}. \end{aligned}$$

Expanding the products and observing that all terms in $\delta\varrho_*(\boldsymbol{p}_*)$ vanish upon integration over a symmetric $\boldsymbol{p}_*$ domain, we obtain

$$\begin{aligned} N^{\rm obs}_{D^0} - N^{\rm obs}_{\overline{D}^0} = N_{D^*}\ \mathcal{B}(D^* \to D^0\pi)\ \overline{\mathcal{B}}(D^0 \to K\pi) \int & d\boldsymbol{p}_* d\boldsymbol{p}_s d\boldsymbol{p}_K d\boldsymbol{p}_\pi \\ & \varrho_*(\boldsymbol{p}_*)\varrho_{K\pi^*}(\boldsymbol{p}_K, \boldsymbol{p}_\pi, \boldsymbol{p}_s \,|\, \boldsymbol{p}_*)\varepsilon_{K\pi}(\boldsymbol{p}_K, \boldsymbol{p}_\pi)\varepsilon_s(\boldsymbol{p}_s) \\ & \big[\mathcal{A}_{\rm CP} + \delta\varepsilon_{K\pi}(\boldsymbol{p}_K, \boldsymbol{p}_\pi) + \delta\varepsilon_s(\boldsymbol{p}_s)\big], \end{aligned}$$

where we have neglected one term of order $\mathcal{A}_{\rm CP}\delta^2$. Similarly,

$$\begin{aligned} N^{\rm obs}_{D^0} - N^{\rm obs}_{\overline{D}^0} = N_{D^*}\ \mathcal{B}(D^* \to D^0\pi)\ \overline{\mathcal{B}}(D^0 \to K\pi) \int & d\boldsymbol{p}_* d\boldsymbol{p}_s d\boldsymbol{p}_K d\boldsymbol{p}_\pi \\ & \varrho_*(\boldsymbol{p}_*)\varrho_{K\pi^*}(\boldsymbol{p}_K, \boldsymbol{p}_\pi, \boldsymbol{p}_s \,|\, \boldsymbol{p}_*)\varepsilon_{K\pi}(\boldsymbol{p}_K, \boldsymbol{p}_\pi)\varepsilon_s(\boldsymbol{p}_s) \\ & \big[1 + \mathcal{A}_{\rm CP}\delta\varepsilon_{K\pi}(\boldsymbol{p}_K, \boldsymbol{p}_\pi) + \mathcal{A}_{\rm CP}\delta\varepsilon_s(\boldsymbol{p}_s) + \delta\varepsilon_{K\pi}(\boldsymbol{p}_K, \boldsymbol{p}_\pi)\delta\varepsilon_s(\boldsymbol{p}_s)\big]. \end{aligned}$$

If we neglect all terms of order $\mathcal{A}_{\rm CP}\delta$ and δ^2, we finally obtain Eq. (3.4):

$$A(K\pi^*) = \left(\frac{N^{\rm obs}_{D^0} - N^{\rm obs}_{\overline{D}^0}}{N^{\rm obs}_{D^0} + N^{\rm obs}_{\overline{D}^0}}\right)^{K\pi^*} = \quad \mathcal{A}_{\rm CP}(K\pi) + \delta(\pi_s)^{K\pi^*} + \delta(K\pi)^{K\pi^*},$$

where we defined

$$\delta(\pi_s)^{K\pi^*} = \int d\boldsymbol{p}_s n_s^{K\pi^*}(\boldsymbol{p}_s)\delta\varepsilon_s(\boldsymbol{p}_s),$$
$$\delta(K\pi)^{K\pi^*} = \int d\boldsymbol{p}_K d\boldsymbol{p}_\pi \; n_{K\pi}^{K\pi^*}(\boldsymbol{p}_K,\boldsymbol{p}_\pi) \; \delta\varepsilon_{K\pi}(\boldsymbol{p}_K,\boldsymbol{p}_\pi),$$

and

$$n_s^{K\pi^*}(\boldsymbol{p}_s) = \frac{\int d\boldsymbol{p}_* d\boldsymbol{p}_\pi d\boldsymbol{p}_K \varrho_*(\boldsymbol{p}_*)\varrho_{K\pi^*}(\boldsymbol{p}_K,\boldsymbol{p}_\pi,\boldsymbol{p}_s \mid \boldsymbol{p}_*)\varepsilon_{K\pi}(\boldsymbol{p}_K,\boldsymbol{p}_\pi)\varepsilon_s(\boldsymbol{p}_s)}{\int d\boldsymbol{p}_* d\boldsymbol{p}_\pi d\boldsymbol{p}_K d\boldsymbol{p}_s \varrho_*(\boldsymbol{p}_*)\varrho_{K\pi^*}(\boldsymbol{p}_K,\boldsymbol{p}_\pi,\boldsymbol{p}_s \mid \boldsymbol{p}_*)\varepsilon_{K\pi}(\boldsymbol{p}_K,\boldsymbol{p}_\pi)\varepsilon_s(\boldsymbol{p}_s)},$$
$$n_{K\pi}^{K\pi^*}(\boldsymbol{p}_K,\boldsymbol{p}_\pi) = \frac{\int d\boldsymbol{p}_* d\boldsymbol{p}_s \varrho_*(\boldsymbol{p}_*)\varrho_{K\pi^*}(\boldsymbol{p}_K,\boldsymbol{p}_\pi,\boldsymbol{p}_s \mid \boldsymbol{p}_*)\varepsilon_{K\pi}(\boldsymbol{p}_K,\boldsymbol{p}_\pi)\varepsilon_s(\boldsymbol{p}_s)}{\int d\boldsymbol{p}_* d\boldsymbol{p}_\pi d\boldsymbol{p}_K d\boldsymbol{p}_s \varrho_*(\boldsymbol{p}_*)\varrho_{K\pi^*}(\boldsymbol{p}_K,\boldsymbol{p}_\pi,\boldsymbol{p}_s \mid \boldsymbol{p}_*)\varepsilon_{K\pi}(\boldsymbol{p}_K,\boldsymbol{p}_\pi)\varepsilon_s(\boldsymbol{p}_s)}.$$

A.2 Untagged $D^0 \to K^-\pi^+$

In this case

$$N_{\overset{(-)}{D}{}^0}^{\rm obs} = \frac{N_D}{2}\; \mathcal{B}(\overset{(-)}{D}{}^0 \to K^\mp\pi^\pm) \int d\boldsymbol{p}_0 d\boldsymbol{p}_\pi d\boldsymbol{p}_K \varrho_{\overset{(-)}{D}{}^0}(\boldsymbol{p}_0)\varrho_{K\pi}(\boldsymbol{p}_K,\boldsymbol{p}_\pi \mid \boldsymbol{p}_0)\varepsilon_{K^\mp\pi^\pm}(\boldsymbol{p}_K,\boldsymbol{p}_\pi)$$

where N_D is the total number of D^0 and $\overline{D}{}^0$ mesons produced (again we assumed $N_{D^0} = N_{\overline{D}{}^0}$ becuase of the CP–symmetric $c\bar{c}$ production in $p\bar{p}$ collisions), $\boldsymbol{p}_0$ is the three–momentum of the $\overset{(-)}{D}{}^0$, $\varrho_{\overset{(-)}{D}{}^0}$ is the density in phase space of $\overset{(-)}{D}{}^0$ mesons; $\varrho_{K\pi}$ is the density in phase space of the $K^\mp\pi^\pm$ pair from D^0 decay.

The difference between charm and anticharm event yields is therefore

$$N_{D^0}^{\rm obs} - N_{\overline{D}{}^0}^{\rm obs} = N_D\; \overline{\mathcal{B}}(D^0 \to K\pi) \int d\boldsymbol{p}_0 d\boldsymbol{p}_\pi d\boldsymbol{p}_K \varrho_0(\boldsymbol{p}_0)\varrho_{K\pi}(\boldsymbol{p}_K,\boldsymbol{p}_\pi \mid \boldsymbol{p}_0)\varepsilon_{K\pi}(\boldsymbol{p}_K,\boldsymbol{p}_\pi)$$
$$\Big\{[1+\delta\varrho_0(\boldsymbol{p}_0)](1+\mathcal{A}_{\rm CP})[1+\delta\varepsilon_{K\pi}(\boldsymbol{p}_K,\boldsymbol{p}_\pi)]$$
$$- [1-\delta\varrho_0(\boldsymbol{p}_0)](1-\mathcal{A}_{\rm CP})[1-\delta\varepsilon_{K\pi}(\boldsymbol{p}_K,\boldsymbol{p}_\pi)]\Big\}$$

where we have defined the following quantities

$$\varrho_0 = \frac{\varrho_{D^0} + \varrho_{\overline{D}{}^0}}{2} \quad \text{and} \quad \delta\varrho_0 = \frac{\varrho_{D^0} - \varrho_{\overline{D}{}^0}}{\varrho_{D^0} + \varrho_{\overline{D}{}^0}}.$$

Assuming η symmetry of the $\boldsymbol{p}_0$ integration region,

$$N_{D^0}^{\rm obs} - N_{\overline{D}{}^0}^{\rm obs} = N_D\; \overline{\mathcal{B}}(D^0 \to K\pi) \int d\boldsymbol{p}_0 d\boldsymbol{p}_\pi d\boldsymbol{p}_K \varrho_0(\boldsymbol{p}_0)\varrho_{K\pi}(\boldsymbol{p}_K,\boldsymbol{p}_\pi \mid \boldsymbol{p}_0)\varepsilon_{K\pi}(\boldsymbol{p}_K,\boldsymbol{p}_\pi)$$
$$[\mathcal{A}_{\rm CP} + \delta\varepsilon_{K\pi}(\boldsymbol{p}_K,\boldsymbol{p}_\pi)].$$

Similarly we obtain

$$N^{\text{obs}}_{D^0} + N^{\text{obs}}_{\overline{D}^0} = N_D\ \overline{\mathcal{B}}(D^0 \to K\pi) \int d\boldsymbol{p}_0 d\boldsymbol{p}_\pi d\boldsymbol{p}_K\, \varrho_0(\boldsymbol{p}_0)\varrho_{K\pi}(\boldsymbol{p}_K, \boldsymbol{p}_\pi\,|\,\boldsymbol{p}_0)\varepsilon_{K\pi}(\boldsymbol{p}_K, \boldsymbol{p}_\pi) \\ \big[1 + \mathcal{A}_{\text{CP}}\ \delta\varepsilon_{K\pi}(\boldsymbol{p}_K, \boldsymbol{p}_\pi)\big].$$

From the last to Equations, neglecting terms proportional to $\mathcal{A}_{\text{CP}}\delta$, we obtain Eq. (3.5):

$$A(K\pi) = \left(\frac{N^{\text{obs}}_{D^0} - N^{\text{obs}}_{\overline{D}^0}}{N^{\text{obs}}_{D^0} + N^{\text{obs}}_{\overline{D}^0}}\right)^{K\pi} = \quad \mathcal{A}_{\text{CP}}(K\pi) + \delta(K\pi)^{K\pi},$$

where we defined

$$\delta(K\pi)^{K\pi} = \int d\boldsymbol{p}_K d\boldsymbol{p}_\pi\ n^{K\pi}_{K\pi}(\boldsymbol{p}_K, \boldsymbol{p}_\pi)\ \delta\varepsilon_{K\pi}(\boldsymbol{p}_K, \boldsymbol{p}_\pi)$$

and

$$n^{K\pi}_{K\pi}(\boldsymbol{p}_K, \boldsymbol{p}_\pi) = \frac{\int d\boldsymbol{p}_0 \varrho_0(\boldsymbol{p}_0)\varrho_{K\pi}(\boldsymbol{p}_K, \boldsymbol{p}_\pi\,|\,\boldsymbol{p}_0)\varepsilon_{K\pi}(\boldsymbol{p}_K, \boldsymbol{p}_\pi)}{\int d\boldsymbol{p}_0 d\boldsymbol{p}_\pi d\boldsymbol{p}_K\, \varrho_0(\boldsymbol{p}_0)\varrho_{K\pi}(\boldsymbol{p}_K, \boldsymbol{p}_\pi\,|\,\boldsymbol{p}_0)\varepsilon_{K\pi}(\boldsymbol{p}_K, \boldsymbol{p}_\pi)}.$$

Appendix B

Monte Carlo Simulation

We provide here a short overview of the standard CDF II simulation which has been used to produce the Monte Carlo samples used in this thesis. Further details can be found in [81].

B.1 Event generator

When you are not interested in the simulation of the entire $p\bar{p}$ collision, the standard tool for generation of heavy–flavoured mesons at CDF is BGenerator [82]. The purpose of BGenerator is to create and fragment heavy quarks (a single q or a $q\bar{q}$ pair), with a given spectrum in rapidity and transverse momentum. The single quark generation follows the theory from P. Nason, S. Dawson and R. K. Ellis [83, 84], while the quark pair generation the ones from M. Mangano, P. Nason and G. Ridolfi [85].

For the samples of simulated charm decays of this thesis, we generated a single charm (bottom) quark per event, forcing it to hadronize into a $D^{*\pm}$ or $\overline{(}\overline{D}\overline{)}^0$ (B^+ or B^0) meson, with an input $p_T - y$ spectrum tuned on measured cross–sections [86, 87].

The created meson are then decayed using the best available descriptions of the decay dynamics provided by the EvtGen package [88]. We produced the inclusive sample of charm decays used to qualitatively understand the sample composition, and the inclusive $B \to DX$ sample, used to study the secondary D mesons present in our data, simulating the full, most updated, table of D and B mesons branching–ratios available from Ref. [7]. In Sect. 3.4 we use, instead, two high–statistics samples of $D^{*+} \to D^{(} \to \pi^+\pi^-)\pi_s^+$ and $D^{*+} \to D^{(} \to K^-\pi^+)\pi_s^+$ decays to test the analysis procedure, in this case only the specified decay chain has been simulated.

Once the physics of the interaction and the generated particles are available,

they are propagated within a simulation of the detector in order to reproduce their interactions with the materials and the different signals they produce in all the subdetectors. For this reason EvtGen does not decay kaons, pions and muons, which are left for Geant in the full detector simulation, which is described in the following section.

B.2 CDF II detector and trigger

In the standard CDF II simulation, the detector geometry and material are modelled using the version 3 of the Geant package [89] tuned to test–beam and collision data. Geant receives in input the positions, the four–momenta and the identities of all particles produced by the simulated collisions that have long enough lifetimes to exit the beam pipe. It simulates their paths in the detector, modelling their interactions (bremsstrahlung, multiple scattering, nuclear interactions, photon conversions, etc.) and the consequent generation of signals on a single channel basis. Specific packages substitute Geant for some sub–detectors: the calorimeter response is simulated with Gflash, a faster parametric shower–simulator [90] tuned for single–particle response and shower–shape using test–beam data (8–230 GeV electrons and charged pions) and collision data (0.5–40 GeV/c single isolated tracks); the drift–time within the COT is simulated using the Garfield standard package [91, 92] further tuned on data; the charge–deposition model in the silicon uses a parametric model, tuned on data, which accounts for restricted Landau distributions, production of δ rays, capacitive charge–sharing between neighboring strips and noise [93].[1] Furthermore, the actual trigger logic is simulated. The output of the simulated data mimics the structure of collision data, allowing their analysis with the same reconstruction programs used for collision data.

The detector and trigger configuration undergo variations during data–taking. Minor variations may occur between runs, while larger variations occur, for instance, after major hardware improvements, or TeVatron shut–down periods. For a more detailed simulation of the actual experimental conditions, the simulation has been interfaced with the online database that reports, on a run–by–run basis, all known changes in configuration (position and slope of the beam line, relative

[1] The δ rays are knock–on electrons emitted from atoms when the passage of charged particles through matter results in transmitted energies of more than a few keV in a single collision.

mis–alignments between sub–detectors, trigger table used, set of SVT parameters) and local or temporary inefficiencies in the silicon tracker (active coverage, noisy channels, etc.). This allows us to simulate the detailed configuration of any set of real runs and to use it, after proper luminosity reweighing, for modeling the realistic detector response in any given subset of data.

Bibliography

[1] T. Aaltonen *et al.* (CDF Collaboration), *Measurement of CP–violating asymmetries in* $D^0 \to \pi^+\pi^-$ *and* $D^0 \to K^+K^-$ *decays at CDF*, Phys. Rev. D **85**, 012009 (2012) [arXiv:1111.5023 (hep-ex)].

[2] T. Lee and C.-N. Yang, *Question of Parity Conservation in Weak Interactions*, Phys. Rev. **104**, 254 (1956).

[3] C. Wu *et al.*, *Experimental Test of Parity Conservation in Beta Decay*, Phys. Rev. **105**, 1413 (1957).

[4] R. Garwin, L. Lederman, and M. Weinrich, *Observations of the Failure of Conservation of Parity and Charge Conjugation in Meson Decays: The Magnetic Moment of the Free Muon*, Phys. Rev. **105**, 1415 (1957).

[5] G. Luders, *On the Equivalence of Invariance under Time Reversal and under Particle-Antiparticle Conjugation for Relativistic Field Theories*, Kong. Dan. Vid. Sel. Mat. Fys. Med. **28N5**, 1 (1954).

[6] G. Luders, *Proof of the TCP theorem*, Annals Phys. **2**, 1 (1957).

[7] K. Nakamura *et al.* (Particle Data Group), *Review of particle physics*, J. Phys. **G37**, 075021 (2010), and 2011 partial update for the 2012 edition at `http://pdg.lbl.gov`.

[8] J. Christenson, J. Cronin, V. Fitch, and R. Turlay, *Evidence for the* 2π *Decay of the* K_2^0 *Meson*, Phys. Rev. Lett. **13**, 138 (1964).

[9] S. Glashow, *Partial Symmetries of Weak Interactions*, Nucl. Phys. **22**, 579 (1961).

[10] S. Weinberg, *A Model of Leptons*, Phys. Rev. Lett. **19**, 1264 (1967).

[11] A. Salam, in *Elementary particle theory*, edited by N. Svartholm (Almquist & Wiksell, 1968), pp. 367–377.

[12] S. Glashow, J. Iliopoulos, and L. Maiani, *Weak Interactions with Lepton-Hadron Symmetry*, Phys. Rev. **D2**, 1285 (1970).

[13] M. Kobayashi and T. Maskawa, *CP Violation in the Renormalizable Theory of Weak Interaction*, Prog. Theor. Phys. **49**, 652 (1973).

[14] J. Augustin *et al.* (SLAC-SP-017 Collaboration), *Discovery of a Narrow Resonance in e+ e- Annihilation*, Phys. Rev. Lett. **33**, 1406 (1974).

[15] J. Aubert *et al.* (E598 Collaboration), *Experimental Observation of a Heavy Particle J*, Phys. Rev. Lett. **33**, 1404 (1974).

[16] S. Herb *et al.*, *Observation of a Dimuon Resonance at 9.5-GeV in 400-GeV Proton-Nucleus Collisions*, Phys. Rev. Lett. **39**, 252 (1977).

[17] F. Abe *et al.* (CDF Collaboration), *Observation of top quark production in $\bar{p}p$ collisions*, Phys. Rev. Lett. **74**, 2626 (1995) [arXiv:hep-ex/9503002].

[18] S. Abachi *et al.* (DØ Collaboration), *Search for high mass top quark production in $p\bar{p}$ collisions at $\sqrt{s} = 1.8$ TeV*, Phys. Rev. Lett. **74**, 2422 (1995) [arXiv:hep-ex/9411001].

[19] V. Fanti *et al.* (NA48 Collaboration), *A New measurement of direct CP violation in two pion decays of the neutral kaon*, Phys. Lett. **B465**, 335 (1999) [arXiv:hep-ex/9909022].

[20] A. Alavi-Harati *et al.* (KTeV Collaboration), *Observation of direct CP violation in $K_{S,L} \to \pi\pi$ decays*, Phys. Rev. Lett. **83**, 22 (1999) [arXiv:hep-ex/9905060].

[21] B. Aubert *et al.* (*BABAR* Collaboration), *Observation of CP violation in the B^0 meson system*, Phys. Rev. Lett. **87**, 091801 (2001) [arXiv:hep-ex/0107013].

[22] K. Abe *et al.* (Belle Collaboration), *Observation of large CP violation in the neutral B meson system*, Phys. Rev. Lett. **87**, 091802 (2001) [arXiv:hep-ex/0107061].

[23] B. Aubert *et al.* (*BABAR* Collaboration), *Observation of direct CP violation in $B^0 \to K^+\pi^-$ decays*, Phys. Rev. Lett. **93**, 131801 (2004) [arXiv:hep-ex/0407057].

[24] B. Aubert *et al.* (*BABAR* Collaboration), *Observation of CP violation in $B^0 \to K^+\pi^-$ and $B^0 \to \pi^+\pi^-$*, Phys. Rev. Lett. **99**, 021603 (2007) [arXiv:hep-ex/0703016].

[25] A. Sakharov, *Violation of CP Invariance, C Asymmetry, and Baryon Asymmetry of the Universe*, Pisma Zh. Eksp. Teor. Fiz. **5**, 32 (1967), Reprinted in "E. W. Kolb and M. S. Turner (ed.), *The early universe*, 371-373", and in "D. Lindley et al. (ed.), *Cosmology and particle physics*, 106-109", and in "Sov. Phys. Usp. **34** (1991) 392-393 [Usp. Fiz. Nauk. **161** (1991) No. 5 61-64]".

[26] G. R. Farrar and M. Shaposhnikov, *Baryon asymmetry of the universe in the standard electroweak theory*, Phys. Rev. **D50**, 774 (1994) [arXiv:hep-ph/9305275].

[27] P. Huet and E. Sather, *Electroweak baryogenesis and standard model CP violation*, Phys. Rev. **D51**, 379 (1995) [arXiv:hep-ph/9404302].

[28] M. Gavela, M. Lozano, J. Orloff, and O. Pene, *Standard model CP violation and baryon asymmetry. Part 1: Zero temperature*, Nucl. Phys. **B430**, 345 (1994) [arXiv:hep-ph/9406288].

[29] M. E. Peskin and D. V. Schroeder, *An Introduction to quantum field theory* (Addison–Wesley, 1995).

[30] I. I. Bigi, *CP violation: An Essential mystery in nature's grand design*, Surveys High Energ. Phys. **12**, 269 (1998) [arXiv:hep-ph/9712475].

[31] R. Peccei and H. R. Quinn, *Constraints Imposed by CP Conservation in the Presence of Instantons*, Phys. Rev. **D16**, 1791 (1977).

[32] R. Peccei and H. R. Quinn, *CP Conservation in the Presence of Instantons*, Phys. Rev. Lett. **38**, 1440 (1977).

[33] E. K. Akhmedov, *Neutrino physics*, 103 (1999) [arXiv:hep-ph/0001264].

[34] N. Cabibbo, *Unitary Symmetry and Leptonic Decays*, Phys. Rev. Lett. **10**, 531 (1963).

[35] J. Charles *et al.* (CKMfitter Group), *CP violation and the CKM matrix: Assessing the impact of the asymmetric B factories*, Eur. Phys. J. **C41**, 1 (2005) [arXiv:hep-ph/0406184], updated results and plots available at http://ckmfitter.in2p3.fr.

[36] L. Wolfenstein, *Parametrization of the Kobayashi-Maskawa Matrix*, Phys. Rev. Lett. **51**, 1945 (1983).

[37] A. J. Buras, M. E. Lautenbacher, and G. Ostermaier, *Waiting for the top quark mass, $K^+ \to \pi^+\nu\overline{\nu}$, $B^0_{(s)} - \overline{B}^0_{(s)}$ mixing and CP asymmetries in B decays*, Phys. Rev. **D50**, 3433 (1994) [arXiv:hep-ph/9403384].

[38] Y. Ahn, H.-Y. Cheng, and S. Oh, *Wolfenstein Parametrization at Higher Order: Seeming Discrepancies and Their Resolution*, Phys. Lett. **B703**, 571 (2011) [arXiv:1106.0935 (hep-ph)].

[39] C. Jarlskog, *Commutator of the Quark Mass Matrices in the Standard Electroweak Model and a Measure of Maximal CP Violation*, Phys. Rev. Lett. **55**, 1039 (1985).

[40] Y. Nir, *CP violation*, Conf. Proc. **C9207131**, 81 (1992).

[41] D. Asner *et al.* (Heavy Flavor Averaging Group), *Averages of b-hadron, c-hadron, and τ-lepton Properties*, (2010) [arXiv:1010.1589 (hep-ex)], and updates at http://www.slac.stanford.edu/xorg/hfag.

[42] B. Aubert *et al.* (*BABAR* Collaboration), *Evidence for $D^0 - \overline{D}^0$ Mixing*, Phys. Rev. Lett. **98**, 211802 (2007) [arXiv:hep-ex/0703020].

[43] M. Staric *et al.* (Belle Collaboration), *Evidence for $D^0 - \overline{D}^0$ Mixing*, Phys. Rev. Lett. **98**, 211803 (2007) [arXiv:hep-ex/0703036].

[44] T. Aaltonen *et al.* (CDF Collaboration), *Evidence for $D^0 - \overline{D}^0$ mixing using the CDF II Detector*, Phys. Rev. Lett. **100**, 121802 (2008) [arXiv:0712.1567 (hep-ex)].

[45] A. A. Petrov, *Charm mixing in the Standard Model and beyond*, Int. J. Mod. Phys. **A21**, 5686 (2006) [arXiv:hep-ph/0611361].

[46] E. Golowich, J. Hewett, S. Pakvasa, and A. A. Petrov, *Implications of $D^0 - \bar{D}^0$ Mixing for New Physics*, Phys. Rev. **D76**, 095009 (2007) [arXiv:0705.3650 (hep-ph)].

[47] Y. Nir and N. Seiberg, *Should squarks be degenerate?*, Phys. Lett. **B309**, 337 (1993) [arXiv:hep-ph/9304307].

[48] M. Ciuchini *et al.*, *D - $\bar{D}$ mixing and new physics: General considerations and constraints on the MSSM*, Phys. Lett. **B655**, 162 (2007) [arXiv:hep-ph/0703204].

[49] S. Bianco, F. Fabbri, D. Benson, and I. Bigi, *A Cicerone for the physics of charm*, Riv. Nuovo Cim. **26N7**, 1 (2003) [arXiv:hep-ex/0309021].

[50] Y. Grossman, A. L. Kagan, and Y. Nir, *New physics and CP violation in singly Cabibbo suppressed D decays*, Phys. Rev. **D75**, 036008 (2007) [arXiv:hep-ph/0609178].

[51] I. I. Bigi and A. Sanda, *On $D^0 - \overline{D}^0$ Mixing and CP Violation*, Phys. Lett. **B171**, 320 (1986).

[52] G. Blaylock, A. Seiden, and Y. Nir, *The Role of CP violation in $D^0 - \overline{D}^0$ mixing*, Phys. Lett. **B355**, 555 (1995) [arXiv:hep-ph/9504306].

[53] S. Bergmann *et al.*, *Lessons from CLEO and FOCUS measurements of $D^0 - \overline{D}^0$ mixing parameters*, Phys. Lett. **B486**, 418 (2000) [arXiv:hep-ph/0005181].

[54] B. Aubert *et al.* (*BABAR* Collaboration), *Search for CP violation in the decays $D^0 \to K^-K^+$ and $D^0 \to \pi^-\pi^+$*, Phys. Rev. Lett. **100**, 061803 (2008) [arXiv:0709.2715 (hep-ex)].

[55] M. Staric *et al.* (Belle Collaboration), *Measurement of CP asymmetry in Cabibbo suppressed D^0 decays*, Phys. Lett. **B670**, 190 (2008) [arXiv:0807.0148 (hep-ex)].

[56] D. Acosta *et al.* (CDF Collaboration), *Measurement of partial widths and search for direct CP violation in D^0 meson decays to K^-K^+ and $\pi^-\pi^+$*, Phys. Rev. Lett. **94**, 122001 (2005) [arXiv:hep-ex/0504006].

[57] S. D. Holmes (ed.), *Tevatron Run II Handbook*, FERMILAB-TM-2484 (1998).

[58] S. Holmes, R. S. Moore, and V. Shiltsev, *Overview of the Tevatron Collider Complex: Goals, Operations and Performance*, (2011) [arXiv:1106.0909 (physics.acc-ph)].

[59] R. Blair *et al.* (CDF Collaboration), *The CDF II detector: Technical design report*, FERMILAB-DESIGN-1996-01 (1996).

[60] C. S. Hill (On behalf of the CDF Collaboration), *Operational experience and performance of the CDF II silicon detector*, Nucl. Instrum. Meth. **A530**, 1 (2004).

[61] A. Sill (CDF Collaboration), *CDF Run II silicon tracking projects*, Nucl. Instrum. Meth. **A447**, 1 (2000).

[62] A. A. Affolder *et al.* (CDF Collaboration), *Intermediate silicon layers detector for the CDF experiment*, Nucl. Instrum. Meth. **A453**, 84 (2000).

[63] A. A. Affolder *et al.* (CDF Collaboration), *CDF central outer tracker*, Nucl. Instrum. Meth. **A526**, 249 (2004).

[64] P. Gatti, *Performance of the new tracking system at CDF II*, Ph.D. thesis, University of Pisa, 2001, available as FERMILAB-THESIS-2001-23.

[65] S. Menzemer, *Track reconstruction in the silicon vertex detector of the CDF II experiment*, Ph.D. thesis, Karlsruhe University, 2003, available as FERMILAB-THESIS-2003-52, IEKP-KA-2003-04.

[66] C. P. Hays *et al.*, *Inside-out tracking at CDF*, Nucl. Instrum. Meth. **A538**, 249 (2005).

[67] L. Balka *et al.* (CDF Collaboration), *The CDF Central Electromagnetic Calorimeter*, Nucl. Instrum. Meth. **A267**, 272 (1988).

[68] E. J. Thomson *et al.*, *Online track processor for the CDF upgrade*, IEEE Trans. Nucl. Sci. **49**, 1063 (2002).

[69] A. Abulencia *et al.* (CDF Collaboration), *The CDF II eXtremely fast tracker upgrade*, Nucl. Instrum. Meth. **A572**, 358 (2007).

[70] B. Ashmanskas *et al.* (CDF-II Collaboration), *The CDF silicon vertex trigger*, Nucl. Instrum. Meth. **A518**, 532 (2004) [arXiv:physics/0306169 (physics)].

[71] L. Ristori and G. Punzi, *Triggering on Heavy Flavors at Hadron Colliders*, Ann. Rev. Nucl. Part. Sci. **60**, 595 (2010).

[72] D. Acosta *et al.*, *The performance of the CDF luminosity monitor*, Nucl. Instrum. Meth. **A494**, 57 (2002).

[73] T. Aaltonen *et al.* (CDF Collaboration), *Measurements of Direct CP Violating Asymmetries in Charmless Decays of Strange Bottom Mesons and Bottom Baryons*, Phys. Rev. Lett. **106**, 181802 (2011) [arXiv:1103.5762 (hep-ex)].

[74] P. S. Maybeck, *Stochastic models, estimation, and control* (Academic Press, New York, 1979), Vol. 141, and references therein.

[75] D. Acosta *et al.* (CDF Collaboration), *Measurement of b hadron masses in exclusive J/ψ decays with the CDF detector*, Phys. Rev. Lett. **96**, 202001 (2006) [arXiv:hep-ex/0508022].

[76] N. L. Johnson, *Systems of frequency curves generated by methods of translation*, Biometrika **36**, 149 (1949).

[77] S. Bar-Shalom, G. Eilam, M. Gronau, and J. L. Rosner, *Second order direct CP asymmetry in $B_{(s)} \to X\ell\nu$*, Phys.Lett. **B694**, 374 (2011) [arXiv:1008.4354 (hep-ph)].

[78] R. Aaij *et al.* (LHCb Collaboration), *Evidence for CP violation in time-integrated $D^0 \to h^-h^+$ decay rates*, Phys. Rev. Lett. **108**, 111602 (2012) [arXiv:1112.0938 (hep-ex)].

[79] I. I. Bigi, A. Paul, and S. Recksiegel, *Conclusions from CDF Results on CP Violation in $D^0 \to \pi^+\pi^-$, K^+K^- and Future Tasks*, JHEP **1106**, 089 (2011) [arXiv:1103.5785 (hep-ph)].

[80] I. I. Bigi and A. Paul, *On CP Asymmetries in Two-, Three- and Four-Body D Decays*, (2011) [arXiv:1110.2862 (hep-ph)].

[81] *CDF Detector Simulation*, http://www-cdf.fnal.gov/cdfsim/.

[82] P. Sphicas *et al.*, *A $b\bar{b}$ Monte Carlo Generator*, CDF Notes 2655 and 5092 (1994 and 1999).

[83] P. Nason, S. Dawson, and R. Ellis, *The Total Cross-Section for the Production of Heavy Quarks in Hadronic Collisions*, Nucl. Phys. **B303**, 607 (1988).

[84] P. Nason, S. Dawson, and R. Ellis, *The One Particle Inclusive Differential Cross-Section for Heavy Quark Production in Hadronic Collisions*, Nucl. Phys. **B327**, 49 (1989).

[85] M. L. Mangano, P. Nason, and G. Ridolfi, *Heavy quark correlations in hadron collisions at next-to-leading order*, Nucl. Phys. **B373**, 295 (1992).

[86] D. Acosta *et al.* (CDF Collaboration), *Measurement of prompt charm meson production cross sections in $p\bar{p}$ collisions at $\sqrt{s} = 1.96$ TeV*, Phys. Rev. Lett. **91**, 241804 (2003) [arXiv:hep-ex/0307080].

[87] D. Acosta *et al.* (CDF Collaboration), *Measurement of the J/ψ meson and $b-$hadron production cross sections in $p\bar{p}$ collisions at $\sqrt{s} = 1960$ GeV*, Phys. Rev. **D71**, 032001 (2005) [arXiv:hep-ex/0412071].

[88] W. Bell *et al.*, *User Guide For* EvtGen *at CDF*, CDF Notes 7917 and 5618 (2005 and 2003).

[89] R. Brun *et al.*, Geant*: Simulation Program For Particle Physics Experiments. User Guide and Reference Manual*, CERN-DD-78-2-REV (1978).

[90] P. A. Movilla Fernandez (CDF Collaboration), *Performance of the CDF calorimeter simulation in Tevatron Run II*, AIP Conf. Proc. **867**, 487 (2006) [arXiv:physics/0608081].

[91] R. Veenhof, Garfield*, a drift chamber simulation program*, , prepared for International Conference on Programming and Mathematical Methods for Solving Physical Problems, Dubna, Russia, 14-19 Jun 1993.

[92] R. Veenhof, Garfield*, recent developments*, Nucl. Instrum. Meth. **A419**, 726 (1998).

[93] M. Gold, *Description of the Parameterized Charge Deposition Model*, CDF Note 5871 (2002).